Multi-Axis Instrumentation for Robotized Micro-assembly

Bhawnath Tiwari

To cite this version:

Bhawnath Tiwari. Multi-Axis Instrumentation for Robotized Micro-assembly. Automatic. Université Bourgogne Franche-Comté, 2021. English. NNT : 2021UBFCD007 . tel-03327751

HAL Id: tel-03327751
https://theses.hal.science/tel-03327751v1

Submitted on 27 Aug 2021

THÈSE DE DOCTORAT DE L'ÉTABLISSEMENT
UNIVERSITÉ BOURGOGNE FRANCHE-COMTÉ
PREPARÉE À L'UNIVERSITÉ DE FRANCHE COMTÉ

ÉCOLE DOCTORALE N° 37
SCIENCES PHYSIQUES POUR L'INGÉNIEUR ET
MICROTECHNIQUES

Doctorat d'Automatique

PAR
Bhawnath TIWARI

Instrumentation multi-axes pour micro-assemblage robotisé

Soutenue publiquement le 14 Janvier 2021, à Besançon
devant le jury composé de :

Franck CHOLLET	Professeur, Univ. Bourgogne Franche-Comté, France	Président
Micky RAKOTONDRABE	Professeur, ENIT, Tarbes	Rapporteur
Frédéric LAMARQUE	Professeur, UTC, Compiègne	Rapporteur
Irène FASSI	Maître de Recherche, CNR, Italie	Examinateur
David J. CAPPELLERI	Maître de Conférences, Université Purdue, États Unis	Examinateur
Philippe LUTZ	Professeur, UBFC, Besançon	Co-encadrant de thèse
Cédric CLÉVY	Maître de Conférences, HDR, UBFC, Besançon	Directeur de thèse

Doctoral Thesis of the University of Bourgogne Franche-Comté prepared at University of Franche-Comté

Doctoral School n° 37
Engineering Sciences and Microtechnologies

Doctorate in Automation

By
Bhawnath Tiwari

Multi-axis Instrumentation for Robotized Micro-assembly

Thesis defended publicly on 14 January 2021, at Besançon
composition of jury :

Micky RAKOTONDRABE	Professor, ENIT, Tarbes	Reviewer
Frédéric LAMARQUE	Professor, UTC, Compiègne	Reviewer
Irène FASSI	Senior Researcher, CNR, Italy	Examiner
David J. CAPPELLERI	Associate Prof., Purdue University, USA	Examiner
Franck CHOLLET	Professor, UBFC, Besançon	Examiner
Philippe LUTZ	Professor, UBFC, Besançon	Thesis Co-supervisor
Cédric CLÉVY	Associate Prof., HDR, UBFC, Besançon	Thesis Director

Acknowledgements

Enjoyment of any journey gets amplified when we have interesting people on board. In the same way, thesis work also requires involvement of adequate people. I would like to thank every individual who directly or indirectly participated in this exciting journey of my doctoral thesis. It is always said that crests and troughs, are part of any journey, but a proper guidance and support always expected for not only its completion but for a healthy learning. Therefore, in this context I express my deepest thanks to my thesis director, Associate Prof. Cédric Clévy and co-supervisor Prof. Philippe Lutz, whose proper guidance and supports, significantly helped me to reach a meaningful completion of this thesis.

I would like to thank my thesis jury members, Pr. Franck Chollet, Pr. Frédéric Lamarque, Pr. Micky Rakotondrabe, Dr. Irène Fassi, and Pr.(Assoc.) David J. Cappelleri, for their time and constructive participation in my soutenance. Your remarks and suggestions are really encouraging and helpful for my research works, it was indeed an amazing learning experience.

As my thesis was in collaboration [COLAMIR 20] with academic-industrial partners, I take this opportunity to say thanks to every members of this project. I would like to especially mention names of Dr. Joël Agnus, Mr. Patrick Rougeot from Femto-ST Institute and Stephane, Margot Billot, and Charlotte Quesnel from Percipio Robotics, who helped me on technical sides throughout my thesis.

I also would like to express my sincere gratitude to every members of AS2M Department, must say that I was fortunate enough to be part of this happy and supportive research family. I especially would like to mention here some of my collegues, Jöel Bafumba Liseli, Marwa Haddad, Ning Liu, Jesus Toledo, Benjamin Mauze, Amine Benouhiba, Yuning Lei, and Luc Petiet. I can proudly say, that I learned a lot from you guys.

I am immensely thankful to my family members for their continuous love, blessings, and supports. Finally, I express my deepest respect and honor for the ultimate purest energy, my god, whose blessings helped me to complete this amazing journey.

Bhawnath Tiwari

Contents

List of Figures

List of Tables

Introduction

Instrumentation of the structures allows their use as sensing devices. Micro-world also requires such instrumentation, mainly for tasks automation or local accurate characterization (interesting for human robot collaborative tasks). The micro-structures because of their fragility and high sensitivity to the uneven environmental variation requires special care in the development of sensing and/or actuation mechanism. In the context of micro-robotics the force/torque sensing can bolster the decision making capability during the tasks. There are varieties of tasks where single axis force sensing is not adequate enough to meet the objective, for example manipulation of the object against an unknown environment, or the rotation of the object, or the assembly of micro-components using a thick film of glue. Many things are indeed coupled thus key things happen on several axis and measuring a single one induces key limitation in the analysis. A diverse and flexible decision making capability during different task handling requires knowledge of the local states along the multi-axis, which can be fulfilled by an instrumented multi-axis force/torque sensor.

The thesis titled “Multi-Axis Instrumentation for Robotized Micro-assembly” covers the different key points in the context of micro-robotics. This thesis is part of the ANR (National Research Agency) project “Collaborative Agile Miniaturized Robotics for ultra-precise assembly (COLAMIR) [COLAMIR 20]” and is focused for the different requirements in the industrial scenario. To start with, a general study of different robotized works in micro-world, the requirement of instrumentation (specially in the context the COLAMIR project), and conclusion from different works (from the state of the art) is presented in Chapter I. Assembly of micro-components is an important and frequent use in the industries. Gluing allows a fixed relative positioning of the two structures, but it brings additional challenges when it comes to positioning accuracy. This issue is addressed in the Chapter II of this thesis where analysis of gluing and its use for precise positioning is demonstrated. The corresponding studies were made along one axis, where the impact was maximum from the gluing. The studies made therefore suggested the requirement of multi-axis instrumentation. This thesis work then covers the instrumentation requirement for the force-sensing along multi-axis. The instrumentation of the structure may be done by instrumenting the platform used for the task, and/or instrumenting the tool used for the manipulation of the micro-component. Both these possibilities are addressed in this thesis. Firstly, an instrumented sensing platform is proposed with a sensing capability of forces along the two planar axes, and the torque about the plane. This work is detailed and is discussed in Chapter III. Following, the instrumentation requirements in the manipulation, a piezoresistive force sensing tool was developed. This tool can sense the force along the two axes, while it can be used for different applications where

2 axis sensing are required but is designed to be used for gripping and assembly tasks. The development of this sensing tool from design, analysis, fabrication and experimental validation of the performance is discussed in chapter IV. Chapter V constitutes, the use of demonstrated instrumented systems for the micro-scale tasks. In this direction, the sensing tool demonstrated in chapter IV was used to develop a microgripper by integration of the tool with piezoelectric actuator. The developed system was then demonstrated with experimental validation following the actuation modeling and tasks covering the micro-grasping and release. Also, an extension of gluing study along multi-axis is presented with a combined use of sensing platform (chapter III), and the microgripper developed.

Chapter I

Instrumentation and Robotics at the Micro-scale

I.1 INTRODUCTION

The excitement and motivation to explore more in the miniaturized world made the researchers to investigate different sensing and actuation mechanisms. From the development of microscope to a very high resolution camera is one of the different advancements made towards the study of micro-world. In the recent years, microscopy development includes the work on range to resolution improvement [Perkel 19], use of artificial intelligence for real time medical diagnosis [Chen 19] to development of portable microscopes that can be used in freely behaving animals [Senarathna 19]. Visualization of structures at micro/nano scale strengthen the motivation to interact with them at such scales. But, unlike the macro-world, interaction with micro/nano structures require extra attention because of their fragility and surface forces predominance at these scales. This lead to the requirement of an intermediate system between the micro-structures and the end-user. Robotic systems can bring interesting results if they are used as intermediate systems to interact with fragile micro-structures. This can be seen in these recent years, where micro-robotic systems demonstrated their usefulness in varieties of applications (detailed in section I.2). But, the performances of any micro-robotic system may be limited by the complexity of the tasks. At the micro-scale, such limitations mainly occur from the lack of local state(s) knowledge and/or their according use in analysis or decision making. Modeling could be one way to provide information of such local state(s), but it's not very obvious to model interaction forces which may differ depending on their nature (e.g. van-der-Waal's, surface tension etc.). Instrumentation, therefore appears as a key requirement. Choice of the instrumented system may vary depending on the targeted works. This thesis work is a part of an academic-industrial project [COLAMIR 20]. The corresponding instrumented micro-robotic system development was considered in the industrial context with focus on manipulation and assembly at the micro-scale (detailed in Section I.3). Depending on the complexity of the task, multi-axis state information can enrich the system capability for decision making during the task or the post-experiment analysis. Therefore the multi-axis instrumentation development meeting the desired specifications of the task appears as a key lock. A discussion on the instrumented system development is presented in section I.4. Finally, the conclusion of this chapter is made in the section I.5.

I.2 MICROROBOTICS AND ITS APPLICATIONS

Robotic advancements lead to extend its application also for the miniaturized world. The medical domain witnessed several potential usefulness of the microrobotics. This field needs dedicated, precise and repeatable task handling capabilities. Whether it deals with the navigation of a tool inside intestine [Wu 19], or the use of biohybrid microrobots [Alapan 19] for in vivo imaging and cargo delivery; microrobotics is of an immense importance. The ultra sensitive tasks like perform-

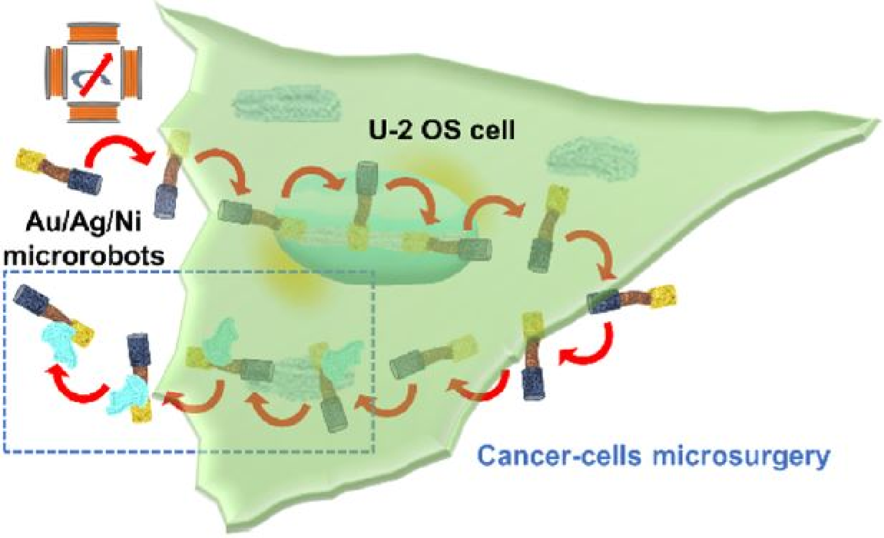

Figure I.1 – Microrobot for cancer cells microsurgery [Vyskocil 20]

ing surgical operations [Vyskocil 20] (Fig. I.1) and transport of cells [Yasa 19] in a confined environment, has also been effectively carried out using microrobots. Whereas the use of microrobotics is also found relevant in the fast detection of toxin, especially in the infection such as clostridium difficile [Yang 20]. Microrobotics demonstrated a potential interest in performing a precise and organized way for varieties of medical tasks. There are still several advancement needed in different context of medical applications, which includes the multimodal sensing and tool development to achieve complex and dexterous tasks inside the body.

The interaction capability of the microrobotic systems with varieties of microstructures can be benefited to have the characterization of the interacting structures. These structures could be biological cell/tissue, DNA or any active or passive micro-structures. The key targeted features in the characterization of any structure in general could be optical, chemical, electrical and mechanical. Because these key properties are the basis to provide important information about the targeted structure and therefore are considered in different applications. Optical characterization which is non-contact based interaction, such as of porcine tissues [Mosca 20], or the collagen synthesis for the creation of scaffolds [Galeano 20], brings useful information of the target. Raman spectroscopy techniques used in vivo targeted brain cancer tissue biopsy [Desroches 18] validates the optical signature influence in the medical context. Mechanical characterization such as [Park 18], [Budday 17] brings interest of mechanical parameters influence on the study of structural health. Whereas the electrical properties are also useful to know the structural wellness, like the case of study of healthy and malign tissues study [Teixeira 18], [Fornes-Leal 16]. The electrical characterization of carbon nano tubes in terms of its electrical resistance and resistivity [Clévy 19] shown in Fig. I.2 can also be realized with the help of suitable positioning (nanopositioner) and measuring system (pico-ammeter). Industrial applications, where

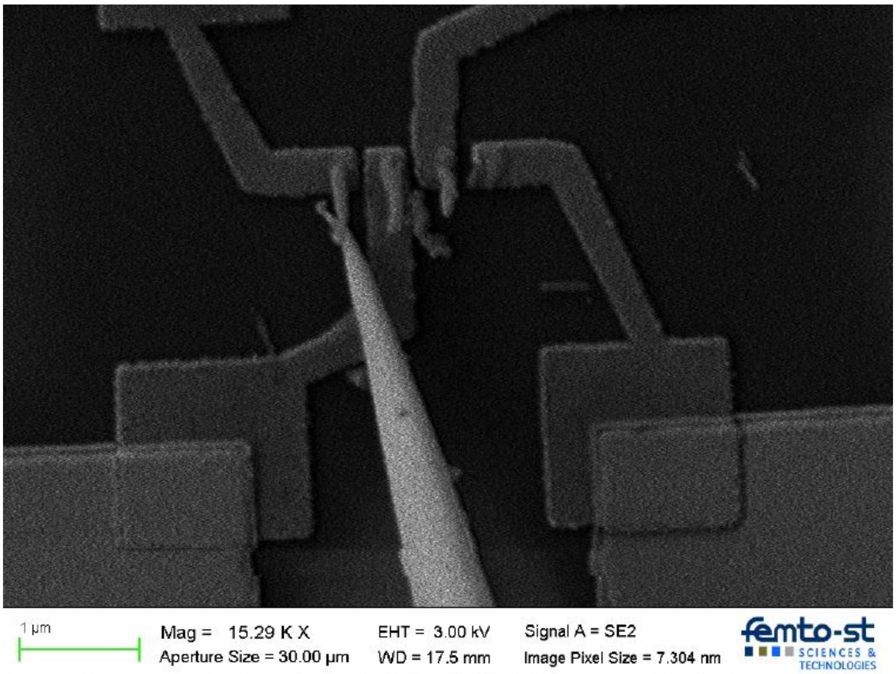

Figure I.2 – Electrical characterization of a carbon nano-tube in contact with a probe [Clévy 19]

manipulation of micro-structures and their assembly is needed, microrobotics is significantly useful in such applications. The different works, constituent complexity and according analysis in the industrial scenario (targeted work of this thesis) are discussed in section I.3. Microrobotics therefore has demonstrated its usefulness in wide range of applications and so, the trend towards miniaturization of the systems is of great importance.

I.3 THESIS CONTEXT AND TARGETED WORKS

Microrobotic systems development and/or the different tools to interact with the micro-world require their fabrication. Although different advanced processes make it possible to fabricate the micro-structure needed, but still some complexity in structure may limit a direct fabrication (depending on time, accuracy or cost limitations). To fabricate such structures, fabrication into sub-components followed by their assembly is a key interesting solution, provided the process employed able to meet the accuracy and assembly challenges.

This thesis is a part of the ANR COLAMIR [COLAMIR 20], which is an academic-industrial collaboration project. The collaborated industrial partners were "Percipio Robotics" and "Aurea Technology". As part of this project, this thesis targeted precise micro-assembly and according system(s) development to address the industrial requirements. The assembly of two structures are very common need in industries, where relative positioning of the two components can be significantly important. To address the fast and large productivity in industrial scenario, the robotization of the assembly process is targeted. This minimizes the requirement of human assembler (can introduce the uncertainty in the positioning of the end product) and also can insure repeatable and cost effective manufacturing. The primary requirement is to understand the complexity and challenges at micro-scale (subsection I.3.1), secondly to analyse the different existing micro-assembly and manipulation works (subsection I.3.2). It also becomes important to study the potential and large demanding micro-assembly techniques. In this direction, use of glue for assembly is an important requirement. Gluing can allow to definitely hold the two surfaces and is a very common need in the industries. The use of glue for micro-assembly, and its corresponding challenges are discussed in subsection I.3.3.

I.3.1 Challenges at the micro-scale

The micro-structure because of their fragility brings additional challenges, as it can be easily broken if not handled carefully. At the micro-scale, surface forces also play an important role, as the van der Waals forces may get dominated than the required interaction force normally needed. For masses less than 10^{-6} kg, adhesive forces becomes more significant than the gravity. A comparison of adhesive forces at micro-level is discussed in [Neugebauer 11] from different state-of-the-art and is shown in Fig. I.3. It can be seen that the adhesive forces such as surface tension, electrostatic, van der Waal's become dominant with the reduction in the object size. Among different adhesive forces, surface tension is significantly high with respect to other forces, which therefore needs to be considered wherever there is an interaction between a micro-object with liquid.

The other challenge at micro-scale task handling is from the micro-system's dynamic. Depending on the compliance of the micro-structure, the dynamic influence may bring additional inertial influence, which sometimes may lead to breakage of the micro-systems. Such happening may get more pronounced when there is fast processing needed. The disturbances from the environment, which could be in the form such as electromechanical or optical, may also impact the targeted behavior, for instance the actuation or actuation based on the sensed state(s). Therefore the according system design and/or the approach to interact with the micro-structures needs to be compatible with the mentioned challenges.

I.3.2 Micro-assembly and the requirements

In the context of assembly, the micro-building components may be assembled manually, but it requires an adequate level of expertise depending on the targeted accuracy of the assembled product. Not only the targeted accuracy is one requirement but the safety of the fragile structure during the assembly should also be a core consideration. In order to minimize a direct interaction of human being with micro-structure (which often results uncertainty in the interaction forces, and

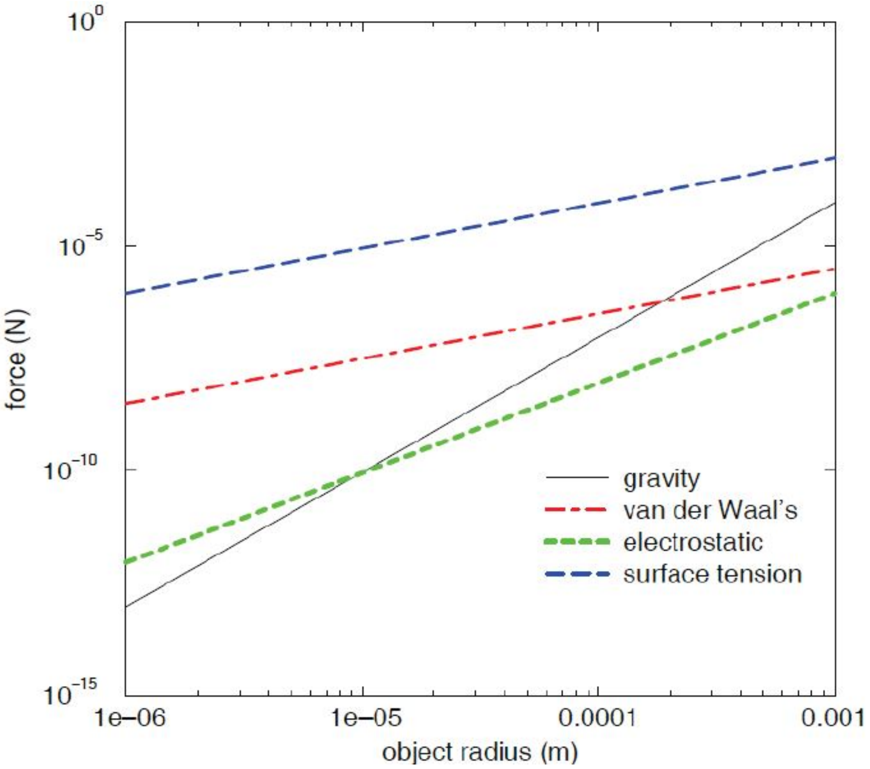

Figure I.3 – Comparison of forces at the micro-scale discussed in [Neugebauer 11]

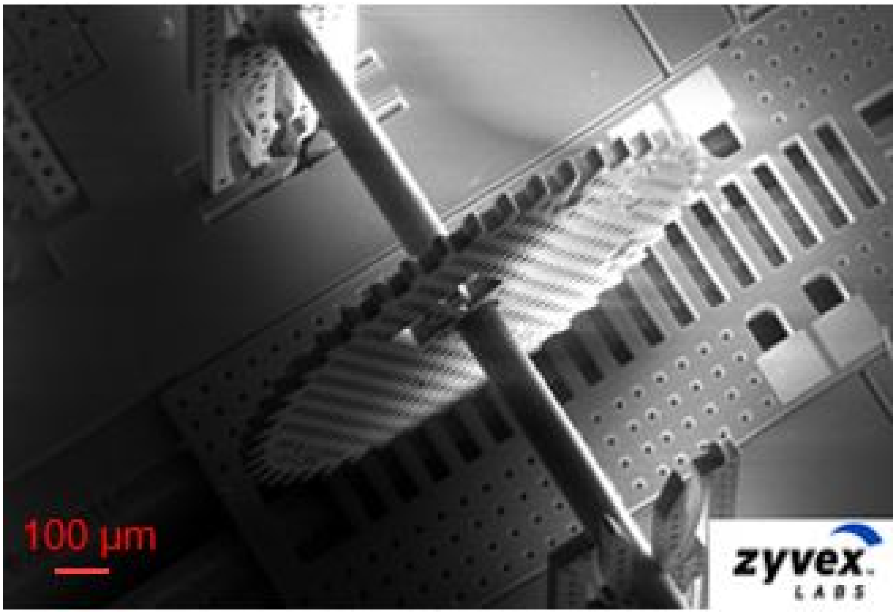

Figure I.4 – Gear assembly on 100 μm tungsten wire [Zyvex 20] according resulted positioning), it becomes important to introduce an intermediate methodology to interact with such fragile systems. To go ahead in such a direction, assembly of the micro-structures using natural and/or introduced interaction forces activation (by means of dedicated functioning) can also bring interesting results. The general principle remains in such approach of the self-assembly technique is to reach a minimum energy state. The different works such as [Yao 19, Percástegui 19, Liu 19, Gao 20, Wang 20b, Chang 17] demonstrate the potential use of the self assembly. Such an approach is very useful as it minimizes direct interaction of the user with micro-structures and also it manages to provide the desired accuracy. Although such an approach has wide applications, but still the lacking factor in the approach of the self-assembly is the generalization of the concept for varieties of micro-structures in terms of their shape, size or the functional properties. Therefore, there is requirement of system(s) that can work as an intermediate driving system between human and the micro-structures which can be operated according to the need (robotized system). The robotic system can operate in two ways with the micro-structure, either embedded actuator with robot (tethered mode) or no embedded actuator with the robot (untethered mode). The untethered robotic systems such as [Youssefi 19, Wang 18, Wang 19b, Zhang 19] can be used for handling of the micro-structures but are mainly designed to work in a dedicated workspace, and therefore the performances are likely to be affected by extending the use for variable assembly requirements (changing the workspace medium, size, or the change of micro-structure of interest). Therefore to meet the varieties of assembly requirements at the micro-scale, a tethered robotics system can provide capability to handle diverse micromanipulation tasks. Tethered micro-robotic systems [Ma 19], [Liu 17], [Yang 18] demonstrated their wide capability to meet the manipulation for assembly. To meet the various needs for complex tasks at the micro-scale, there is requirement of the appropriate system.

Industrial works such as [Zyvex 20] employed tethered robotic system, where gear assembly was done on 100 μm tungsten wire using a defined pick-and-place function. The driving of the assembled gear was from stepping rack meshing below the gear which moved by the thermally actuated fingers. Robotic system should be able to address the different challenges along with meeting the defined task objective(s). Especially when there is requirement of multi-states knowledge for the decision making. In [Shang 20], a feed-forward compensation control based strategy is proposed to make rotation of 90 μm diameter sphere, the approach used estimation of the contact force, identification of different kinematic and dynamic parameters and the feedback from camera in decision making. The approach considered no deformation of microsphere (metalic), and a symmetrical structure to be sure about the uniform pixelic measurement into consideration of decision making. While [Liu 20] demonstrated 3-D orientation and releasing capability (shown in Fig. I.5) with a Dual-Probe-Based Micrograsping system. The force information was estimated by measuring pixelic deformation of the probe at contact point. In practice, dealing with a non-symmetrical micro-object such an approach may not be applicable in the form it is used, because the rotation measurement then would need 3D pixelic information. Especially in the case where the

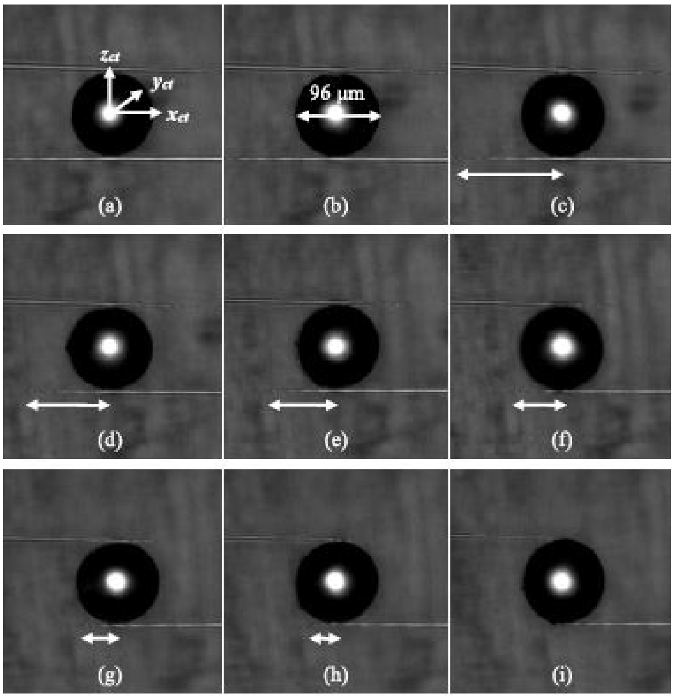

Figure I.5 – Releasing strategy used in [Liu 20], (a)-(i) sequential images during the release

micro-structure used, is undergoing some deformation, then also the approach may require additional state(s) information. Similarly, the peg-in-hole micro-assembly needs multi-state(s) information, which can be achieved by several means. In [Chang 16], an augmented reality technique was used to work with vision-based sensing as shown in Fig. I.6. In such an approach a virtual micro-assembly system was generated using a CAD model (calibrated with real time system), which then used an online error correction with the information from camera (real system) and the virtual system. Such a method requires 3D model generation for a defined workspace, and a dedicated systems like gripper, micropeg and hole is used with the use of 3D reconstruction from 2D image features. The technique used may not be adequate enough to meet the challenges from the environmental uncertainties (shadows, contact forces etc). The use of vision for the localization of the hole is indeed a valid need, but there is requirement of an online interaction data of peg with the hole. In [Shen 19], multi-dimensional forces and torques information was used to make an automated peg in the hole with control strategy. Such an approach provides the capability to perform various insertion tasks, not limited by a dedicated workspace or choice of the peg or hole. The used force/torque sensor was commercially available ATI Nano-43, which has a force and torque resolution respectively of 7.8 mN and 0.050 N mm, for respective range of ± 18 N and ± 250 N mm. The respective diameter and height of peg and hole were, 8.012 mm × 10.085 mm and 5.002 mm × 9.013 mm. The matching gap between the outer diameter of the peg and the inner diameter of the hole was 50 μm, which is still a large value in context of the micro-insertion task, where the typical accu-

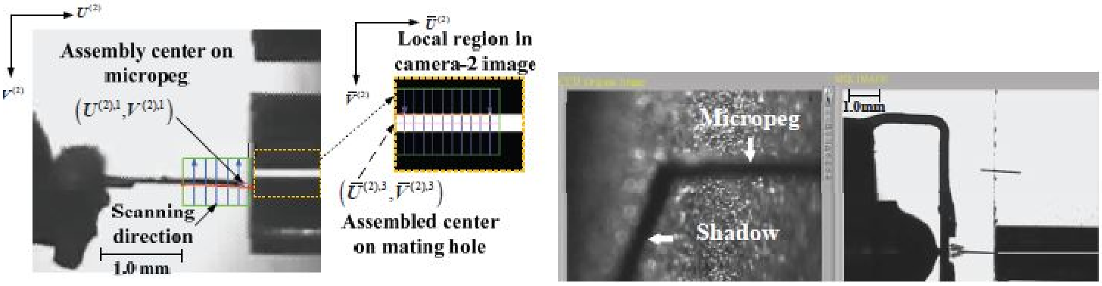

(a) Vision based detection of micropeg tip position and mating hole's end position (b) Assembled peg-in-hole (left: observed by Camera, right: observed by Augmented Reality approach

Figure I.6 – Peg-in-Hole micro-assembly used in [Chang 16]

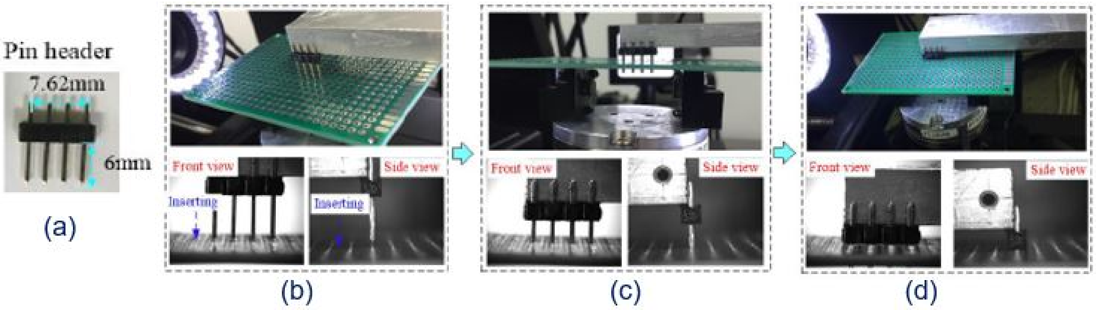

Figure I.7 – Multi peg-in-hole used in [Ma 20], (a) Pin Header with pegs (b)Before Insertion (c) During Insertion (d) Insertion Done

racy needed is within few μm. Same commercial Force/Torque sensor was used in [Ma 20] (Fig. I.7), where insertion of multiple-pegs were made using demonstration learning and reinforcement learning. The force/torque information facilitates the decision making capability for such complex tasks, but for micro-insertion, a dedicated force/torque precise sensing is needed. The instrumentation which can meet the micro-scale challenges in order to handle the fragile structure effectively and throughout the phase of the task handling, is required to be considered. The objective is to have the necessary and precise information of state(s) needed to implement the desired task. Then, the according adequate control strategy would be required to implement the action by using the information of the state(s) and the constraints.

In [Wang 19a], a displacement/force switching controller is used to meet the requirement of grasping of a 80 μm diameter copper wire. For the force sensing along the gripping axis, strain gauges were used and to have the position information, an external laser sensor was used. The task validation was done along a single axis, but the force/position state information is needed to perform such tasks. The force information along with precise positioning is significant in making interaction of the gripper with the micro-structure. In [Das 20] a piezoelectric actuated microgripper is proposed capable of a actuation with ± 10 nm resolution but to perform grasping of 540 μm wire, an external strain gauge was attached to the microgripper stationary jaw in order to have the grasping force information. In [Komati 16a], piezoelectric actuation was used but both the fingers were instrumented to sense the force (piezoresistive sensing), which allowed the grasping of multi-stiffness object without need of any external sensor. Safe manipulation of a fragile micro-object with unknown compliance requires the force and/or deformation information during the phase of manipulation. The sensing capability then needs to be extended in order to tackle the complex tasks like rotation, insertion without dependency on modeling alone.

I.3.3 Micro-assembly with glue

Assembly of the two surfaces can be made in several ways, like a dedicated insertion mechanism leading to fixation of the two surfaces or by using a bonding adhesive in between. Micro-assembly has a strong industrial interest, and in most of the needs there is requirement of a precise positioning (accuracy below 1 μm). In majority of the cases the aim is to hold the two surfaces with a desired relative distance over a long period of time. There were several approaches used and proposed for micro-assembly, depending upon the modes of operation required. In [Cui 18], a rapid aqueous process based self-assembly of nanoparticles has been presented, whereas the assembly of modular and polymer-based microfluidic devices has been investigated in [Lee 18]. Micro-assembly with very high accuracy has been demonstrated in several works, such as for optical components positioning [Bettahar 17] and assembly of flexible structures [Komati 16b],[Xing 18], but gluing tasks for a micro-assembly have been little investigated, despite being very widespread [Chang 10]. The gluing in itself has many challenges, which depends on its intended use. Glue in the liquid phase introduces the capillary force on the structures to glue which may be considerable depending on the size (as shown in Fig. I.3 for surface tension). The extent to which the micro-structure can be affected is dependent on the glue quantity, its shape, and also on the shape and size of the structures. The capillary action alone can significantly influence the final positioning of the structures in contact. This can be seen, where the capillary force was used for the assembly, especially in the context of self-assembly. In the self-assembly scheme (Fig. I.8), the behavior can be forecast depending on the fluid quantity, meniscus and the surface geometry in contact. In such an approach the choice of fluid, its viscosity is indeed additional factor to consider, especially in terms of the intended positioning from the capillary action.

Therefore the two points in the gluing context need to be considered, first the behavior in its liquid phase (capillary effect), secondly consequence from the curing of the glue. There could be several possibilities in the use of glue, either the glue quantity and its shape need to be controlled and/or the glue impact on the structures need to be controlled by some direct means. Majority of the gluing tasks (at micro-scale) in industries are done manually, where the obtained final positioning is based on the expertise of the assembler. Other than the glue quantity and its shape control (which are indeed difficult to do manually), the final

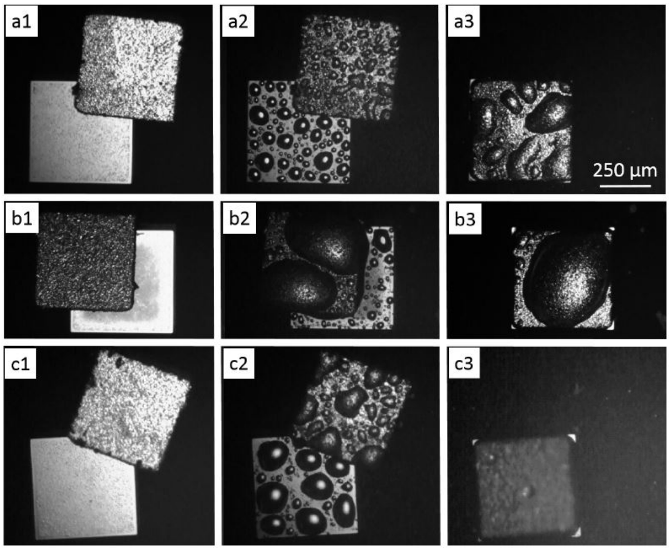

Figure I.8 – Capillary self-alignment in [Chang 17], (a1),(b1) and (c1) chip was placed on a receptor site; (a2),(b2) and (c2) water mist induced droplet introduces at the assembly site; (a3), (b3) and (c3) self-aligned chip at the receptor site

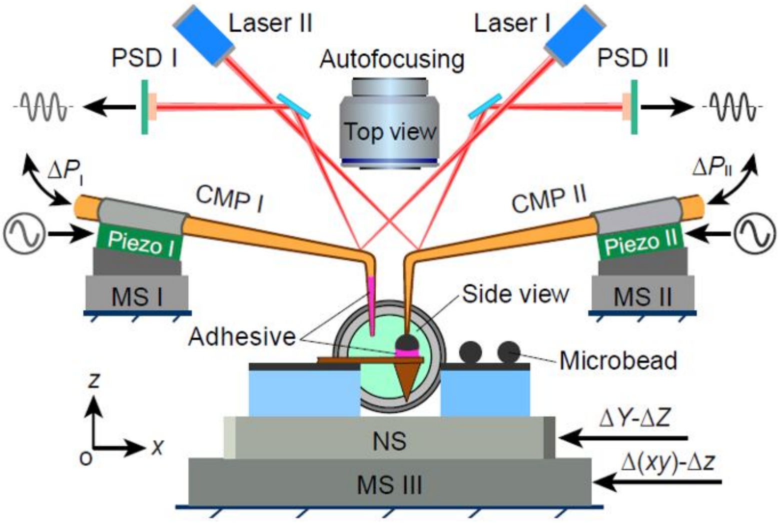

Figure I.9 – Schematic of the Gluing system used in [Xie 18] positioning of the glued product is also dependent on the choice of the glue (the material properties), and the curing process. Therefore, it appears that there are multiple potential parameters which can affect the positioning of the glued product, therefore an intermediate system is needed for a precise gluing. In [Xie 18], a micro-assembly system was used which included two cantilevered micropipette probe (CMP), each of them can be controlled to generate necessary vacuum. One of the CMP, named CMP I was used for adhesive deposition, while other (CMP II) was used for pick-and-place (schematic is shown in Fig. I.9). Also, to measure the interaction force, an optical lever consisting of position sensitive detector (PSD) and a laser was used. Meaning which, the force measurement is external to the interacting tool, and in such cases the two frames (of sensing and tool) must need to be relatively known and sometimes fixed (to be in the sensing range of the position detector). The glue (adhesive) quantity was controlled with the help of vacuum pressure control and typically the quantity of glue was much less (a thin layer) compared to the micro-object used. Therefore positioning was not affected considerably by the curing. The gluing quantity may affect the required holding pressure of the micro-object during the curing, and this side can affect the final relative positioning of the structures.

In order to have a precise, flexible and robust micro-assembly capability, the different key requirements can be listed as:

- Multi-axis and precise knowledge of assembly system's state(s)
- Long range state(s) information for flexible tasks handling
- Compatibility over a high bandwidth
- Precise and multi-axis actuation
- Adequate control strategy to meet the desired speed and accuracy
- A compatible interaction tool/gripper for the desired task

Precision, range, and choice of control, need to be considered in the design based on the requirement of task of interest and therefore is not quantified. At the micro-scale, it can be said that the ideal situation would be when instrumentation of the robotic system allows the lowest change detection over a highest range possible. These lowest and highest limits, need to be considered based on the targeted task. The different possibilities of instrumentation, their merits, limitations, the targeted specifications from the state-of-the-art works discussed is presented in section I.4.

I.4 Instrumented system development

As defined objectives in section I.3, the multi-axis instrumentation is an important concern in the micro-assembly context, and therefore different possibilities need to be studied for an adequate instrumented system development. Talking about the possibilities of instrumentation, there are several feasible principles possible. A comparative study of different widely used sensing approach is listed in Table I.1, with their corresponding key advantages and disadvantages. All listed principles allow to have a sub μN resolution, and therefore the according system design and signal processing feature needs to be analyzed to have adequate system for the desired task. In the context of force sensing, when an external load is applied to the structure of interest (where force needs to be measured) undergoes strain. This strain can be mapped to a force measurement, which can be done by use of a reference force sensor.

$$f_{ref} = s_{cal} \times m_{state} \tag{I.1}$$

Eq. I.1, defines a general equation of force sensing, where f_{ref} is the force sensed by a reference force sensor (calibrated), m_{state} is a measured state that needs to be used for force measurement and s_{cal} is a calculated scaling factor (called sensitivity) for mapping of m_{state} to f_{ref}. In this equation, there are two key assumptions included, first in the linear dependency of m_{state} on f_{ref}, while second in the single state m_{state} dependency over force measurement along a given axis. It is possible to have a non-linear relation between f_{ref} and m_{state}, and also to have a dependency of f_{ref} on multiple states (case of coupling). A simplified version is used here to address the sensing principle, and therefore according changes can be included if its relevant. An elastic beam when subjected to an external load (using a reference force sensor) at its tip end will undergo deformation, the extent will be dependent on the intensity of the load. If displacement of the tip is measured by an external position sensor, then displacement sensed (m_{state} here) can be transformed to measured force f_{ref} from the reference force sensor, which results into calculation s_{cal}, which is the stiffness of the beam (need to be calculated from the equivalent stiffness of beam and reference force sensor). The sensor development depends mainly on two factors, first on the choice of m_{state}, second the principle used for measurement of m_{state}. If displacement of the beam's tip is m_{state}, then this could be done by use of an optical sensor or by use of vision based sensing. Elastic behavior of structure allows to have calculated scaling factor s_{cal} unchanged, and therefore the structure can be used as a force sensor with measurement of m_{state} alone. Indeed, depending on the material and geometrical parameters, there will be a life-cycle of any structure to withstand a constant elasticity and so the s_{cal}. Displacement is m_{state} also in case of vision based sensing [Adam 19]. It allows easier experimental implementation with a reliable measurement over a long range sensing capability. Use of an adequate camera makes the system expensive, and with magnifying objectives the overall system may get bulkier. The limitation in vision based sensing also is in its focus depth. But, indeed this approach is very useful for a precise and long range planar sensing.

Optical based sensing is not limited with its use of displacement as m_{state} but it can use some of the dedicated approaches such as Fabry-Perot Interferometers (FPI), Fiber-Bragg Gratings (FBG) or Light Intensity Modulation (LIM). Starting with LIM [Noh 16], this approach is based on the light intensity detection

Principle	Advantages	Disadvantages
Piezoresistive	• Easy implementation • Large range	• Temperature sensitive • Humidity sensitive
Capacitive	• Low power consumption • High sensitivity • Large bandwidth	• Circuit complexity • Noise sensitive
Optical	• High spatial resolution • Imune to electrical noise	• High cost • Small range
Vision	• Easy implementation • High range	• Low focus depth • Expensive • Bulky

Table I.1 – Comparison of major sensing approaches used for micro-scale applications in terms of voltage measurement, therefore m_{state} is voltage which is function of light intensity. A rotating mirror (or a modulator in general) can be fixed at the end of an optical fiber which leads to the intensity variation detection under the presence of external load. This optical method is costly and corresponding performance are likely to be affected in the presence of bending of fiber. Whereas FBG [Shi 19, Li 19, Li 20a], uses a diffraction grating formed in the optical fiber. This grating selectively modulates the reflected light where the constituent spectrum changes with external load. The other very prominent approach in optical force sensing is FPI [Dash 19, Wei 19], where a dedicated MEMS is attached at the end of optical fiber, such system allows the detection of introduced load in terms of optical spectrum change where m_{state} is wavelength change measured. As a whole, optical sensors can provide high spatial resolution with high repeatability. The key advantage remains in its immunity against the electrical noise. Depending on several possibilities of optical sensing, cost in general is still high with the employment of suitable fiber. Electrical circuitry are often used in the sensors development, the main approach used is the voltage change detection as function of the application of external load, which means m_{state} as voltage. From the material side, the question comes is about the choice of material which can allow a voltage change detection against the applied load. One very common electrical circuitry used for voltage change detection is “Wheatstone Bridge” based circuitry, where the electrical resistance change can be transformed to voltage change detection. To go ahead in such direction the resistance property of structure need to be considered. This resistance feature should not solely be dependent on the electrical resistance alone, but can be reflected in terms of the reactance. Also it is possible to use directly, the resistance/reactance change as m_{state} against the force applied. It depends on which choice suits the specific signal processing requirements. Charge storage capacity of the material, which can allow the measurement of capacitive reactance or capacitance, can be mapped to force. The corresponding structure which exhibits the change of capacitance [Na 19] under the applied load, can therefore be used as a force sensor. The capacitive sensor design therefore need to consider the dependent parameters on capacitance, such as electrode area, size, or dielectric medium. Capacitive sensors can allow a high sensitivity over a large bandwidth, but the according circuitry might need special design in order to minimize the noise influence on the performance which may result into complexity in the circuitry. Under the external load application a piezoelectric device undergoes change in the electric charge and so do the capacitance which then can be measured to map to the force. Piezoelectric device [Morales 18, Lee 20, Liseli 17] can be used as a force sensor, but the performance of device would be limited by the minimum capacitive change detection. Depending on the choice of the material and geometry, the extent of change in capacitance against the external load applied, may limits its use for micro-scale applications. The other features which can be used for the reactance change can be inductive. An inductive reactance or inductance change can also be used to measure the force. This requires, the change of inductance [Yeh 19, Wang 20a] of the structure against the external load. This choice is very limited because of additional complexity in the device

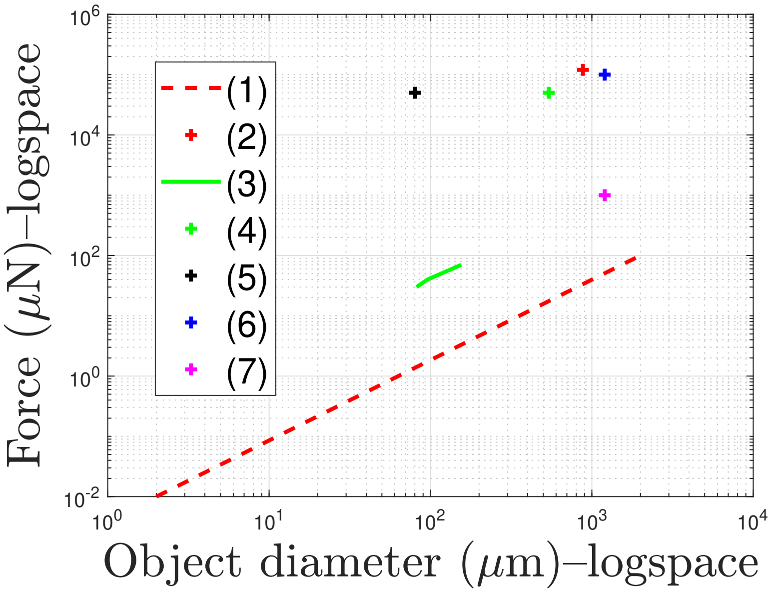

Figure I.10 – A comparison of different force sensing from the state-of-the-art

fabrication and large influence of noise in the signal processing. A piezoresistive device exhibits a direct change in electrical resistance under the applied external force, and this therefore can be used for force sensing. The resistance change can be directly used as m_{state} or as said, it can be used to make voltage change as m_{state} using a dedicated wheatstone circuitry. Such devices are relatively easy to implement as a force sensing device, also it can allow a high resolution measurement over a long range. Indeed, the sensitivity and according performances would be dependent on the choice of the piezoresistive material, geometry and according signal processing. The limitation of such a sensing approach is in environmental constraints, as resistance change is dependent on the temperature and humidity, therefore the environmental conditions must need to be in accordance with the material properties of the device. A state-of-the art survey is included in [Wei 15], which compared different force sensing techniques for micro-scale applications. Every sensing principle has some pros. and cons., the choices then need to be made based on the candidate which closely meets the targeted performances under the defined constraints.

The targeted instrumented system must exhibit a repeatable behavior, but in terms of its range and resolution, it needs to be defined based on the targeted work. From different discussions in section I.3, the minimum and maximum force range measured in different works can be used to define the targeted specifications. Surface forces such as van der Waal's and surface tension are also useful for handling of task. The range of force needed to be sensed dependent on the size of the object (interaction area) and the stiffness. Different tasks such as [Wang 19a] and [Das 20], considered a non deforming object (in the corresponding force range) but works such as [Xing 18] and [Komati 16b] considered deforming object. Force mea-

Works	Reference
(1)	[Neugebauer 11]
(2)	[Ma 20]
(3)	[Liu 20]
(4)	[Das 20]
(5)	[Wang 19a]
(6)	[Xing 18]
(7)	[Komati 16b]

Table I.2 – State of the art References for Fig I.10

sured against the object diameter is included in Fig. I.10, where for [Komati 16b] width of the structure was considered as diameter. Although, with variation in interaction area, size and stiffness, the required force sensing is difficult to quantify, but from the different works a system development may be targeted which can meet the sensing requirements of majority of the works at this scale. In a nutshell the force sensing capability from 1 μN to 100 mN would be of great interest for wide varieties of works targeted.

I.5 CONCLUSIONS

Microrobotics systems have demonstrated their potential application in almost every domain. With their capability to interact effectively with micro-fragile structure, they can be used for handling of complex micro-assembly tasks. Gluing for the assembly, being an important assembly approach need to be studied and especially in terms of requirements towards precise gluing (discussed in Chapter II). To facilitate handling of complex tasks including gluing; multi-axis instrumentation of the microrobotics system is needed. This instrumentation can be done to the platform and/or the system used for manipulation of the micro-component. Studies from the different state-of-the-art works suggest that instrumentation of the system with sensing capability in 1 μN to 100 mN would be of great interest. In this thesis work, instrumented systems development is therefore targeted. This would aim to cover instrumentation of the platform (Chapter III) and also a tool (Chapter IV) which can then be used for gripper development (Chapter V), all of these should be capable of multi-axis sensing. Moreover, micro-scale task handling capacity with the developed systems need to be demonstrated (Chapter V).

Chapter II

Analysis and robotics based precise gluing

II.1 INTRODUCTION

Gluing appears to be a key task of a micro-assembly process because it enables to definitely hold the relative position between two components. For most applications, the quality/positioning accuracy of the assembly directly impacts the performances of the final product. Most of the existing gluing tasks require very dedicated approaches, especially to use thin films using surface referencing and conditioning [Tennico 10],[Xiong 14]. For gluing two objects, even using a conditioned glue layer of ~ 20 μm can introduce significant error towards desired assembly (the typical needs to reach a positioning accuracy below 1 μm). Depending on the requirements, the thick glue layer can provide a wide range of desired distances between the two surfaces to be glued. In [Gakkestad 10], a 30 μm thick layer of conductive glue was used to connect a MEMS structure directly to a printed circuit board. Different applications of packaging, such as fiber fixation with a chip, might be made using a thick glue instead of using fusion splicing based dedicated approach, as used in [Nauriyal 18], but positioning accuracy then needs to be insured by some other flexible means.

Surfaces in contact with adhesive make huge contributions towards the behavior during gluing, especially their influence towards spreading coefficient and rate of spreading for the equilibrium stabilization [da Silva 11]. Moreover, the choice and quantity of glue also play an important role in final positioning [R.D. 84, Cognard. 10]. Glue curing induces stress around the surfaces under glue-contact, which would introduce positional shrinkage (between the two gluing surfaces). As a whole, use of thick film of glue can introduce significant positional drifts, primarily from capillary effects (surface-liquid glue interaction), followed by positional drift because of stress development during glue curing. The procedures needed to reach high positioning accuracy (below 1 μm) must account for these mentioned happenings. In order to have desired and repeatable behavior, there is requirement to have similar choice, quantity, size and shape of glue, along with similar surfaces to be glued (in terms of the size, roughness, shape). A small change in one or more of the mentioned parameters may result into different results than the targeted version. Therefore, there is a strong requirement of a flexible and versatile approach that could solve the complexity with sub-micrometer accuracy. To address this, we aim to use an active robot control strategy which could allow online track of gluing state and to make the necessary corrections so as to insure the desired positioning of the glued product. Indeed, this approach appears particularly generic, versatile, and flexible because it intends to adapt to all of the mentioned-above parameters change. In order to meet this challenges, force-position sensing and its accordingly use in development of control strategy may bring an important role in the decision making. Discussions in this chapter are focused on 3 studies, first the main effect of gluing on the surfaces in contact without any external load (applied force at the gluing end), second the impact of external load on the relative distance between the two surfaces during the process of gluing and finally to extend the studies to control the external load so as to reach a desired gluing of the two surfaces. The behavior resulted from gluing in absence of external load was primarily discussed (section II.2), then the limitation in analysis and the requirement to have an external load based analysis is discussed (section II.3). The gluing behavior with its dependency over the external load was analyzed followed by its use to estimate a control scenario in order to have a precise relative positioning of the gluing surfaces is also discussed (section II.4 and II.5). The continuation of the arguments presented is further experimentally demonstrated with an active control strategy for a precise gluing (section II.6). The entire analysis and the work discussed in this chapter is made along a single axis, which consist of major influence on the gluing surfaces (longitudinal component). It allows to make the key analysis, check the feasibility of the approach towards solution to the key problems, without adding any complexity in the system.

II.2 GLUE CURING IN ABSENCE OF EXTERNAL LOAD

The glue curing process in absence of any external load is discussed in this section. The objective of this study is to be able to have understanding of the shrinkage amplitude, its introduced force on the surfaces, when there is no load externally applied to the gluing system. Moreover, analysis of the corresponding behavior obtained in terms of the challenges towards a precise gluing is also studied.

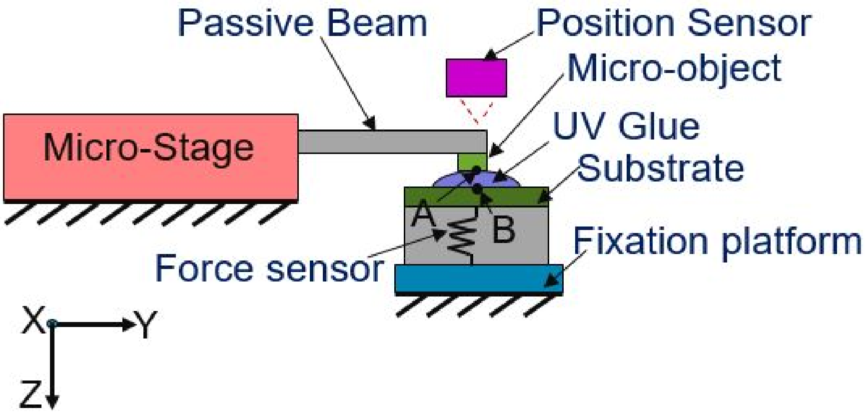

Figure II.1 – Schematic for the Gluing in absence of external load

The dispensed glue droplet size is 35 μm in height, and 315 μm in diameter (assuming uniform distribution around). The glue used was DYMAX 425, which is an UV curable glue, and DYMAX Blue Wave 50 was used as UV source for glue curing. The micro-object used is 500 μm × 500 μm in cross section, with 350 μm thickness, made of silicon is attached (using thermal glue) to the beam made of steel. The beam with the attached micro-object can be moved along Z, to go in contact with the glue (point A) as shown in Fig. II.1. This contact induces stress on the object because of the surface tension from the liquid meniscus and therefore, the glue-beam system allowed to get stabilized (fluidic stress release),

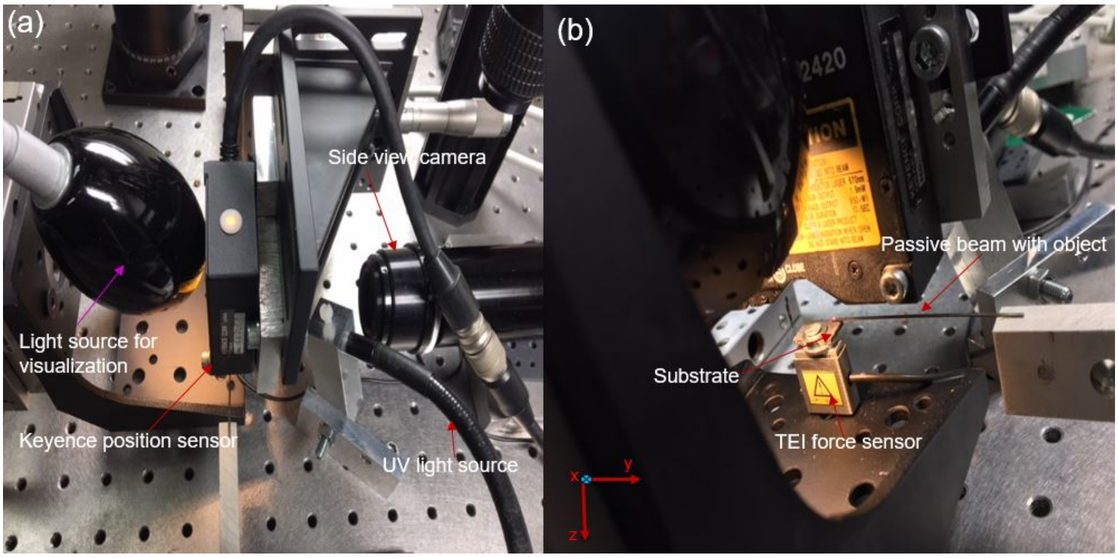

Figure II.2 – Experimental Setup for gluing in absence of external load: (a) Top view (b) Side View

where the stabilization of the system can be monitored with a position sensor (Keyence LC-2420 which works on a laser reflection principle) and a force sensor (TEI-FSB 101). Once the UV exposure was made (at about 180 seconds) the glue starts curing, and this resulted into development of stress in the beam-glue link. The resulted bending of the beam (and so the position of the object) was monitored from the employed position sensor and the force from the force sensor. The measured displacement y_A (Fig. II.3a) and the force F_A (Fig. II.3b), gives 6 μm of displacement and 0.15 mN of force respectively, as result of the glue curing.

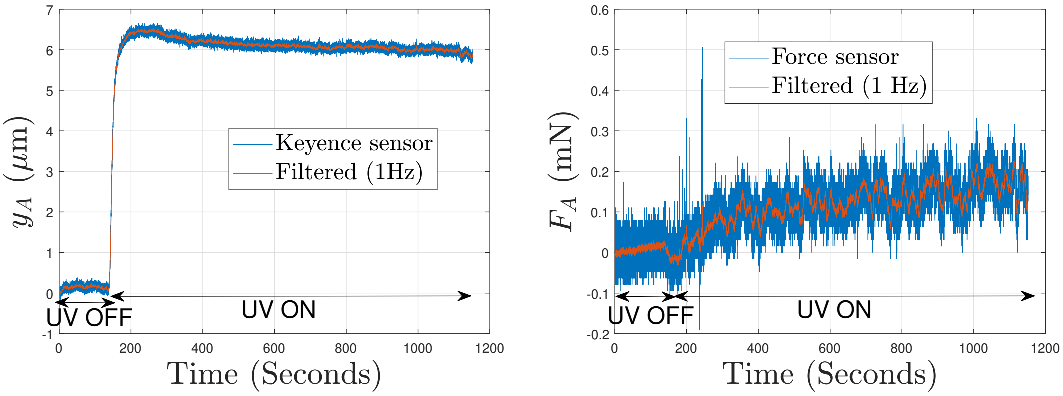

(a) Displacement from curing

(b) Force from Curing

Figure II.3 – Study of the behavior of a component during its gluing

The progress of curing process can be seen as the force or displacement growth, but the information of progress of curing is limited by the stiffness around the glue.

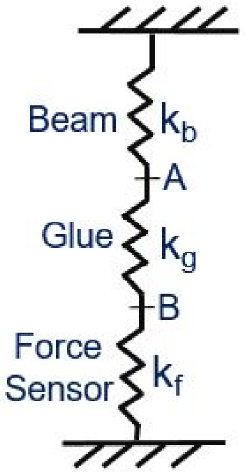

Figure II.4 – Spring model

$0 < k_g \leq \dfrac{k_b \times \ k_f}{k_f + k_b}$	(II.1)
$k_g > \dfrac{k_b \times \ k_f}{k_f - k_b}$	(II.2)

Table II.1 – Evolution of Glue Stiffness

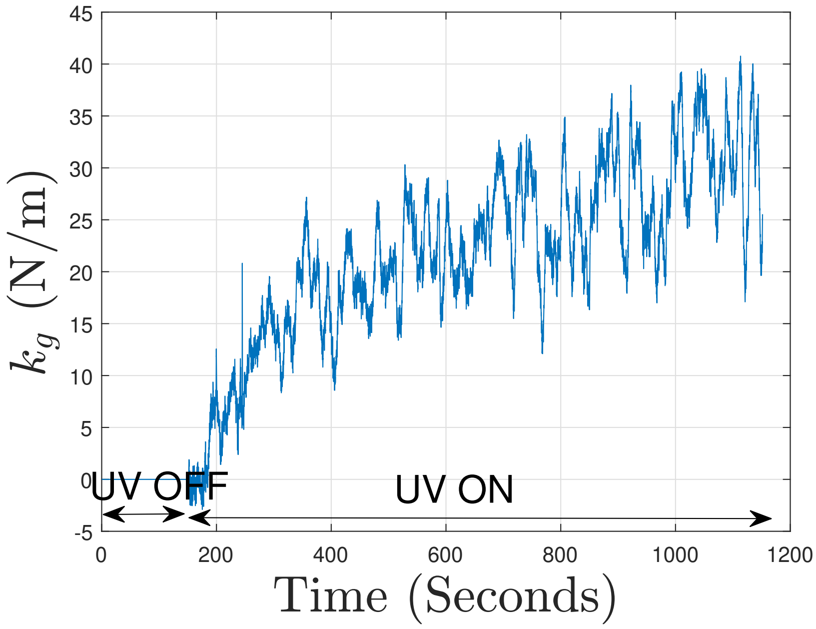

Figure II.5 – Calculated glue stiffness with 20 N/m passive beam

A spring equivalence model considering the static scenario is shown in Fig. II.4, where k_b is the beam stiffness, k_f is the force sensor stiffness and k_g is the glue stiffness. Following the curing of the glue, the resulted stress introduced on beam and the force sensor, allows to measure the glue stiffness evolution as defined in Eq. II.1 of Table II.1. The corresponding external shape change of the glue with curing is the only main source of the stress introduction on the beam and the force sensor, and this corresponds to static equilibrium situation. The internal layer of the glue doesn't introduces any stress on the surrounding compliance and therefore is not track-able (Eq. II.2). Therefore, there is requirement of an additional approach by which the glue curing extent can be monitored for the entire duration of gluing. One of the possible strategies could be the application of time-varying but known external load.

II.3 Glue curing in the presence of external Load

Curing in presence of a known time varying external load can allow the track of the entire curing phase, again the extent of track dependent on the application of load intensity and its variation with time. In this section, a time varying load is applied against the glue film to monitor the behavior before and during the curing. An experimental setup to analyse the behavior of the glue in the viscous phase and during the curing is shown in Fig. II.6, where Beam 1 is fixed to Nano Positioner (MCL Nano-3D200 from Mad City Lab), two position sensors (Keyence LC-2420) is used to monitor the Beam 1 and Beam 2 displacement. One end (which is not in contact with glue) of Beam 2 is kept fixed throughout the experiments discussed in this section. A side view camera (IDS USB 3 uEye CP camera, with 20x magnification objective from Mitutoyo) is used to visualize the glue meniscus against the beams.

Beam 1 is allowed to go in contact with the glue which is placed at the tip of Beam 2, and allowed to properly stabilized following the viscous and residue stress release. A sinusoidal input displacement of Beam 1 is made from the Robot 1, which lead to the stress imposed on the glue (Fig. II.7b, where t is time spend during the gluing). Both of the beams, Beam 1 and Beam 2 are of stiffness 167.5 N/m (respectively defined as k_{b1} and k_{b2} of Fig. II.7a). In absence of UV exposure, under the introduced motion of the Robot 1, position A (d_A), Beam 1 tip position d_B followed displacement, whereas no considerable displacement is noticed of Beam 2 tip C (d_C), which means, the introduced stress from the Beam 1 motion is within the dissipation limit of the liquid glue alone (very low stiffness of the liquid glue compared to the Beam 2 stiffness, and so no dissipation). Moreover the position d_A and d_B, followed almost same amplitude of displacement in absence of UV but with a very small delay in their actuation, which means the liquid glue is acting as a phase delay element with no any considerable dissipation. Once the UV exposure is made, then the glue starts curing, and a very fast transition of phase happened (marked as “Curing” in Fig. II.7b). During this transition phase, the Beam 2 starts moving, as a result of formation of link between point B and C. Once the link is sufficiently cured then a constant amplitude displacement of point B and C can be seen (marked as “Cured” in Fig. II.7b).

Ideally the input displacement from the Robot 1, and the output displacement of the Beam 1 should follow a linear relation if there is no any phase delay in-between. But, as it is seen that there is presence of some delay, then the presence of hysteresis is expected in the liquid phase of the glue. Once the glue is cured, then the delay in-between, is removed and then there should not be any presence

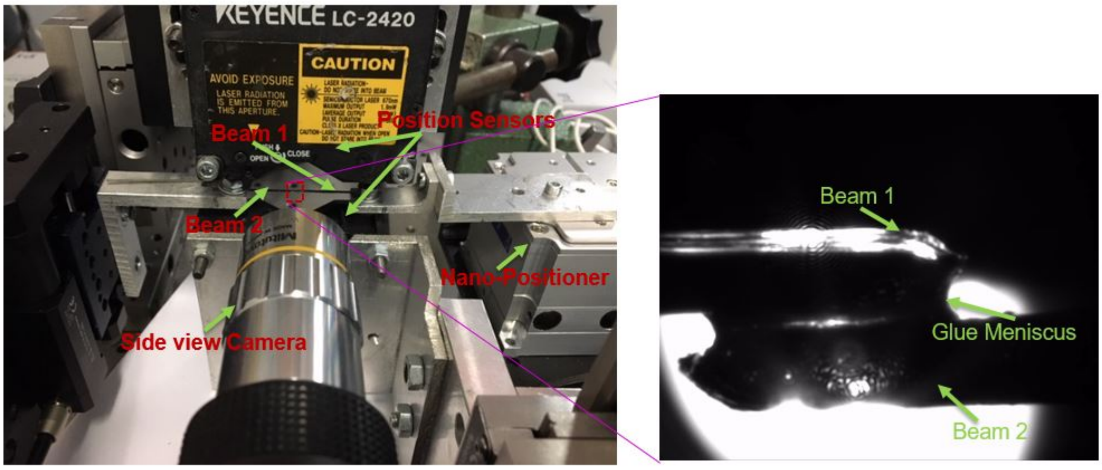

Figure II.6 – Experimental setup for Glue behavior under external load

of hysteresis, but depending on the timing of start of UV exposure there may be component of residue stress helping one way motion than the other way, leading to the presence of the hysteresis. In the presented experiment, the obtained hysteresis in the liquid glue, its transformation phase and the cured phase is shown in Fig. II.8a. Although, the hysteresis in the cured phase is much lower than that of the liquid phase but the presence is noticeable. The formation of link between the point B and C as a result of curing can be seen in terms of the evolution of the glue stiffness. Under the static equilibrium consideration, the force introduced on the glue is beam stiffness times the beam deformation, whereas the glue displacement is the shrinkage between point B and C (i.e. change of d_B-d_C), which is defined as change of d_{BC} (i.e d_{BC} = d_B-d_C). A plot of the force resulted on beams (f_A = stiffness of Beam 1 × displacement of point A) against the d_{BC} of the glue is shown in Fig. II.8b, where during the liquid phase force-displacement relation is almost horizontal indicating the negligible stiffness of the glue, while a very rapid transformation from horizontal to vertical slope can be seen under the exposure of the UV. The marked curing phase is the transition phase which includes the change of the slope and so the stiffness. Indeed the glue stiffness can not be concluded to be infinite from the vertical slope of the Force displacement, but it suggests the stiffness is significantly high compared to the stiffness around the glue.

The intermediate slope in the transformation phase of the glue suggests that the glue stiffness is higher than 100 N/m, a further track of this evolution may be possible with lowering of the curing speed and/or increasing the load amplitude with time.

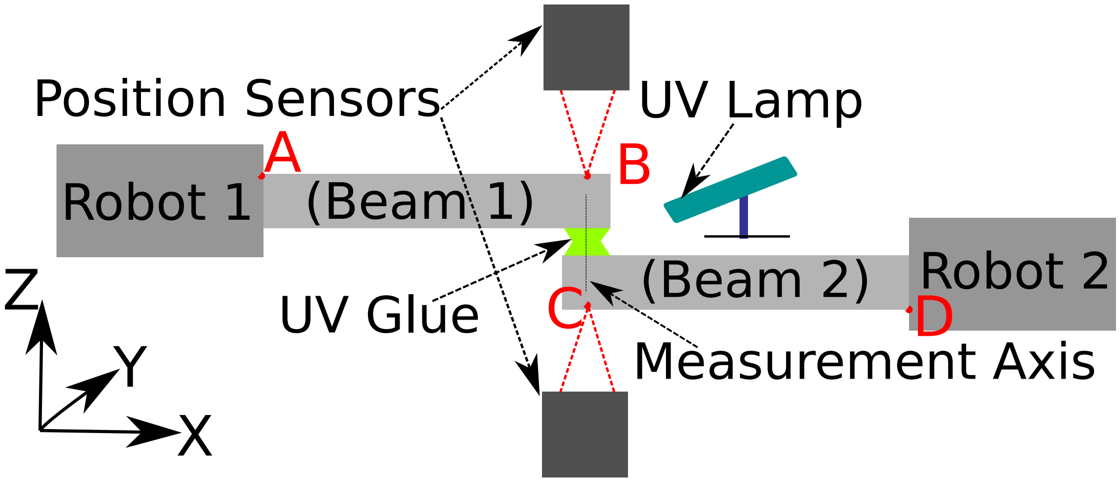

(a) Beams schematic

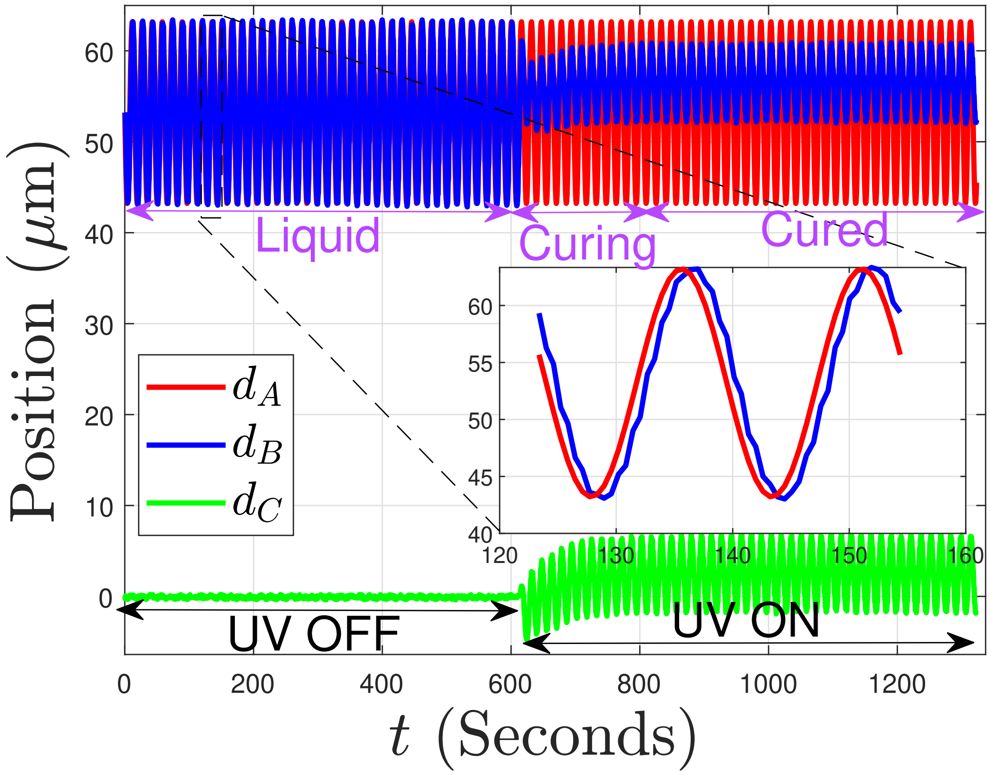

(b) Displacement of beams

Figure II.7 – System representation and behavior during gluing

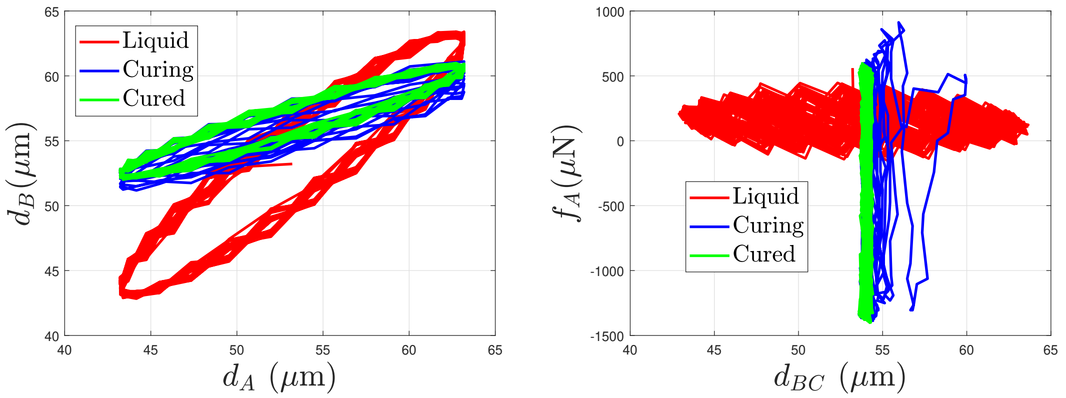

(a) Hysteresis presence

(b) Evolution of stiffness

Figure II.8 – Hysteresis and stiffness evolution during gluing

II.4 MODELING OF THE GLUE SHRINKAGE

In the continuation of the experimental observations and analysis made in the previous section, shrinkage of the glue can be modeled. Such modeling can help to estimate the different requirements such as external load actuation, the shrinkage influence dependency on the stiffness around, choice of the mechanical properties etc. The extent and dynamic of shrinkage are dependent on many parameters like quantity of glue, meniscus shape, UV exposure intensity, choice of the UV glue etc. A black box model may be done using design of experiment by keeping few parameters fixed, but in the current context, the objective is to analyse the requirement and difficulties to use the glue for the precise micro-assembly. Glue followed a sinusoidal compression and elongation against the applied sinusoidal load in the absence of the UV exposure, but an exponential reduction in the distance was seen as result of UV exposure. It was also noticed that in the very beginning of the exposure, the oscillation existed with lowered amplitude but later, no influence of the introduced oscillation. This means the stress from the curing became significantly stronger compared to that from the introduced oscillatory load. Modeling of the shrinkage resulted from the curing can be done with inclusion of the two components, first the glue shrinkage as a result of its pure curing, second its impact from the introduced external stress. The first component from the curing alone is stronger in the presented case Fig. II.9, because at the end there is an overall reduction in the distance between the beams. If t_u is the time when the UV exposure was introduced then the curing shrinkage parameter C(t) can be defined as in Eq II.3, where p_i (i= 1 to 8) are the parameters that can be identified to fit the exponential decay. This equation is simply a function used for modeling s-shaped behavior, which is the case in the current context where we have inverted s-shaped behavior (as used for shrinkage strain model in [Hossain 09]).

$$C(t) = \begin{cases} 0 & \text{if } t \leq t_u \\ p_1 e^{(\frac{-p_2}{t-t_u})^{p_3}} + p_4 e^{(\frac{-p_5}{t-t_u})^{p_6}}, & \text{if } t > t_u \end{cases} \tag{II.3}$$

The distance between the beams under the contact with glue is dependent on the introduced motion at the end B. If there is no curing, the displacement of point B will directly define the distance d_{BC} between the two beams, this dependency would continue even during the curing but with reduced impact. But at the end of curing there won't be dependency, once the link is fully cured (assuming we don't intend to break the cured link). This behavior can be formulated into the Eq. II.4.

$$\hat{d}_{BC}(t) = \int_0^t [(p_9 d_B(t) + p_7)\frac{dC(t)}{dt}]dt + p_8 C(t) + d_{BC}(t_u) \tag{II.4}$$

$\hat{d}_{BC}$ is the estimate of the distance between the beams, $d_{BC}(t_u)$ is the distance between the beams at the starting of UV exposure, d_B is the displacement of the point B, and p_7, p_8, p_9 are the parameters to match the obtained behavior. The structural formulation of the Eq. II.4 is defined by following considerations:

- Final distance between the beams should be directly dependent on the initial distance, before turning ON UV, i.e. $d_{BC}(t_u)$.
- Turning on UV, the distance between the beams would follow shrinkage, term proportional to C(t).
- Distance between the beams should be also dependent on the external displacement introduced at B i.e. d_B.
- The dependency over the displacement of point B must need to be dependent on the exposure time of UV (i.e. integral action required).
- The point B displacement must need to be a multiple of curing extent, so that when the glue is fully cured the distance between the beams can't be changed, assuming the intention is to not break the link (to include derivative of C(t) as a multiple of $d_B(t)$ in the integral).

Parameters p_7 and p_8, could be combined together, but is differently used to split the constant dependency of the solver used.

In Fig. II.9, the distance d_{BC} with its corresponding estimate is shown with respect to time. The parameters were identified using non-linear least square fit method and are shown in the Table II.2.

The obtained modeling helps to further make an in-depth investigation like to analyse the situation under the load impact or in other word to vary load to generate the desired situation.

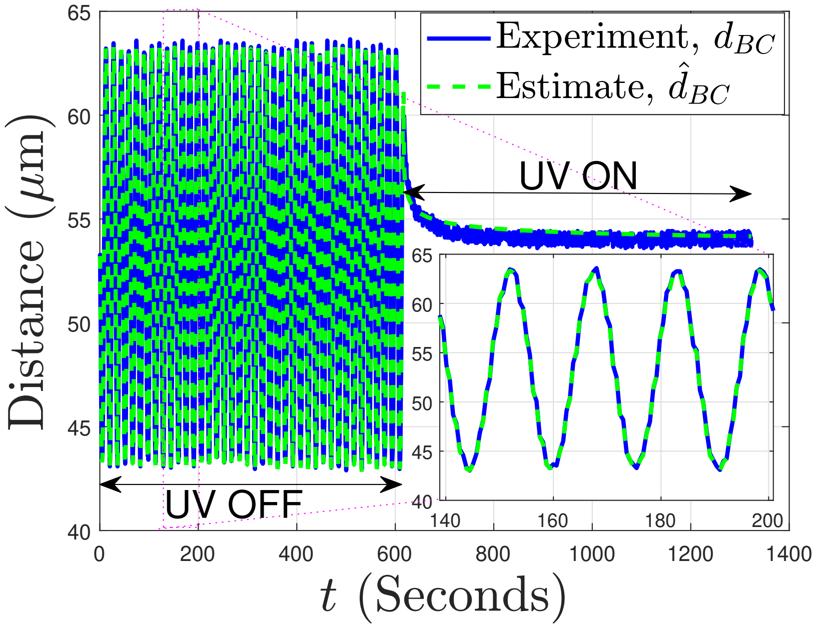

Figure II.9 – Modeling of the Glue shrinkage

Parameters	Values
p_1	0.167
p_2	0.003
p_3	0.412
p_4	0.174
p_5	3.774
p_6	0.374
p_7	1.019
p_8	1.019
p_9	0.545

Table II.2 – Identified Parameters for shrinkage modeling with load

II.5 Study of active control to achieve accurate gluing

As the glue curing process induces mechanical stress and so a drift, there is a requirement of an adequate action that can restrain this additional drift. There could be several approaches to solve this mismatch. In [Müller 15], shrinkage compensation from UV-curing was addressed using identifying critical parameters of curing. This identification was made by numerical simulation with knowledge of the sensitivity of the isolated degree of freedom, and accordingly, bonding direction was used. But this approach has its limitations: primarily from the choice of glue, and secondly from its convenient adaptability towards the micro-assembly process. Another possible approach could be to manage the viscosity variation to restrain the possible reshaping of glue arising from the glue curing. In [Roca 12], one apparatus is proposed with which viscosity adjustment of UV adhesive could be made. But mapping up the viscosity adjustment with the micro-assembly might further limit the workspace and the strategy towards assembly, as there might be other factors (such as choice of glue and cured strength) that complicate the chosen approach. With the knowledge of physical happening and its use in the approach, it could be possible to further improve the flexibility of the approach (towards force/position-based control).

There are multiple ways to address this problem; one would be to go with the approach of force/position control. To solve the problem of desired relative distance resulting from positional drift, one approach could be to track positional shrinkage, and accordingly generate sufficient force against the glue curing, thereby avoiding the drift introduced. This case is quite similar to that of grippers end-effector against the dynamic environment. An impedance control-based approach to estimate the unknown environment's parameter using force tracking is presented in [Komati 14b]; the approach was tested with different compliant structures. In [Wang 17], the force sensor was used to detect the penetration force against a biological cell, and a strain-based sensor to measure the relative position of the micropipette. With knowledge of force/position, an incremental PID controller was proposed to meet the suitable injection force. Another similar situation could be the case where the teleoperated task needs to be done against the dynamic environment, resulting in a requirement of force/position knowledge to develop suitable behavior. This case was addressed in [Lu 18], where a fuzzy-observer based hybrid force/position control method was used for a bimanual teleoperation system in the presence of dynamic uncertainties.

Combining these several studies, in the context of glue curing, an active control-based strategy to control the distance between the beams appears promising. Beam 1 would be allowed to find a suitable position to have sufficient force at the assembly end, through which the desired distance between the beams can be obtained. The employed load in the presented experiment was not strong enough to fight against the shrinkage. Assuming the similar conditions in terms of the glue choice, shape, quantity and analysing the behavior in terms of load dependency, a zoomed section

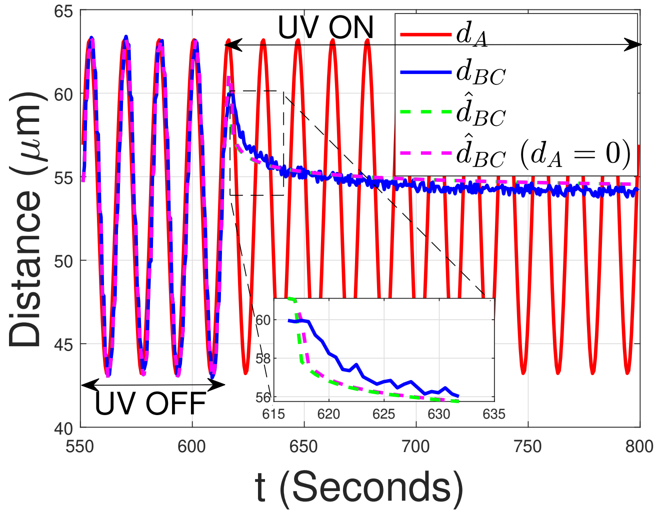

Figure II.10 – Negligible impact from the employed load; d_A=0 correspond to no displacement from Robot 1 (as shown in Fig. II.7a)

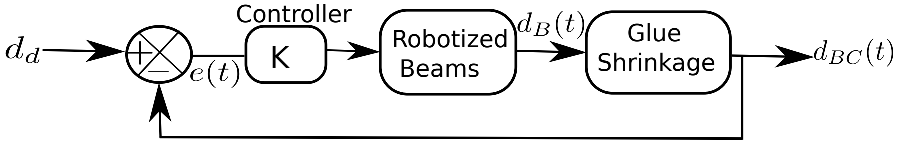

Figure II.11 – A feedback control to insure a desired distance between the surfaces

of the previously presented experiment is shown in Fig. II.10. The behavior in presence and estimated in absence of load are very close. A situation where we intend to use the gluing for micro-assembly, then the positioning accuracy becomes more important.

To analyze the scenario where we intend to have always a desired distance between the two gluing surface (beams here), then a feedback control is proposed to carry out this task.

A control schematic is shown in Fig. II.11, where d_d is the desired distance, and K is the controller gain, $d_{BC}(t)$ is the instantaneous distance between the beams (point B and C), e(t) is the error (i.e e(t)= d_d -$d_{BC}(t)$). To correct the error introduced from the glue shrinkage, different choices of controllers are possible but, in the current work, proportional controller with a gain K is used to study the approach. Referring to the spring equivalence diagram of Fig. II.4, in order to control the distance, the Robot 1 can be moved under a direct control. For stiffness k_1, k_2 respectively for Beam 1, and Beam 2, the required actuation from robot 1 can be formulated as written in Eq. II.5 which is derived from Eq. II.6 and Eq. II.7.

$$\hat{d}_A(t) = K(1 + \frac{k_2}{k_1})d_d + \frac{k_2}{k_1}(d_{BC}(t_u) - (K+1)\hat{d}_{BC}(t)) \tag{II.5}$$

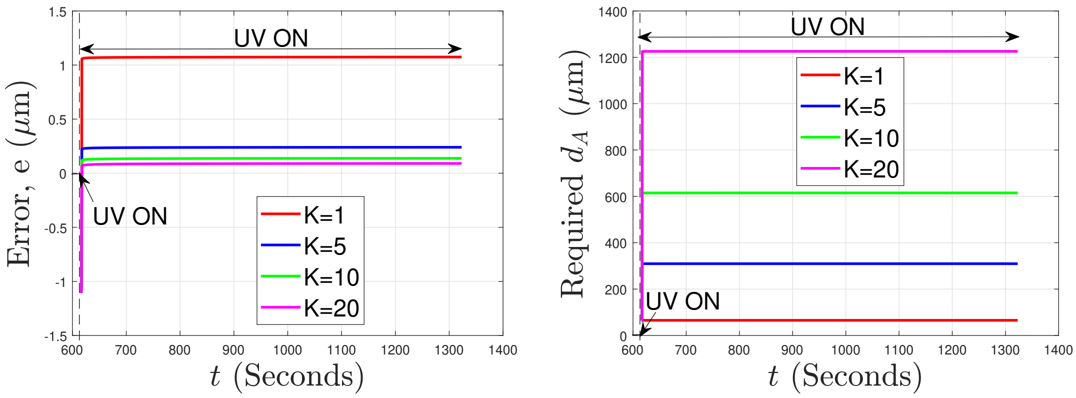

(a) Tracking error with controller gain (b) Required actuation with controller gain

Figure II.12 – The dependency of the controller gain on the extent of actuation and accuracy

$$d_A(t) = \frac{k_2}{k_1} d_C(t) + d_B(t) \tag{II.6}$$

$$\hat{d}_{BC}(t) = d_{BC}(t_u) + d_B(t) - d_C(t) \tag{II.7}$$

The correction strategy used for formulation of Eq II.5 was based on correction of point B position to have $d_{BC} = d_d$. But the correction extent is limited by the dynamic of correction as the correction can only be done when the glue is not cured, this argument is included in the modeling part. Therefore the controller speed can allow to reach the accuracy needed.

For different values of controller gain K, the estimation error and the required actuation are shown in Fig. II.12. It can be seen that the fast correction can facilitate to reach desired accuracy. Also as the glue curing phenomenon is very rapid, therefore the correction dynamic appears as step from the model based actuation. The made correction includes two components, first the actuation requirement for actuation in general, second the growing stress from the curing, therefore a high actuation is required to reach better accuracy. Indeed the experimental context can bring up additional challenges to reach the desired performance. Therefore a further experimental analysis and the use of active control for a precise assembly is discussed in the next chapter.

II.6 TOWARDS AN ACTIVE CONTROL FOR PRECISE GLUING

As discussed in previous sections, the glue shrinkage and its dependency on the external load. In this part of the chapter, the experimental work dealing with the control for precise gluing is presented. The control scheme as defined from the model in section II.5, brings many information which is needed to consider for the controller design for a precise gluing.

II.6.1 Working principle

This part of work aims to address the problem of positioning accuracy resulting from glue curing and to introduce a versatile solution to meet positioning requirements. In the present work, gluing about the Z-axis (Fig. II.7a) is addressed using the presented beam-based system. There are many parameters that can influence the assembly behavior, including glue quantity, relative contact area, and beam stiffness. The influence of the positional drift from glue curing about other planar (X and Y) axes can be considered negligible relative to the Z-axis, which was the case in [Dai 19]. This can be seen in context of gluing plane which is XY (contact with glue) in the presented configuration, so the orthogonal Z axis would include the dominant shrinkage tensor, therefore the possibility of sliding in XY plane is negligible. The other problem is from a very intense UV exposure that might introduce small voids around the neutral axis of the beams [Norland 00]. This is mainly possible when using very fast curing of glue, so that neither the glue nor the beam surfaces can equilibrate rapid enough to restrict the stress development.

In the literature, there are several works reporting the use of “depth curing” in place of “surface curing” using photoinitiators [Okamura 16]. With the suitable concentration and choice of photoinitiator, it could be possible to avoid the creation of void by facilitating the stress release. In the current work, the UV exposure intensity was minimized by placing the source suitably far (based on experimental observation) from the glue, thereby resulting in a slow curing rate, and the possibility of void creation could be minimized because of sufficient time for stress release. The other justification for negligible void creation can be explained by the length to width ratio of the employed beams, which is more than 20 times for all chosen beams. So, overall, the major effect is considered to be along the longitudinal Z-axis. The idea is to demonstrate the validity of the proposed approach about the chosen axis, which can then be extended to another axis (with the inclusion of an additional sensing mechanism).

The top beam can be, for instance, a microgripper holding a micro-object (part in contact with the glue) and the bottom beam as a substrate. Basically, the presented configuration and the opted approach was chosen in the context of a tethered configuration for micro-assembly. The objective will be to control the relative distance [i.e., the distance between the two beams tips (denoted as points B and C of Fig. II.7a)].

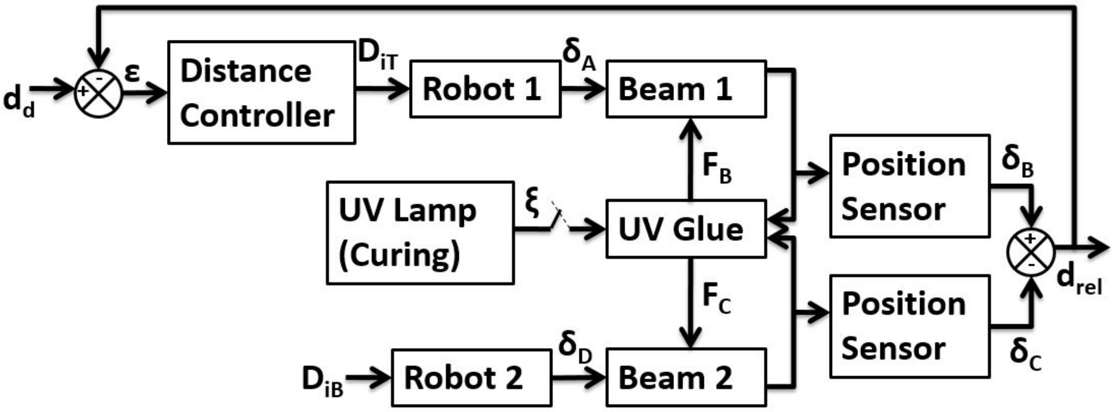

Figure II.13 – Proposed scheme for distance control between the Beams

$$\begin{cases} F_A = k_{b1} \times \ (\delta_A - \delta_B) \\ F_B = k_g \times \ (\delta_B - \delta_C) \\ F_D = k_{b2} \times \ (\delta_C - \delta_D) \end{cases} \tag{II.8}$$

In the presented model of Fig. II.7a, the displacement of points A, B, C, and D (along the Z-axis) are δ_A, δ_B, δ_C and δ_D respectively. Beam 1 stiffness is termed as k_{b1} and Beam 2 stiffness as k_{b2}, whereas the glue stiffness is termed as k_g. F_A, F_B, F_C and F_D, which are the forces acting at point A, B and C (Eq. II.8) respectively. F_B and F_C are expected to be numerically equal and also under stabilized equilibrium; all forces should be equal because of the chain configuration.

II.6.2 Controller Design

The proposed active control strategy is shown in Fig. II.13. There are two robots, Robot 1 and Robot 2, which are connected to Beam 1 and Beam 2, respectively, but only Robot 1 was used for the control of distance. Robot 2 has been placed at fixed position D_{iB} with constant input to the Robot for entire experimentation, and is therefore not directly included in feedback control. The respective beams position (when in contact with glue) would also be influenced by the presence of UV light (turning on the UV lamp); this additional influence has been denoted as ξ. All of the measured positions shown in the control scheme (Fig. II.13) are in common frame. The actual relative distance between the beams (d_{rel}) must be compared with the desired distance between the beams (d_d) to generate the error signal ε, which is further processed by a proportional "Distance Controller" with gain (K). The output D_{iT} from the controller was input to Robot 1, thereby achieving the necessary changes in its position. With the internal sensor of the robot, the current position and the desired change were compared to make the necessary updates.

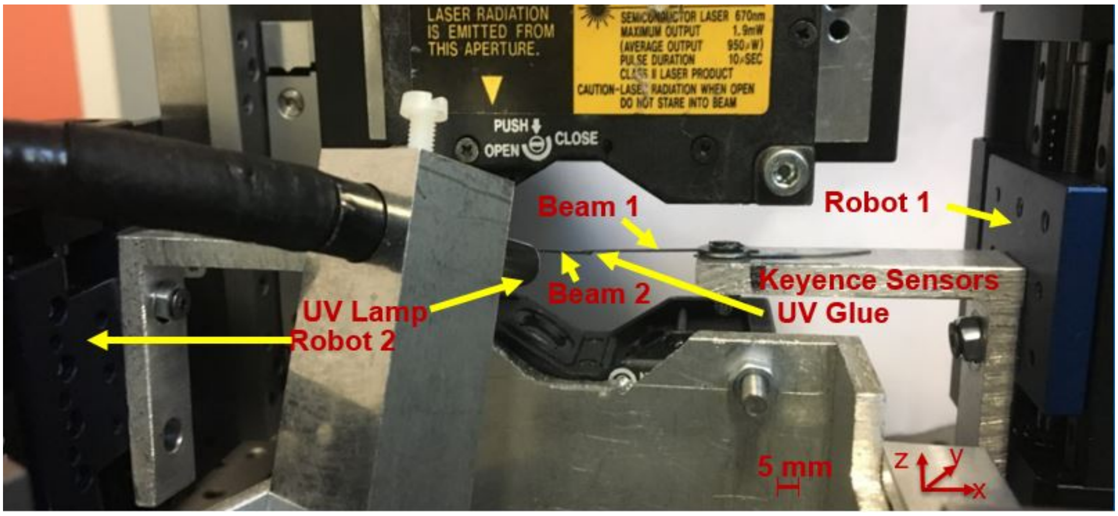

Figure II.14 – Experimental Setup used for the analysis

II.6.3 Experimental setup

There are two main requirements from the experimental side. First, to be able to analyze the glue curing behavior, as discussed in section II.6.1. Second, to be able to perform the defined active control action explained in section II.6.2.

The experimental setup based on the proposed beam model (Fig. II.7a) is shown in Fig. III.8. There are two Keyence (LC-2420) position sensors used which has sensing resolution of 10 nm.

Throughout the different experiments, there are three kinds of beams used, all made of steel material with the stiffness of 10, 20, and 167.5 N/m to investigate different potential behaviors that may happen during a gluing task. The targeted area (the shared area between beams) for gluing throughout the different experiments was 1×1 mm. The chosen UV glue for the experimentation was VITRALIT 6128, whereas the UV light source utilized for glue curing was DYMAX Blue Wave 50 with UV emission of 365 nm wavelength. As shown in the experimental setup, the two beams are attached to Robots, these are basically M-122-2DD motors from “Physik Instrumente (PI)”, and the used controllers for these motors were C-863 from Mercury. Along with these key elements of the presented experimental setup, there were manual stages, which were used for the pre-positioning of different elements.

II.6.4 Behavior in the absence of the proposed control scheme

In this section, several experimental results are investigated to analyze the challenges in the absence of the proposed control scheme. Because of the use of thick film, capillary action should also have an influence on the positioning.

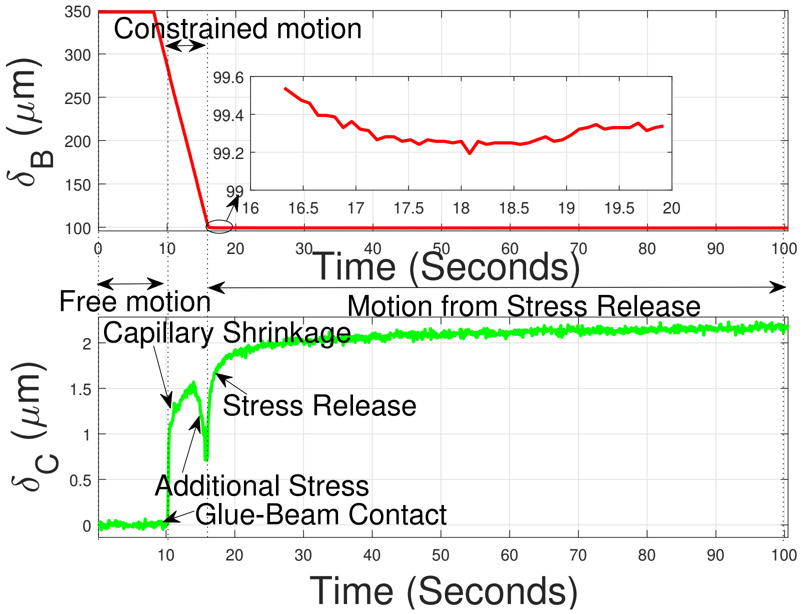

(a) Effect from Glue-Beam Interaction

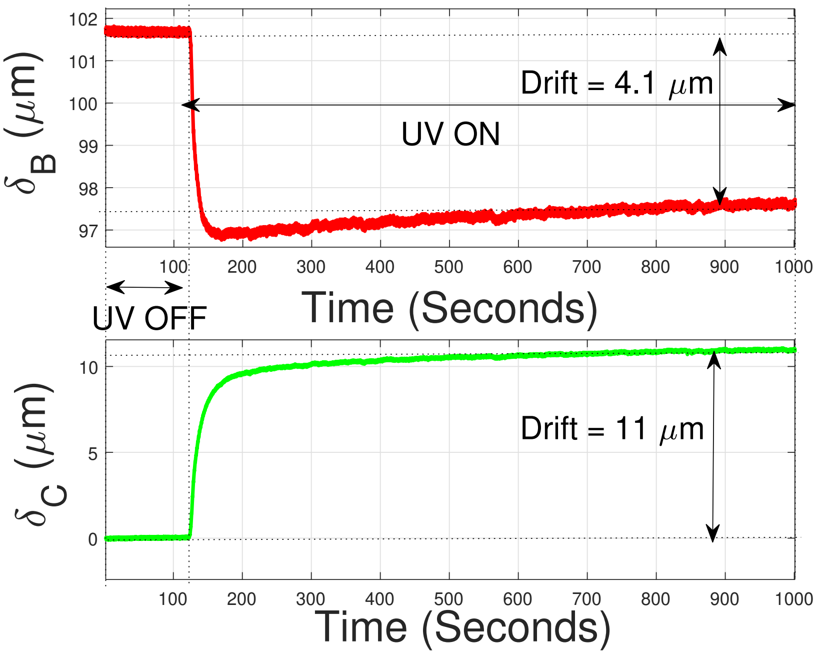

(b) Effect from curing

Figure II.15 – Behavior in absence of control from interaction and curing

Table II.3 – Obtained shrinkage from different experiments

k_{b1} (N/m)	k_{b2} (N/m)	G_i (μm)	G_f (μm)	Distance Drift (μm)
167.5	10	99.2	88.9	10.3
167.5	10	93.25	78.9	14.35
167.5	20	88	76.6	11.4
167.5	20	68.8	63.1	5.7
167.5	167.5	101.6	86.5	15.1
167.5	167.5	98.5	86.5	12

To monitor the behavior during glue contact, Beam 1 and Beam 2 of 167.5 N/m was used. In Fig. II.15a, the initial glue droplet size is approximately 300 μm (in diameter), and Beam 1 is targeted to be placed 100 μm away from Beam 2. For approximately first 10 s, Beam 1 was in free motion and then it came in contact with glue. With glue-beam contact, Beam 1 followed a constrained motion from time 10 to 16 s. During the constrained motion, a capillary based shrinkage can be seen, which means the stress resulted from Beam 1 movement was not stronger than the capillary stress and so this resulted into Beam 2 bending towards Beam 1. But there is a time when the stress from Beam 1 pressing became significantly higher than the capillary stress (marked zone as “Additional Stress” in Fig. II.15a), this would result into Beam 2 motion along the same direction as that of Beam 1. The developed stress starts to release as soon the introduced pressing from Beam 1 is stopped. The quantity of glue and extent of stress developed would influence the final positioning of the end of the beam. Therefore, there is considerable drift possible induced by the capillary action during the beam placement against the glue. There are multiple factors working together at the liquid phase of the glue, adding up multiple possible uncertainties for final positioning of the beams. This positional drift may be minimized by suitable placement of the Beam 1 against the glue, but the major influence is from the positional drift induced during glue curing.

To start with glue curing, a wait of a certain duration was made to allow the stabilization of both beams against the liquid glue. This stabilization was considered when the drift minimized to the order of sensing resolution. In Fig. II.15b, Beam 1 (of stiffness 167.5 N/m) is used against Beam 2 (of 167.5 N/m stiffness). Beam positions are at a constant level before the start of UV light, with an initial distance of 101.6 μm. As a result of turning on the UV light, the two beams deform towards each other, with drifts of 4.1 μm and 11 μm from Beam 1 and Beam 2, respectively. A slow drift after the first quick drift (just after UV ON) is mainly because of the stress release derived from initial press/bending of the beams.

As the primary interest is to maintain the desired distance between the beams, the drift induced by glue curing is addressed through shrinkage of the distance (between the beams). There were several experiments performed (listed in Table II.3) to examine the shrinkage order between the beams. The distances between the beams before the start of glue curing are listed as “G_i” in Table II.3, whereas the distance as a result of glue curing is listed as “G_f”. Therefore, the shown “Distance Drift” (Difference of G_i and G_f) in the table is mainly from the glue curing, whereas we do have the shrinkage from the capillary action dependent on introduced stress and glue quantity (as seen in Fig. II.15a). The big difference in distance drifts from 11.4 to 5.7 μm in two runs with 20 N/m for Beam 2 is mainly because of the different glue quantities between the beams. The amount of drift is directly dependent on the quantity of glue. The experimental results are shown in Table II.3, which differ mainly because glue quantity was not controlled in different parallel runs. This also demonstrates the behavior sensitivity over different parameters. The shrinkage from capillary action (before the start of curing) ranged between 2 and 17 μm, throughout the different experiments listed in the Table II.3. Therefore, the overall shrinkage from the gluing process could reach up to 30 μm, which is a serious concerned from an assembly accuracy point of view. Therefore, the key objective of this work is to have a versatile approach for micro-assembly using UV glue, which could result in a repeatable sub-micrometer accuracy positioning.

II.6.5 Behavior with proposed control strategy

The chosen control scheme (Fig. II.13) with a single robot allows the flexibility for micro-assembly operations, especially where the substrate is not robotized. The intention in the proposed work is to adapt a versatile approach that can also work for a thick film (complex compared to thin films), and to avoid any special treatment for gluing. Glue thickness > 50 μm is targeted to demonstrate the feasibility of the approach, but the approach aims at being independent of the choice of glue thickness. The limits in terms of glue quantity and the area to be glued can be defined from sensing and opted systems limitation. In the presented case, Keyence sensors are used, for which, a relatively high stiffness beam (chosen 167.5 N/m) as compared to 10 or 20 N/m is used, so that the corresponding displacements are scaled down. As with stiffer beam, a higher force can be generated at the assembly end with small movement of the beam whereas in case of low stiffness beam (10 or 20 N/m), it may requires to move out of the Keyence sensing range dependent on chosen glue size and area to be glued. Moreover, the chosen stiffness is closed to the stiffness of instrumented gripper (130 N/m) used in [Komati 14a], therefore a comparative analysis in terms of limitation to tasks handling could also be done.

The main principle of the control strategy employed is to move Robot 1 with sufficient force at the assembly end (beams end) so that the desired distance between the beams can be obtained. The passive beam’s position is an important information which is required for processing of the control action. This position would be influenced depending on the beams’ interaction with glue and the movement from Robot 1. Therefore, the entire experiment has been divided into five steps. Step 5 includes the proposed active control strategy, whereas the other steps are used to track the positional changes during the different steps of the gluing process.

II.6.5.a Calculation of the bottom beam's relative position

The chosen Keyence sensor for position sensing has a typical sensing range of 400 μm, and therefore the targeted starting distance was chosen to be in this range. Also, based on the direction of movement of beams, the respective Keyence sensors were positioned close to the extreme sensing value. For an efficient implementation of control strategy, there is a requirement for the calculation of all positions in a common frame. Therefore, the Beam 2 position (point C) was chosen as the world frame for all experimentation. The Beam 2 position, taken as the origin, is symbolically termed as Z_0. An experimental model to show the interactions between the beams is shown in Fig. II.16a. A trapezoidal signal (amplitude, 300 μm) was given to the Robot 1 (Fig. II.16b) to allow Beam 1 movement towards Beam 2. And based on the movement of Beam 2 under the interaction with Beam 1, the Beam 2 position can be calculated. This leads to the identification of position Z_0 relative to Robot 1 movement.

II.6.5.b Glue Deposition

It is possible that, because of gluing or placement tool interaction, the substrate (Beam 2) moved to another stable position (lack of elasticity). Therefore, to be sure about the happenings throughout the phase of the glue placement, the position of Beam 2 was monitored. To have sufficient space for glue placement at Beam 2, Robot 1 was moved to a waiting position Z_W, and the Beam 2 position was accordingly monitored. In Fig. II.16d, Z_W was 4 mm, and an impulsive displacement can be seen as a result of interaction between the Beam 2 and gluing tool.

II.6.5.c Contact of Beam 1 with Glue and stabilization

Now, there is a requirement of placing the Beam 1 in contact with glue (Step 3), but at the same time, there could be a considerable spreading of glue (Fig. II.16e). Based on the identified Z_0 from Step 1, and the targeted distance between the beams (d_d), which is 50 μm, Robot 1 was sent to a position $Z_0 + d_d$. Dependent on the viscosity, quantity of glue, stiffness of the beams, and applied pressure around the beams, the actual distance between the beams is different than the targeted 50 μm, as shown in Fig. II.16f. The beginning of Step 3 has δ_B at a constant level in the absence of glue contact with Beam 1; then, as a result of its contact and further movement with glue, Beam 2 is compressed by 4.5 μm. Once Beam 1 is allowed to stay at the same level after completing the initial movement (Step 3), Beam 2 moved towards Beam 1, which was a result of capillary action together with the

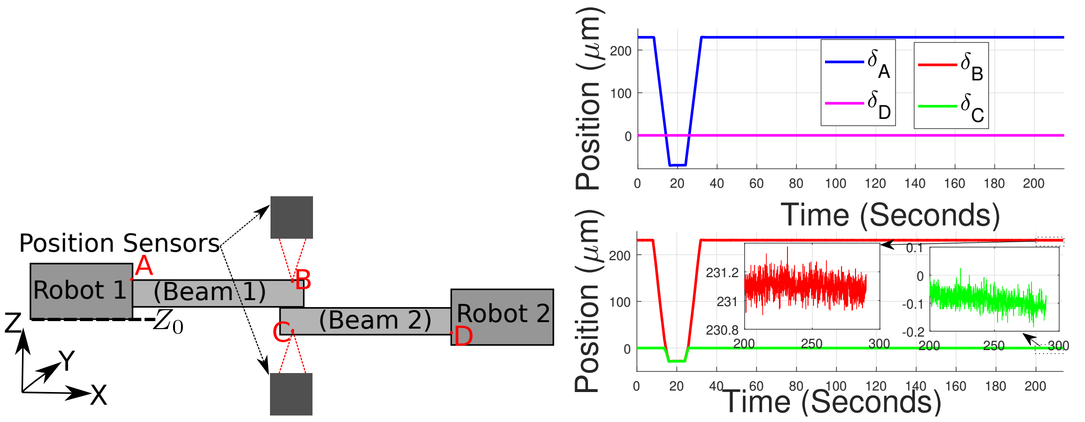

(a) Z_0 identification (Step 1)
(b) Relative position with input motion

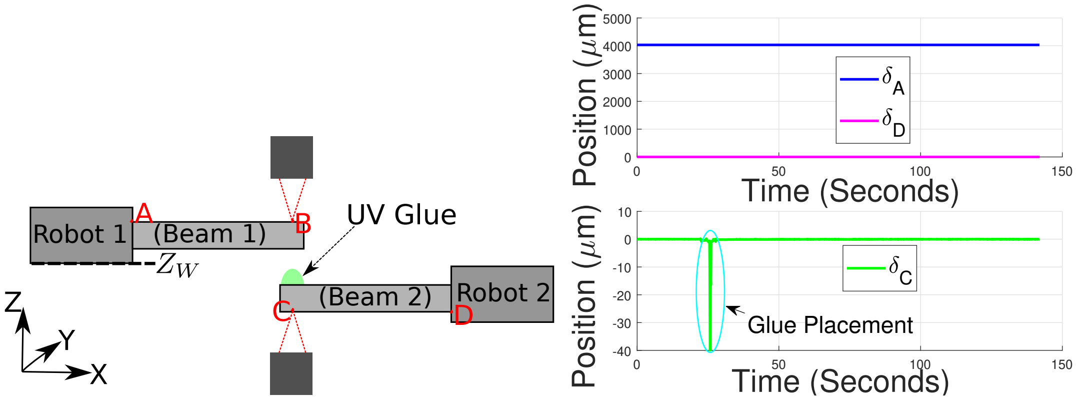

(c) Glue Placement on Beam 2 (Step 2)
(d) Behavior during glue placement

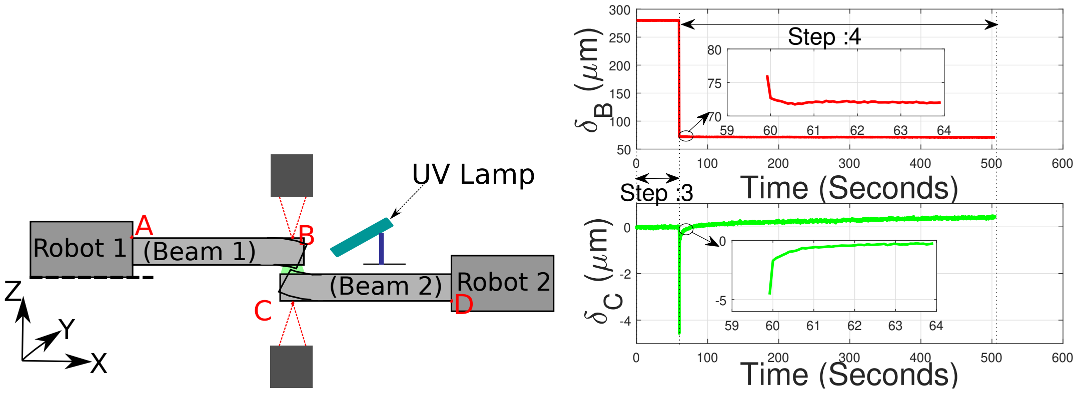

(e) Beam 1 contact with the Glue
(f) Beams-Glue contact (Steps 3 and 4)

Figure II.16 – Different Steps before use of control release of the introduced stress. The respective beams movements were monitored until acceptable stability (of the order of sensing resolution) was obtained (Step 4).

II.6.5.d Glue Curing and Distance Control

From Fig. II.16b, it can be seen in the zoomed-in part that even in the absence of any movement from the robot, and glue/beam interaction, there is the presence of oscillation which is, in fact, the noise from different sources of mechanical vibrations around. This signifies the limitation of the system in terms of noise influence, so with the use of distance controller, the error signal (ε) falling in the range of noise amplitude may not be trusted. Therefore, the correction against the order of noise can be ignored. This could provide two main benefits. First, the controller would be stabilized when there is no need for correction. Second, because of the controller stabilization, the cured link between the two beams will achieve relatively good strength compared to that against continuous correction from the controller. Also, Robot 1 and Robot 2 have the minimum step movements of 0.2 μm. Therefore, taking into consideration the system limitations and noise influence, a dead zone of $\pm$ 0.15 μm is included with the distance controller. So, if the error signal (ε), as shown in Fig. II.13, is inside the defined dead zone range, then there will be no correction in position D_{iT} of the Robot 1.

Before glue curing starts, it is important to ensure an initial condition, such as the stable positioning of the beams in the absence of UV, and then UV light can be turned ON to start the gluing task (Step 5). For the processing of the experiment, the Baud rate of 38400 was used for communication to Robots using mercury C-863 controller (based on PID). To achieve suitable speed and avoid overshoots (sensing range limitation), the “Distance Controller” (Fig.II.13) chosen was a proportional controller with unity gain. For the exchange of signals, a NI USB-6353 card was used. The obtained sampling frequency for different processed signals was 12.5 Hz. As the included Keyence sensors are external to the glue-beam system and, therefore, the position of the sensor was positioned well to be within convenient sensing range for the entire assembly operation.

The multiple sources of uncertainty seen in section II.6.4 coming from capillary effect (liquid glue) and glue curing are collectively seen as a single perturbation to the system. The proposed control scheme has to reject this perturbation for the desired behavior. In Fig. II.17a, Beam 1 moved by 300 μm to generate sufficient force between the beams to have the desired distance (d_d) of 50 μm. From Eq. II.8, with the beam stiffness of 167.5 N/m, the order of force required to achieve the desired distance is 50 mN. The key requirement is the sufficient force at the assembly end, and this requirement was fulfilled by the automated movement of Beam 1 as a result of the proposed control scheme. From Fig. II.17a, it can also be seen that the major distance correction against the curing was made in the first 60 s after turning on the UV light. Therefore, the proposed control action is fast enough to adapt the requirements against the curing. The obtained distance between the beams oscillates slightly near this defined dead zone value. Fig. II.17b highlights

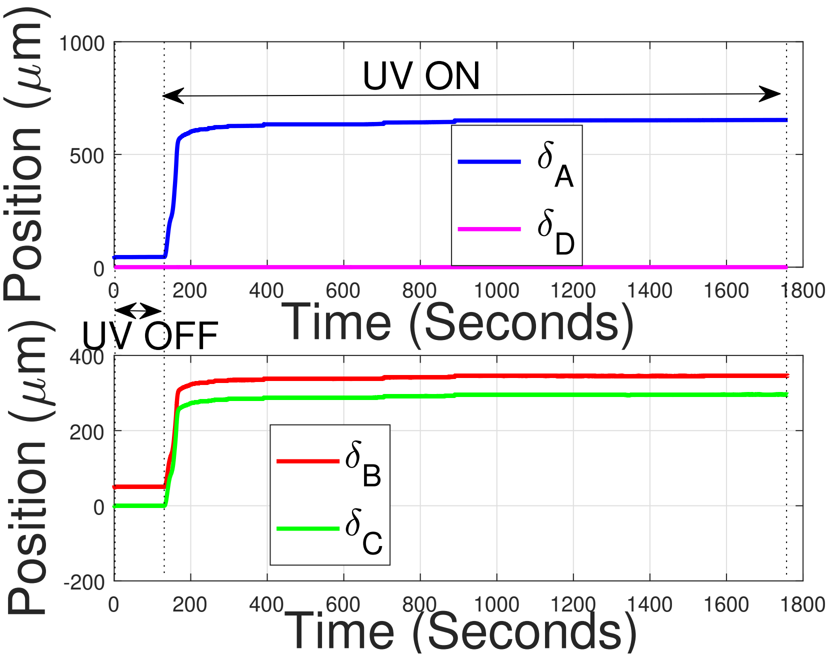

(a) Actuation with control (Step 5)

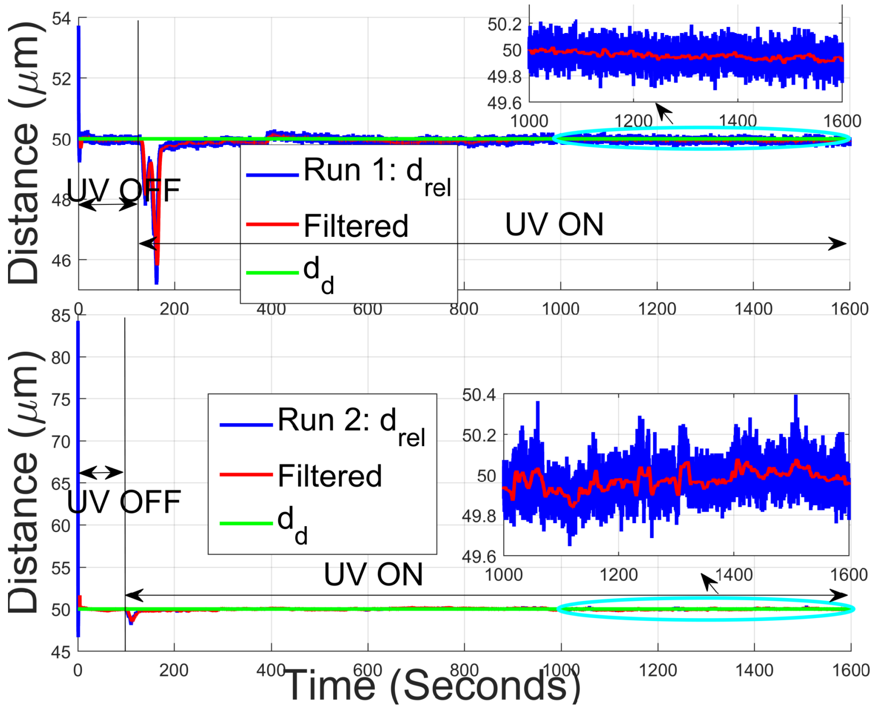

(b) Obtained results from 2 Runs

Figure II.17 – Actuation and obtained gluing with the proposed active control the distance evolution over time during this gluing process. There were several experiments done to test the repeatability of the approach, and the experimental result from the two runs (Run 1 and Run 2) is shown in Fig. II.17b. Run 1 corresponds to Fig. II.17a, whereas Run 2 corresponds to another experimental result. Before switching on the UV light (in Run 1 of Fig. II.17b), the initial distance between the beams was controlled from 53.9 to 50 μm. The proposed control action can maintain the desired distance with an error in the order of 200 nm. By saying order 200 nm means, the obtained distance signal (d_{rel}) oscillates (with the exclusion of spikes) by 200 nm around the targeted distance. But it can be seen that with the use of a moving average filter, the filtered signal is very close to the desired 50 μm (typically less than 20 nm positioning error). There are likely multiple sources of this noise; the main sources could be the mechanical vibration resulting from the electrical devices around, the different vibrations from the movement around, and also the optical presence might have a contribution to the obtained noise. In Run 2, the initial distance between the beams was 84.6 μm, but with the proposed approach, the final distance between the beams is of the same order as that of Run 1, indicating the repeatability of the behavior. From Fig. II.17a, there is no movement of Robot 1 after $\sim$ 900 s, which means that the difference in desired and the actual distance between the beams is well inside the defined dead zone. Therefore, the noted dynamics after stopping the movement of Robot 1, as shown in the zoomed-in version of Fig. II.17b, mainly comes from the noise. Achieving accuracy around the opted dead zone and the resolution of the sensor also indicates that, if the chosen systems limitation can be removed or minimized, then it could be possible to further improve the accuracy with the same approach for the distance control.

II.7 Conclusions

The chapter constitutes the behavior analysis of glue for its use in the context of micro-assembly. The behavior of glue in absence and presence of external load was analyzed, which helped to build a modeling scheme with which the shrinkage-external load dependency can be further investigated. The modeling scheme helped further to investigate the scenario desired from the external load in order to have a desired distance between the two gluing surfaces. Based on the observations, an active control scheme is presented which demonstrated the feasibility of the approach in order to have a desired positioning. The obtained performance from the used approach is not dependent on several potential parameters discussed, which proven the versatility of the strategy used for a precise gluing. The approach used an indirect control of force by means of position control, which signifies the interest of position control using the force information.

The influence of unsymmetrical bending of the beams (around the neutral axis) was also minimized by slowing the curing process. There is need of multi-DoF fast and precise gluing. It was also seen that glue quantity and shape affect the behavior of the shrinkage. Moreover, dependency over external sensor also requires frames re-positioning (the sensing frame and the beams frame) in order to be in the sensing range. This adds up additional complexity in the systems positioning. The instrumentation of the gluing platform along multi-axis (in the current case it was Beam 2) with precise and long range sensing capability can definitely strengthen to handle such tasks. Moreover, an instrumented gripper with a multi-axis sensing capability will bolster the manipulation and decision making capability before and during the process of gluing. Both these requirements are addressed in the coming chapters.

Chapter III

A high range-to-resolution multi-axis µForce/torque Sensing Platform

III.1 Introduction

Micro-devices are often used for instrumentation in order to retrieve useful local state information. Such devices present high interests in robotics or mechanical engineering as they enable to measure critical information in order to succeed in doing the desired tasks in an appropriate way (like gripping, guiding as in [Komati 16a]). Instrumentation bringing the capability to measure at very local states with the required resolution (typically few μN) is of strategic interest (as discussed in Chapter I). A sensor capable of precise sensing over high range can allow to sense in the uneven terrain during the task handling, where required sensing range may constitutes high degree of uncertainty. Therefore high range to resolution ratio (RtR2) can bolster the tasks handling capability of the system. Moreover, most of the commercially available μForce sensors are single axis and are designed to operate against a relative environmental frame. A small misalignment of target relative to the sensing axis may lead to the inaccurate measurement which may be significant at any specific phase of the task. Small scale devices often have coupling behavior with different mechanical axes. Therefore, it is important to have a multi-axis force sensor which can decouple the different-axis force components. From a sensing system design point of view, the different sensors need to be optimally used depending on the available workspace. A multi-axis sensor may come handy as compared to differently oriented single axis sensors. Moreover, one of the major requirement of the force sensing is in sensor's development itself (calibration of the force sensor). For the development of a multi-axis force sensor, a calibrated multi-axis force sensor may ease the characterization process. Therefore, it is a potential need to have a multi axis force/torque sensor with a high RtR2 capability.

Several multi-axis force sensors have been developed, depending on the requirements of the targeted tasks. A graphical comparison of the existing state-of-the-art multi-axis micro-force sensors (similar performance along the 2 axis) with the proposed work is proposed in Fig III.1. In all the cases presented in Fig III.1, the best possible sensing and range configurations are used (in case sensors have different performances under different modes of their proposed use). In [Adam 19] a vision based force sensor was presented, the best possible resolution out of different versions fabricated was 0.36 μN with the sensing range of 175 μN. Sensors developed in [Takahashi 14, Suzuki 19, He 14, Li 20b, Taghipour 20, Puangmali 12] works on optical based sensing, where sensor in [Takahashi 14] can sense force along 2 axes with ± 20 μN sensing range with a resolution of 1 μN which makes RtR2 ratio of 20. Similarly, the sensor in [Suzuki 19], can sense higher range up to 1 mN but with a resolution of 10 μN scaling the RtR2 ratio to 100. Whereas the optical sensor in [He 14] has possibility to sense axial force with 41 μN, with configuration that allow maximum range of 20 mN. In the same work the radial force can be sensed up to ± 20 mN but with resolution of 83 μN, making the RtR2 ratio vary between 240 to 408. Work of [Li 20b], allows to sense force up to 2N, which is significantly high compared to the other discussed works but the resolution demonstrated was

8.8 mN, inducing the RtR2 ratio of 227.2. The capacitive sensors are known for there high resolution, works included in [Yang 17, Beyeler 09, Muntwyler 10] are capacitive sensors. The capacitive sensor of [Yang 17], allows RtR2 ratio of approximately 170 with a resolution of 0.58 μN. A six axis MEMS force-torque sensor based on capacitive sensing with a sensing range of 1 mN and a resolution of 1.4 μN was demonstrated in [Beyeler 09]. The RtR2 ratio was approximately 714. There was another work followed by the same authors in [Muntwyler 10], which demonstrated a 3 axis force sensor with an adjustable force range from ± 20 μN to ± 200 μN, with validated sensing resolution of 0.1 μN along all the three axes, which makes the best RTR ratio 2000. In Fig III.1, very few sensors are able to measure force up to some mN range with a resolution of some μN. Therefore the RtR2 appears as a key lock. The proposed work targeted this lock, and comparison to existing state-of-the-art it brings RtR2 ratio of 55000. The sensing principle of the proposed sensor is based on vision.

Vision based sensing constitutes a great interest in multi-axis sensing, especially when the targeted sensing need to be precise against the environmental variation, such as change of temperature, humidity. Such sensing technique can take advantage of a dedicated encoding, so as to sense over a long range and to be able to decouple different axes. The encoding strategy defined in [André 20b] and [André 20a] demonstrate the possibility of a precise and multi-axis sensing capability using vision. In order to use these advantages of sensing over a long range there is requirement of a dedicated compliance structure design, such as in [Yong 09]. In an attempt to increase the sensing range using the compliance structures, it may possible that the structure exhibit the non-linearity after some part of the linear sensing. The different force sensors discussed in the state-of-the-art, operate in linear zone with a constant value of force to displacement ratio but majority of available mechanical structures have wider non-linear zone compared to linear zone (at the micro-scale). Working in linear zone provides many advantages, such as simplified model, higher linearity, and flexibility over segment of the sensing range without knowledge of the pre-load. Before getting into an approach to consider the non-linearity evolution in the sensing, it becomes important to analyze the non-linearity presence in some of the recently demonstrated works. In [André 20b], the obtained non-linearity for the employed encoding was between 0.4-1.15 % over a displacement range of 9 μm whereas the measurement error was 1.15 %. Moreover talking about the non-linearity of different force sensors operating well in the linear zone can also be analyzed. For example, in [Guggenheim 17] the demonstrated cross coupling sensing error was significant with non linearity 1 %. In [Liu 13], for the two configurations the demonstrated non-linearity was 1.57 % and 2.03 % respectively. Whereas in the work of [Xie 16], the demonstrated non-linearity was 1.82 %. Going for little higher operational range as compared to the discussed cases, in [Li 20c], the rms error for a triaxis force sensor was less than 3 % without consideration of temperature impact. In all these cases, the operational region of the force sensor was in the linear zone, but still the presence of the non-linear components was seen in the repeatability. Therefore the extension

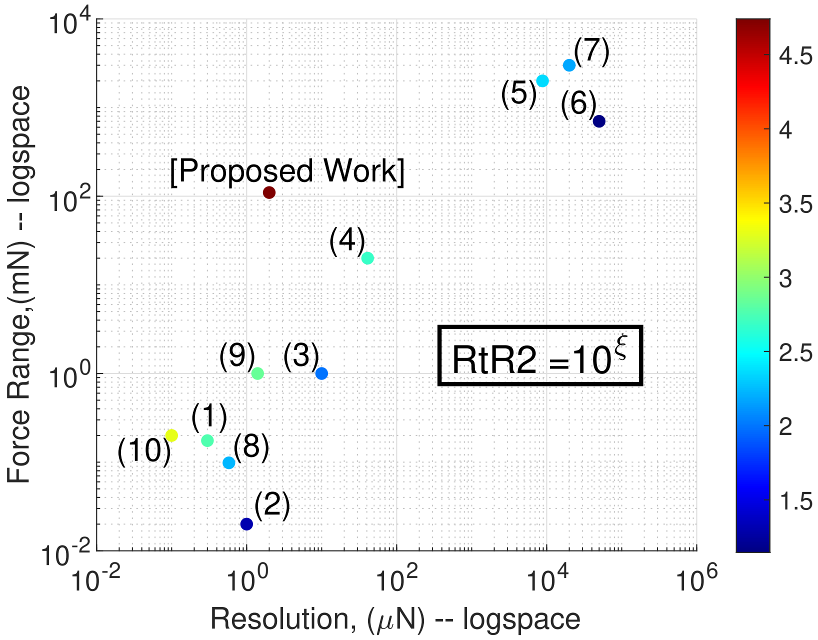

Figure III.1 – Comparison of different state-of-the-art Multi-axis Force Sensors

of the sensing range in non-linear zone can be made provided the corresponding performance remains within or close to the performance of working in linear zone alone.

Finding a way to make use of non-linear zone adds up a diverse capability to use the mechanical sensing structure over a very high sensing range. For example, in [Dosta 17] a rubber like structure which undergo large deformations covering linear and non-linear zone is modeled with the approach of Bonded Particle Model (BPM). But instead of material based information, the requirement in the current sensing platform case is to use the planar positions information from vision. Overall, the objective and so the key content of this chapter can be formulated as:

- To design a system capable of translation and rotation over a long range (corresponding to force of 100 mN or higher as discussed in chapter I) and fulfilling both the encoding and mechanical requirements.
- To fabricate the corresponding structure.
- To develop a model which allows the use of the sensed planar positions to Force and Torque capable to adapt the force-displacement linear or non-linear relation if required.
- To demonstrate a high RtR2 performance experimentally.

To combine the targeted works, this chapter will firstly introduce the sensor design including its working principle (section III.2), system modeling (section III.3), explanation of experimental setup with experimental results validation (section III.5), and followed by conclusions (section III.7).

Works	Reference
(1)	[Adam 19]
(2)	[Takahashi 14]
(3)	[Suzuki 19]
(4)	[He 14]
(5)	[Li 20b]
(6)	[Taghipour 20]
(7)	[Puangmali 12]
(8)	[Yang 17]
(9)	[Beyeler 09]
(10)	[Muntwyler 10]

Table III.1 – State of the art References for Fig III.1

III.2 SENSING PRINCIPLE AND PLATFORM DESIGN

III.2.1 Sensing Principle

Force sensing is always indirect and requires physical laws and/or a model. Among the different physical principles that can be used to assess force, many limitations occur and getting a high RtR2 is really a challenge. The use of a compliant platform is a common solution and, then, force can be retrieved through the measurement of either strain, stress, displacement, etc (discussed in section I.4 of chapter I). Use of structure like piezoelectric, piezoresistive, etc. are capable of a precise sensing but the dependency over the active state changes like stored electric charges, resistance etc. are mainly limited over a short range (requires a dedicated geometrical and electro-mechanical study for the system design). A passive structure has wider flexibility over design choice in terms of its mechanical side alone (less constrained over the system design). Therefore the exterior sensing methods, such as optics or vision can be used to take advantage of a flexible passive structure. A microscopic motion can be monitored precisely by vision, but the interest at the micro-scale is to avoid motion of the camera which usually are bulkier. The force sensing principle used in this chapter consists in applying the in-plane measurement method to a compliant platform of which the motion of the central part is representative of the force applied. For this purpose, a pseudoperiodic encoded pattern is encrypted on the movable part of a compliant structure and observed by a static vision system fasten to the external structure frame (no motion of camera). The design of a suitable compliant structure is thus required with the constraint, so that the encoded pattern must remain in the in-focus plane of the vision system.

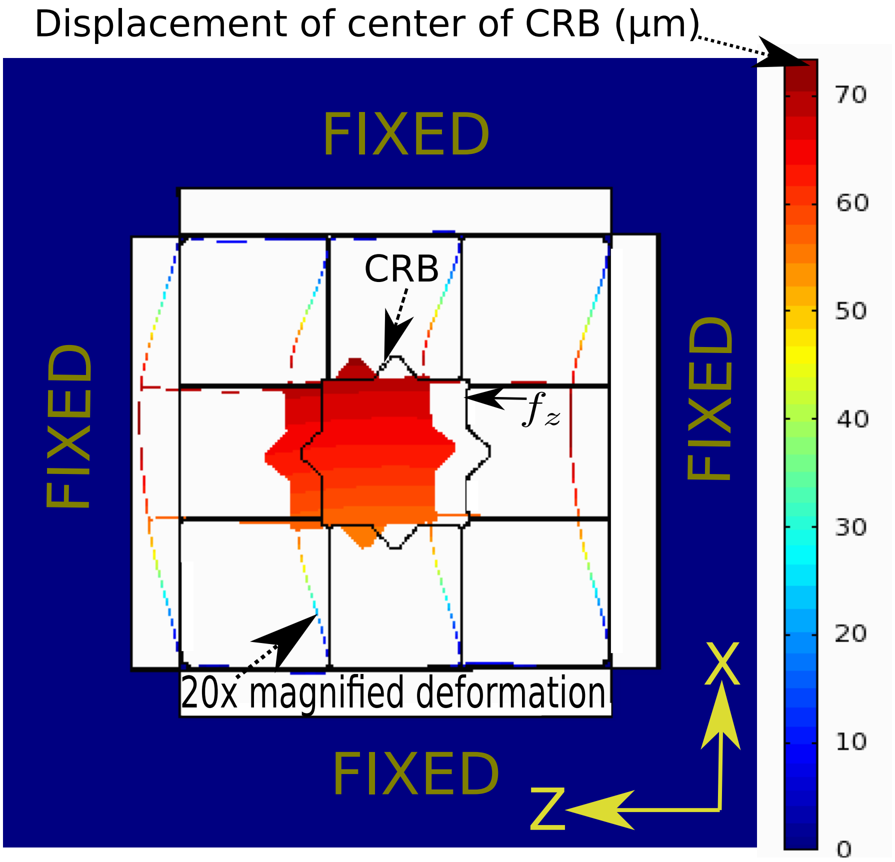

Figure III.2 – Sensing platform design and working principle

III.2.2 System Design

System design needs to fulfill a high precision requirement tied to the encoding of the platform and a sufficient mechanical flexibility to allow large range sensing. Because of the visual measurement approach chosen, the movable part must be rigid to avoid encoded pattern deformations that would result into corrupt measurements. Therefore, the mechanical structure must exhibit a movable but rigid part bound to the static frame of the structure by means of flexible links. The design should keep the advantage of symmetry and elastic behavior over a large range (to allow the best possible performances along the 2 axis). The device was fabricated through clean room processing because of precise encoding requirements (cf. Sect.III.2.3) and because of the highly sensitive compliant structure with beam widths of a few μm. The overall size of the proposed system is 29.5 mm × 29.5 mm, with the Central Rigid Body (CRB) of 5.2 mm × 5.2 mm, beams around with width of 50 μm and thickness of 500 μm. The fabrication process is discussed in section III.4.

Fig. III.2 presents the planar structure designed. The encoded pattern need to be deposited on the CRB whereas the symmetry of the surrounding flexible beams are expected to allow both large range and easy axis decoupling. The form factor of the beams ensures guided planar motion fulfilling focus requirements

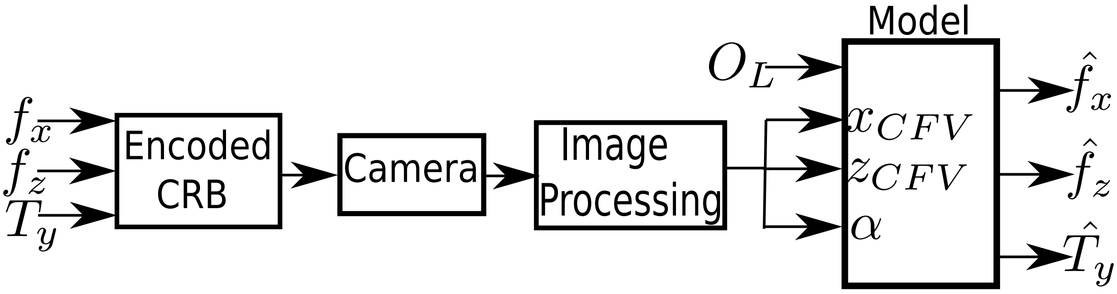

Figure III.3 – Principle scheme of the force-torque sensing platform

(dimensions like beam width, length, thickness were accordingly chosen). Fig III.2 is a COMSOL simulation view, where an external force f_z is applied, resulted into displacement of CRB, and according deformation of the beams around. This part is detailed in Sect. III.3. The principle scheme of the platform is depicted in Fig. III.3. Where f_x and f_z are respectively external forces along X and Z axis, and T_y is the torque about Y, O_L is the position of the point of application of load. Vision algorithms applied to the images of the encoded pattern recorded by the camera provide three position data x_{CFV}, z_{CFV}, and α. Data x_{CFV}, z_{CFV} determine the X, Z positions of the center of the field of view with respect to the whole encoded pattern whereas α, the angle between the pattern axes and the pixel frame axes, determines the angular position around axis Y. These data need to be used in a model so as to have an estimate of the forces ($\hat{f}_x$, $\hat{f}_z$ respectively along X and Z) and Torque ($\hat{T}_y$ along Y). Further information on position retrieval is provided in Sect.III.2.3 whereas Sect.III.3 presents the platform modeling.

III.2.3 Vision-based Position Measurement

The aim of visual processing is to retrieve data x_{CFV}, z_{CFV} and α which need to be converted into force / torque data. This step is based on an encoded pattern of the type described in [André 20b, André 20a] as well as suited decoding algorithms. Basically, the encoded pattern is made of a 2D periodic distribution of dots altered by missing lines and columns as shown in Fig.III.4. The periodic frame allows Fourier computations that result in the conversion of the pattern axes X and Z (position x and z respectively) into two linear phase maps ($\Phi_x(x)$ and $\Phi_z(z)$ respectively) defined by Eq. III.1.

$$\begin{cases} \Phi_x(x) = 2\pi \cdot x/\lambda_{phy} \\ \Phi_z(z) = 2\pi \cdot z/\lambda_{phy} \end{cases} \tag{III.1}$$

where λ_{phy} is the physical period of the pattern. The aim of the missing lines and columns is to unequivocally break the periodicity by means of a binary code (as define in encoded cell of Fig.III.4) and thus to allow the correct determination of every period index in both directions from any local view of the pattern. This is illustrated in Fig.III.4 where the minor field of view of Fig.III.4a is inserted in the

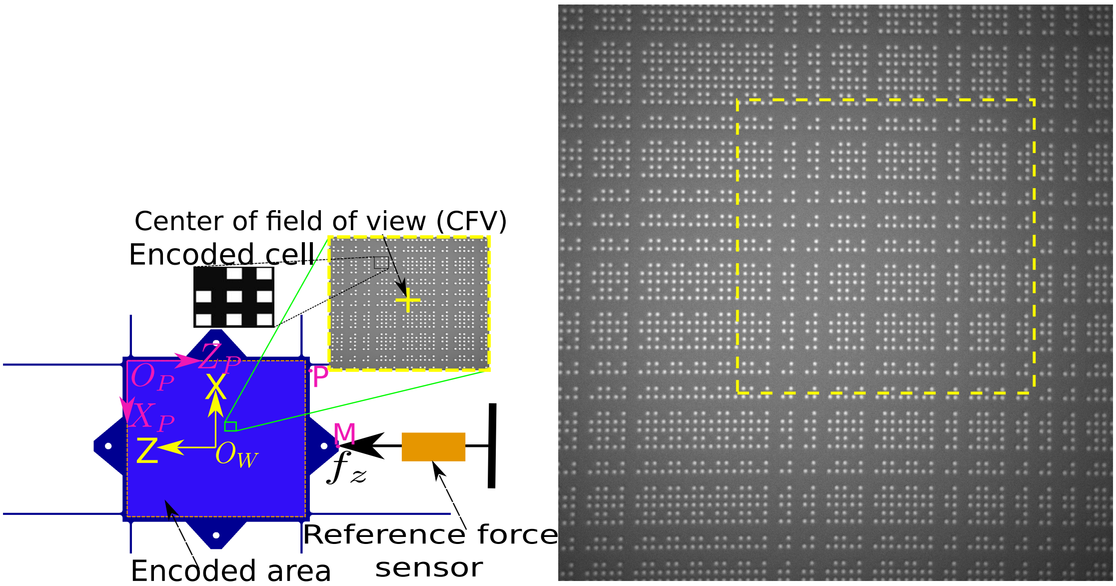

(a) Encoding on CRB (b) Major Field of View

Figure III.4 – Encoded Central Rigid Body (CRB) with different Field of View

major field of view of Fig.III.4b (yellow square). The resulting encoding of the platform can be seen as a 2D measuring scale where the missing lines and columns mark an entire number of periods whereas the dot distribution relative to the pixel frame allows a fine position interpolation by means of Fourier phase computations. In accordance and for each direction, position is retrieved for the Center of the Field of View (CFV) by involving two phase parameters as described below:

$$\begin{cases} x_{CFV} = \lambda_{phy}\frac{\phi_x}{2\pi} + k_x\lambda_{phy} \\ z_{CFV} = \lambda_{phy}\frac{\phi_z}{2\pi} + k_z\lambda_{phy} \end{cases} \tag{III.2}$$

where ϕ_x and ϕ_z results from the phase interpolation at the center of the field of view and k_x and k_z correspond to the correct number of entire periods.

The rotation α of the platform is given by the orientation of the lines and columns of dots relatively to the pixel frame of the camera. α is also retrieved with a high accuracy from the phase data. In Fig III.2, O_P is the pattern frame and O_W is the world frame. Information provided by the vision algorithm is obtained originally with respect to O_P frame but, to keep the uniformity, all positions are defined throughout with respect to world frame O_W. In practice, a physical period (λ_{phy}) of 6 μm with an encoding on 8 bits was chosen. The resulting encoded area of 4.716 mm × 4.716 mm is centered on the 5.2 mm ×5.2 mm area of the CRB.

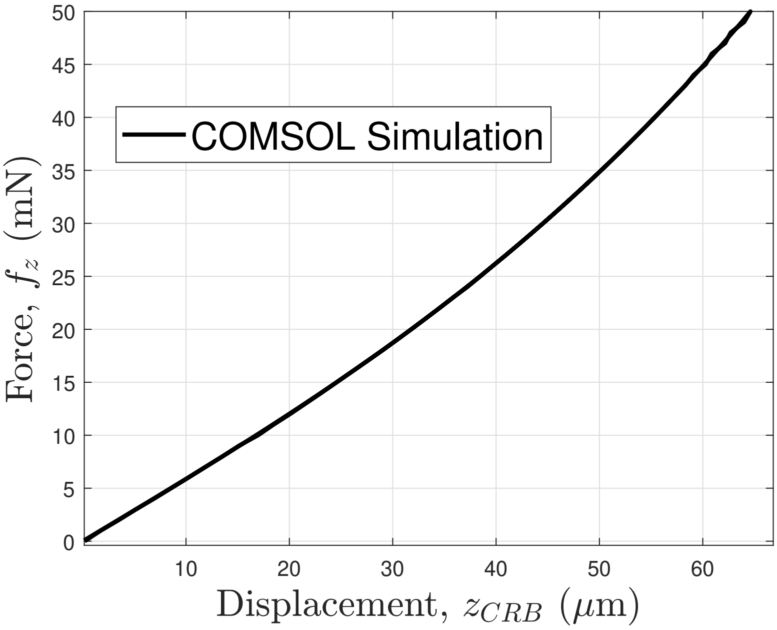

Figure III.5 – System Behavior from COMSOL Simulation

III.3 SYSTEM MODELING AND ESTIMATION

The conversion of position data of the CFV; x_{CFV}, z_{CFV} and α into relevant force and torque data requires a model of the mechanical behavior of the compliant structure. A behavioral examination of the designed platform was carried out by the means of COMSOL multiphysics simulation. Simulation was made under Quasi-Static condition with the use of Backward Differential Formula (solver order 5). Because of the deformable beams around the CRB (as shown in Fig. III.2), non-linearity in force-displacement relation is expected, especially when large deformation is targeted. To analyse the behavior, a ramp force of 50 mN was applied on the CRB, along the Z axis (marked as f_z in Fig. III.2). As a result of the force applied, the CRB undergone displacement, the colored intensity from blue to red is used in Fig III.2 to define the displacement magnitude of the entire test body. The deformation shown in Fig. III.2 is 20 × magnified of the actual displacement (which is shown in the colored bar), in order to have better visualization of the resulted motion. The displacement of the geometrical center of the CRB (z_{CRB}) was retrieved from COMSOL as depicted in the force-displacement curve of Fig. III.5 which shows non-linear evolution of stiffness. Any mechanical structure in general has a linear zone which may differ in size (operational region) based on the structural feature, and therefore it becomes important to have a force displacement relationship which could adapt a linear relationship for the linear zone and a non-linear relation afterward. Keeping the advantage of working in linear zone and capability to adapt the non-linear stiffness evolution over a long range a “Global Model" is presented which would basically work as a linear model for a defined linear range and non-linear in non-linear zone of deformation. Extrapolation of the calculated stiffness from the linear zone is termed as a linear model and the difference between linear and global model can then be analyzed.

The overall motion of the CFV results from a combined motion (translation and rotation). If the translations along the two axes are termed as d_x and d_z, along X and Z axes respectively then the overall motions along the two axes is given by Eq. III.3, where x_I, z_I are initial positions of the CFV along the respective axes and α is the rotation of the platform.

$$\begin{bmatrix} x_{CFV} \\ z_{CFV} \\ 1 \end{bmatrix} = \begin{bmatrix} \cos\alpha & -\sin\alpha & d_x \\ \sin\alpha & \cos\alpha & d_z \\ 0 & 0 & 1 \end{bmatrix} \begin{bmatrix} x_I \\ z_I \\ 1 \end{bmatrix} \tag{III.3}$$

As d_x and d_z, are pure translations, they directly depend on the forces f_x and f_z applied along these two axes. The additional displacement component (resulted from rotation) is referred to as P_I and is defined in Eq. III.5.

$$\begin{bmatrix} x_{CFV} \\ z_{CFV} \\ 1 \end{bmatrix} = \begin{bmatrix} a_1\cos\alpha & -a_1\sin\alpha & 0 \\ a_1\sin\alpha & a_1\cos\alpha & 0 \\ 0 & 0 & 1 \end{bmatrix} \begin{bmatrix} (\frac{f_x}{a_2})^{r_x} \\ (\frac{f_z}{a_2})^{r_z} \\ 1 \end{bmatrix} + P_I \tag{III.4}$$

$$P_I = \begin{bmatrix} \cos\alpha & -\sin\alpha & 0 \\ \sin\alpha & \cos\alpha & 0 \\ 0 & 0 & 1 \end{bmatrix} \begin{bmatrix} x_I \\ z_I \\ 1 \end{bmatrix} \tag{III.5}$$

The overall equation including forces f_x, f_z along the two axes and the initial position component P_I are shown in Eq. III.4. The variables r_x and r_z, are representative of the linear or non-linear force-deformation relation. For instance, these variables should be unity for a linear relation and non-unity for a non-linear behavior. Depending on the material properties of the deforming structure, the non-linearity component needs to be adjusted in order to reflect the changing non-linear stiffness. The variables r_x, and r_z can be defined using Eq. III.6, where def is x_{CFV} and z_{CFV} respectively for defining r as r_x and r_z.

$$r = a_3^{u(def)} \tag{III.6}$$

$$u(def) = \begin{cases} 0, & \text{if } 0 \leq def < d_1 \\ b_i, & \text{if } d_1 \leq def < d_{i+1} \end{cases} \tag{III.7}$$

Function u(def) is defined in Eq. III.7 which facilitate the decision making approach by splitting the sensing range into sub-regions. d_i defines the boundaries based on the displacements. In Eq. III.7, model is in linear region for def $< d_1$, otherwise the system is in non-linear zone. i is the number of sub-regions in non-linear zone, for $i = 1$, system has only 1 region (between d_1 and d_2) in non-linear zone. The force-displacement relation is defined linear for def $< d_1$, therefore the respective algebraic powers (r_x, and r_z) for X and Z axis respectively must be 1 in this region. When the system is in non-linear region then the r_x, and r_z should be non-unity. But, there need to be a parameter independent of the respective algebraic powers (r_x, and r_z), so that an adequate scaling of stiffness can be realized between linear and non-linear region. These parameters are respectively defined as a_1 and a_2. The parameter required to handle r_x and r_z throughout the operational range is a_3, which is raised to zero algebraic power for linear region and non-zero positive power for non-linear. Eq. III.7 defines the algebraic power of r_x and r_z, the respective intercept component in order to keep smooth computation is defined by Eq. III.8. If the non-linearity component is uniform, then only one value of b_i, and c_i with $i = 1$ is sufficient for a good force-displacement estimation. If not, the non-linear region may be divided into several sub-regions to include the changes of the non-linearity component throughout the sensing range.

$$v(def) = \begin{cases} 0, & \text{if } 0 \leq def < d_1 \\ c_i, & \text{if } d_1 \leq def < d_{i+1} \end{cases} \tag{III.8}$$

In the current case, the information available is the positions and orientation of the CFV, and the requirement is to estimate the forces and torque. Therefore Eq. III.4 can be inverted and written as Eq. III.9 for force estimate along X and Z, where t_x, and t_z are variables defined by Eq. III.10.

$$\begin{cases} \hat{f}_x = a_2(\frac{t_x - v(x_{CFV})}{a_1})^{(\frac{1}{r_x})} \\ \hat{f}_z = a_2(\frac{t_z - v(z_{CFV})}{a_1})^{(\frac{1}{r_z})} \end{cases} \tag{III.9}$$

$$\begin{bmatrix} t_x \\ t_z \\ 1 \end{bmatrix} = \begin{bmatrix} \cos\alpha & \sin\alpha & -x_I \\ -\sin\alpha & \cos\alpha & -z_I \\ 0 & 0 & 1 \end{bmatrix} \begin{bmatrix} x_{CFV} \\ z_{CFV} \\ 1 \end{bmatrix} \tag{III.10}$$

Considering the symmetry of the sensing platform, the mechanical parameters along X and Z axes were considered equal. Therefore, the different mechanical coefficients formulated in terms of different parameters are considered same along both axes.

$$R = \sqrt{x_L^2 + z_L^2} \tag{III.11}$$

$$\hat{T} = f_{eq} R sin\gamma \tag{III.12}$$

$$f_{eq} = \sqrt{\hat{f_x}^2 + \hat{f_z}^2} \tag{III.13}$$

$$\gamma = tan^{-1}\frac{z_L}{x_L} + tan^{-1}\frac{\hat{f}_z}{\hat{f}_x} \tag{III.14}$$

The torque estimation ($\hat{T}$ can be defined as written in Eq. III.12) requires the distance between the point of load application (x_L, z_L) and the center O_W, this is marked as R (Eq. III.11). Where, f_{eq} (Eq. III.13) is the overall force which makes an angle γ (Eq. III.14) with frame O_W.

III.4 FABRICATION PROCESS

Silicon was chosen for the proposed sensing platform fabrication (Wafer size 5 inch, thickness 500 μm). Because it is widespread, and enables to fabricate high aspect ratio beams. Also, its hookean nature with minimized energy dissipation and less fatigue behavior allows a high repeatability. The fabrication process was started with a silicon-on-insulator (SOI) wafer with 1.2 μm SiO_2 coating on both side (Fig III.6). One side (along with side wall) of this coating was removed with Buffered Hydrofluoric Acid (BHF) etching by keeping the other side with a protective resist. The negative resist was then deposited with a designed mask, followed by resist deposition for Deep Reaction Ion Etching (DRIE). This process was done for the bottom and top side with deposition of Aluminium (electrode patterning) with the use of protective resist deposition in between. Finally, the etching of aluminium was made followed by remaining residue cleaning with acetone and ethanol respectively. As defined encoding in Fig III.4, each square was targeted to be of 3 μm resulting into physical period of 6 μm. The fabrication result is shown in Fig III.7, the obtained encoded squares on the fabricated CRB was measured 3.01 μm, resulting into less than 0.4 % fabrication error.

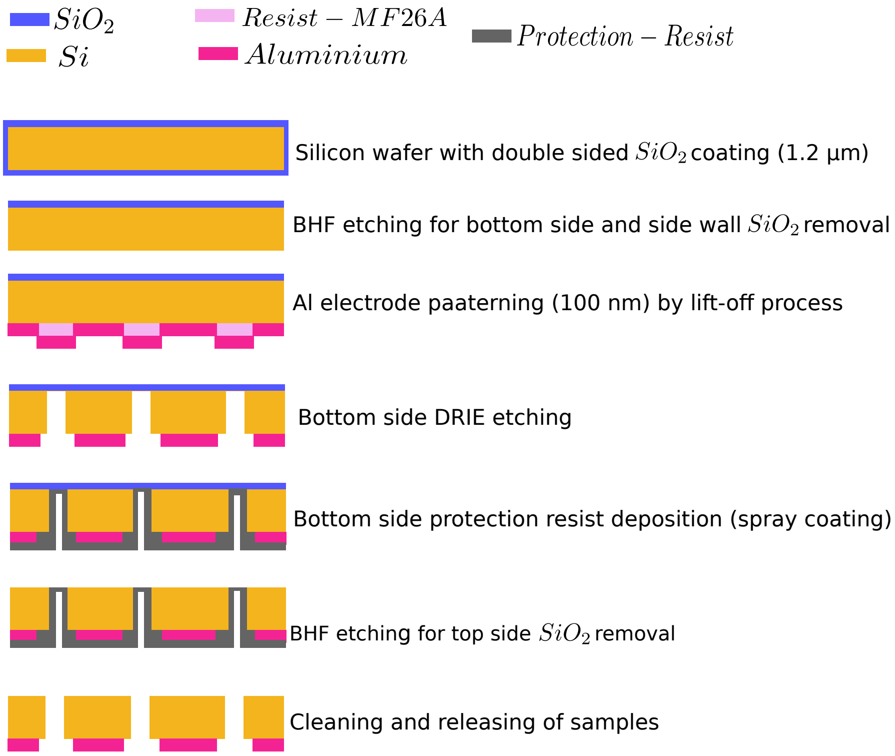

Figure III.6 – Summarized Fabrication Process

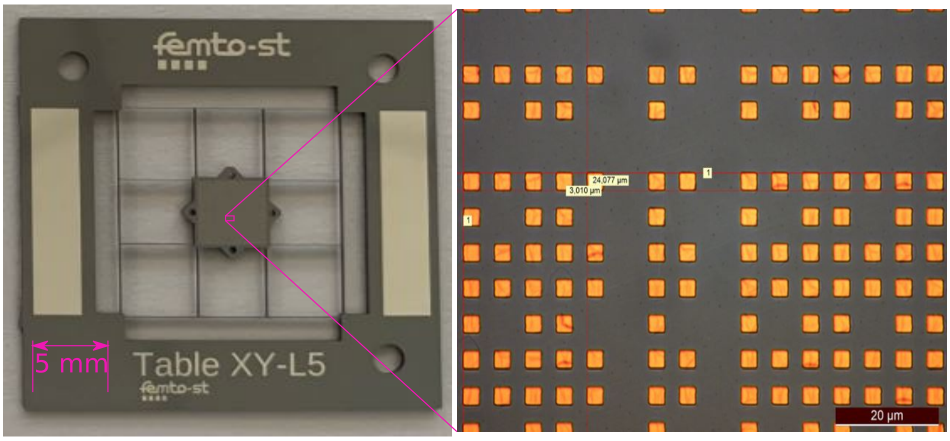

Figure III.7 – Fabricated Platform

III.5 EXPERIMENTAL WORKS FOR IDENTIFICATION

The experimental validation of the model requires the knowledge of the force applied. For this purpose, the force is applied along the Z axis of the CRB by means of a reference force sensor fastened to a 1D micro-positioner. The beam deformations induced by micro-positioner displacements z_{Pos} result in displacements of the CRB which is measured by vision, and the force f_z is synchronously measured by the reference force sensor. In this way, force-displacement curves representative of the platform behavior can be recorded and used for the identification of model's parameters.

III.5.1 Principle and Setup

The experimental setup built includes 5 main components and is shown in Fig. III.8. The platform is placed with its encoded plane facing a monitoring camera. A reference force sensor; either a TEI FSB-101 with a 500 mN range or a FemtoTools FT-G102 sensing finger with a 250 μN range is used, depending on a long range validation or resolution validation requirement. The reference force sensor is attached with a M122.2DD micro-positioner from Physik Instrumente. The positioning of the reference sensor probe relatively to the platform is made with the help of a side view camera. The cameras used are IDS USB 3 uEye CP, with a 20x magnification objective from Mitutoyo integrated with OPTEM ZOOM 70 XL in the case of the pattern monitoring camera.

III.5.2 Experimental Results

Fig III.9a presents the load applied to the CRB of the platform where force measured by the reference force sensor versus the displacement of the positioner is shown. z_{Pos} and f_z are respectively the input displacement of the positioner and the sensed force by the reference force sensor, which is used in the identification process of the different parameters defined in the model (sampling rate of 0.408 samples/sec). The resulting motions of the CRB are retrieved through the pattern monitoring camera and the vision algorithms. The results obtained are depicted in Fig III.9b, where the Z-X planar motion of CFV is shown, along with the rotation of the platform. The obtained motion along X and the rotation is very less compared to the force application direction (along Z).

III.5.3 Parameters Identification

The defined system parameters were identified using a non-linear least square method to fit the reference force measured by the TEI force sensor. The functions u(def) and v(def) for variables r_x and r_z (Eq. III.6 to Eq. III.8) define the non-linear region behavior.

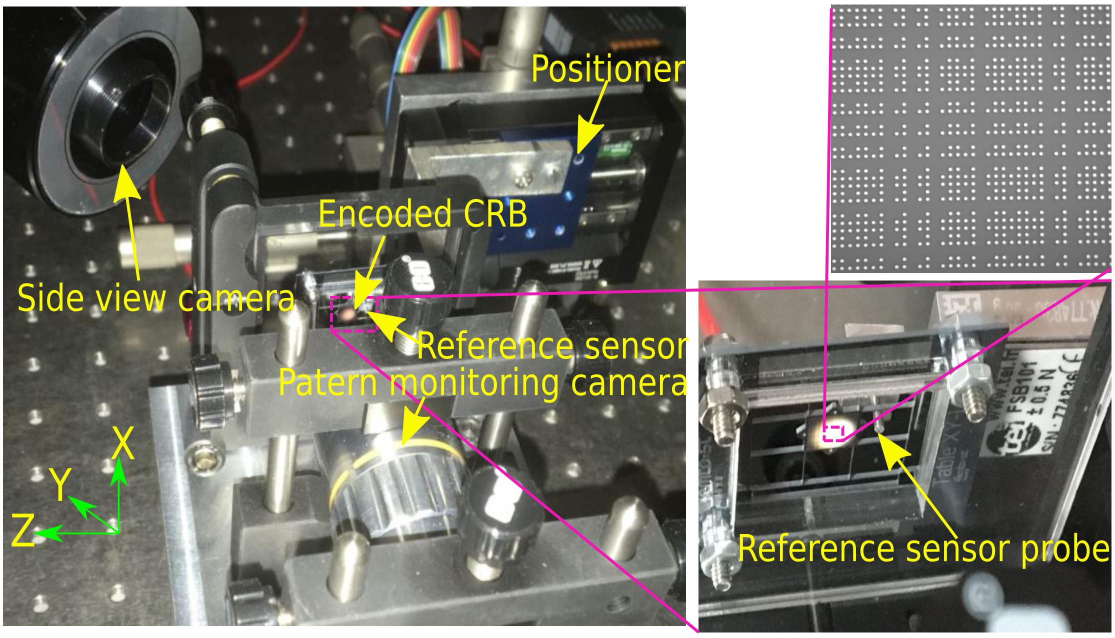

Figure III.8 – Experimental Setup

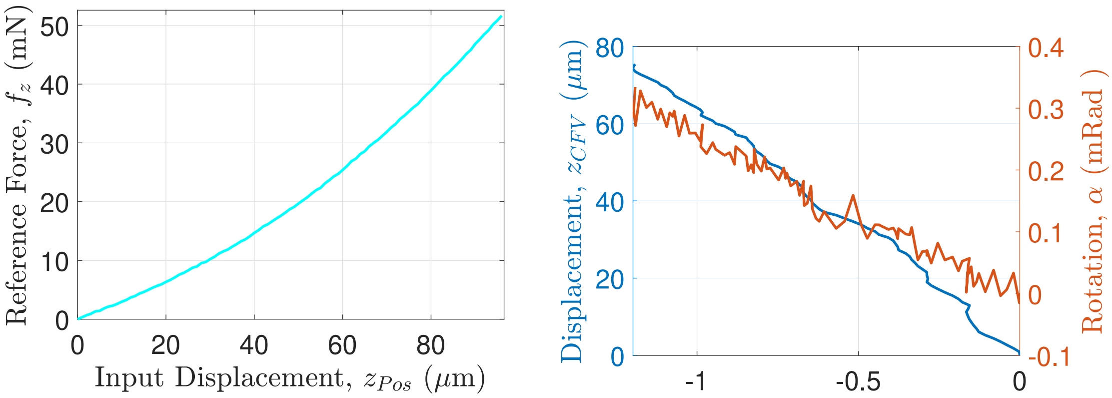

(a) Reference force applied by micro-positioner (Experimentation)

(b) Information from Vision Sensing

Figure III.9 – Experimentation, input motion, reference force and according position sensed by vision

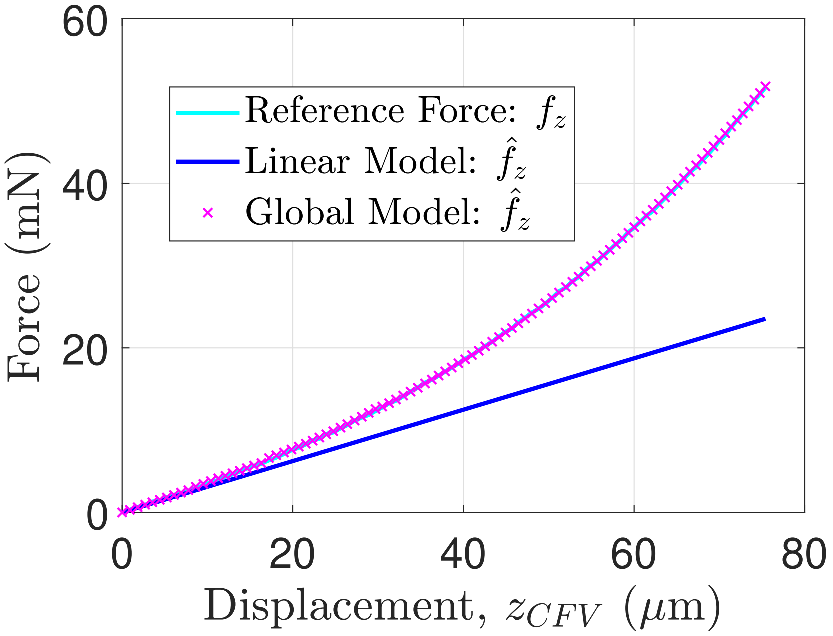

Figure III.10 – Model fitting and parameters identification

i	a_i	b_i	c_i
1	97.58	-0.06	0.9
2	0.034	1.2	-43.2
3	0.36	1.015	-38.67
4	–	0.992	-38.19
5	–	1.025	-37.61

Table III.2 – The Identified Parameters

In order to minimize the non-linearity error, i=5 was chosen, resulting into splitting of operational regions into 6 sub-regions (1 linear, and 5 non-linear). The chosen boundaries of the defined sub-regions d_1, d_2, d_3, d_4, d_5, d_6 were respectively 8, 17, 30, 40, 76 and 115 μm. The 5 identified parameters for b_i and c_i are shown in the Table III.2. A comparison of the behavior estimated from the model and measurements from the reference force sensor is shown in Fig III.10. The force-displacement relation working in the linear zone (def $< d_1$) if extrapolated similarly in non-linear zone then the obtained estimation ($\hat{f}_z$) would be far from the true value (f_z). This linear extrapolation plot is marked as "Linear Model", whereas the defined model with inclusion of non-linearity is marked as "Global Model". From the Global model, the estimated force ($\hat{f}_z$) is very close to the measurement provided by the reference force sensor (f_z). The error obtained is within 0.5 % for a force range of 52 mN. In all the subsequent estimation, we would be referring to the Global model for the estimation.

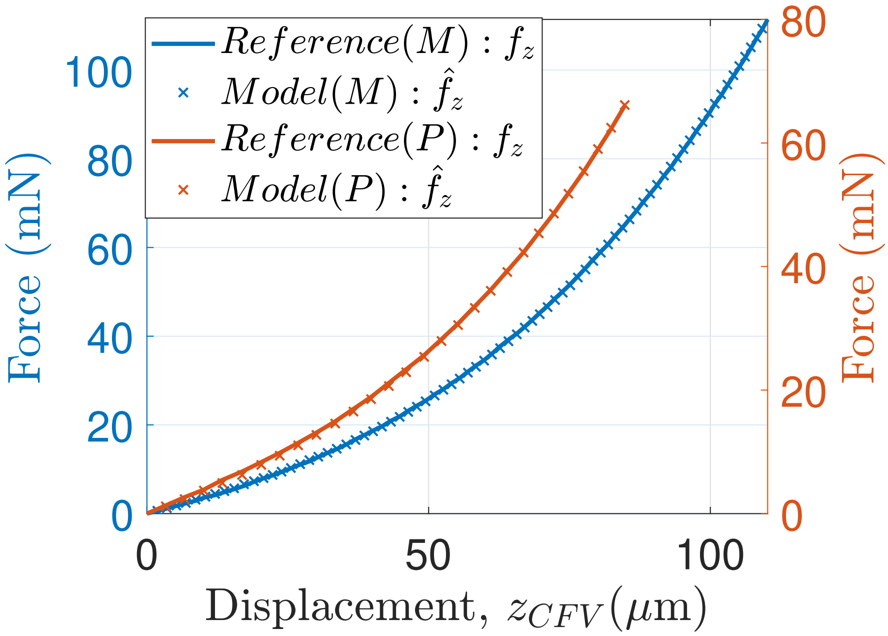

Figure III.11 – Force, Z: Model Validation with force at M and P

III.6 Model Validation

With the help of identified parameters, given in the Table III.2, validation of the model is made further for two different experiments. With defined point M and P on the CRB from Fig. III.4a, additional studies of behavior were made when a force is applied at M (as for the identification) but in other case force applied at P (specific interest to study the coupling between the axis). With the help of the model, the force along Z for the two cases is estimated. The estimated force in comparison to measurement from the reference force sensor is shown in Fig III.11, marked M and P for the force applied at M and P respectively. The applied force at M and P are respectively 110.2 mN and 66.15 mN. The calculated standard deviation in all the presented cases is found less than 0.35 mN, which is less than 1 % of the validated range. The obtained error between the force estimate and the reference force is less than 1 % for all the cases from identification to validation and is shown in Fig III.12.

III.6.1 Estimation of Torque along Y and Force along X

The coupling presence, which includes the force along X axis, and torque about the plane can be accordingly estimated from the defined model. In the absence of a commercially available multi-axis reference force/torque sensors (of the required precision, and workspace), the estimation error is not included for these components but based on the fabrication symmetry along the two axes the estimation can be justified.

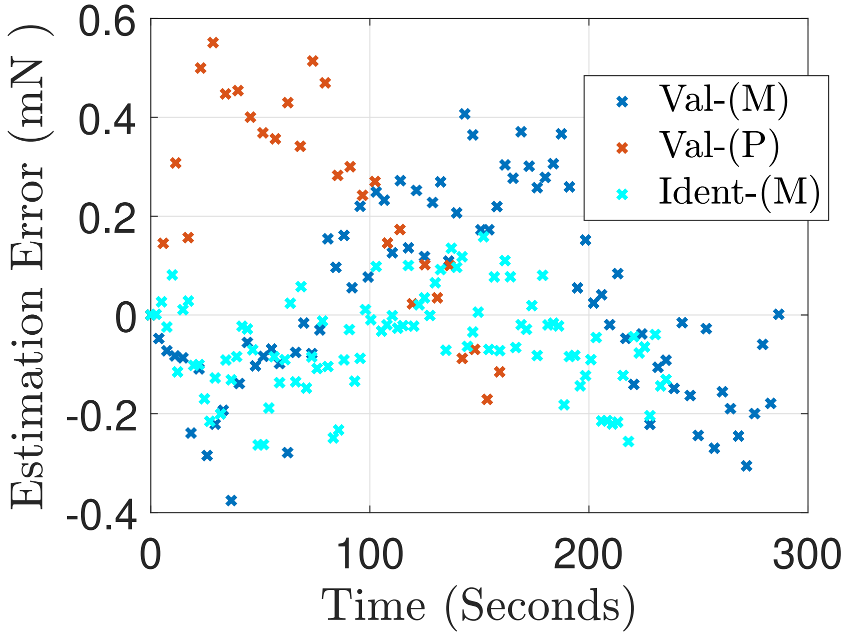

Figure III.12 – Estimation error for the identification (Ident-(M) for force at M) and validation (Val-(M) and Val-(P)), respectively for force at M and P

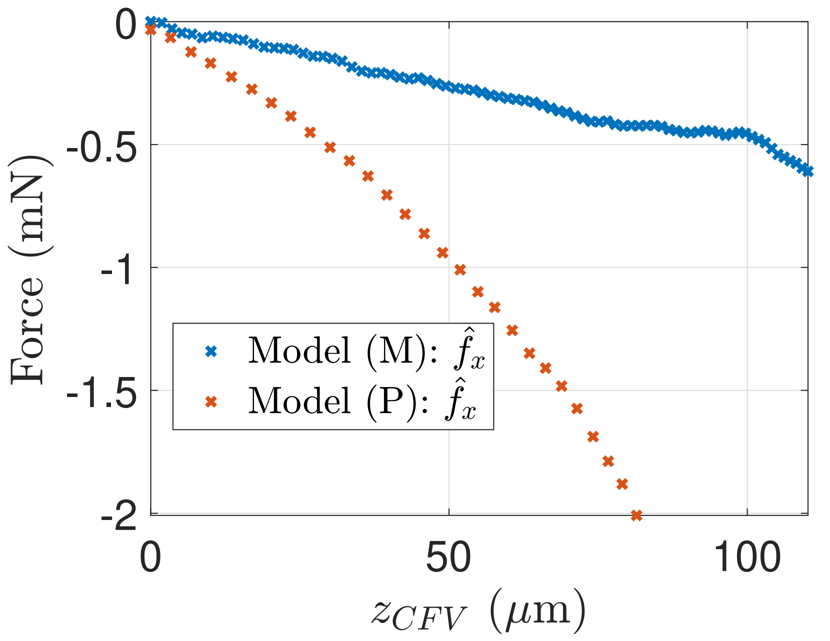

Figure III.13 – Estimation of Force along X

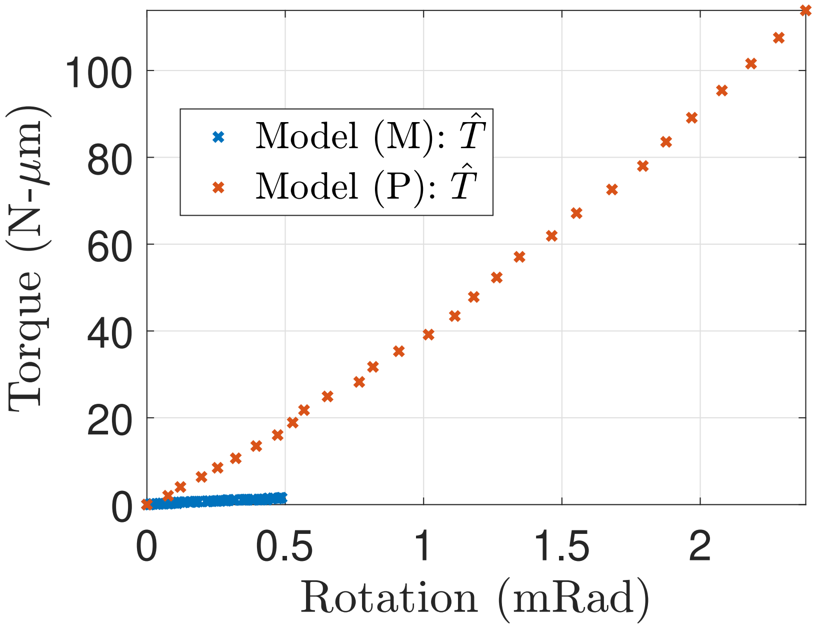

Figure III.14 – Estimation of Torque about Y

Force along X is shown in Fig III.13 against the displacement of CFV along Z, this represents the coupling of the two axis which is higher when the force is applied at P than M. The estimated torque is shown in Fig. III.14, which is higher when the point of application is at P than that at M. The applied force at M is significantly higher than that at P, as the rotation obtained under load at P is much higher than that at M. Moreover, the force along X is also higher in case of load at P than M, this mainly resulted from beam relaxation, which is higher in case of load application closer to beams (case of P), than that at M which is far from the supporting beams around.

III.6.2 Sensing Resolution Validation

In the previous sections a long range and repeatable sensing capability was demonstrated. In order to validate the high RtR2 of our proposed sensor, an experimental demonstration is needed. One required change in the experimental setup used previously, is the reference sensor with a high sensing resolution.

Also, the available freespace between the CRB and the beams is very limited ($<$ 5 mm). So keeping the mentioned requirements into consideration, FemtoTools FT-G102 sensing finger is used. A staircase input of 250 nm step-size was given to the positioner. Then force from the reference sensor and positions from vision algorithm were measured (sampling rate of 0.285 samples/sec). With the defined global model, an estimate of the force was made. The experimental and estimated results are shown in Fig III.15. The obtained result estimate the force with a value close to the mean noise value of the referenced force sensor. The obtained behavior

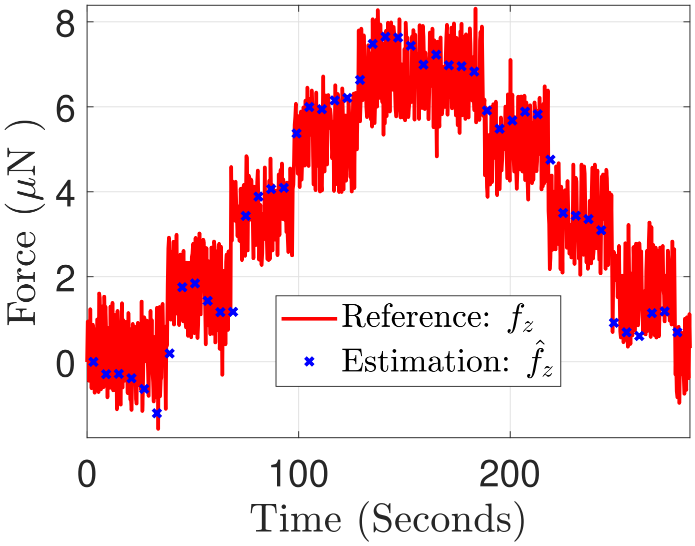

Figure III.15 – Validation of Resolution

validates a sensing resolution less than 2 μN (approximately 1.8 μN). Mainly this order of force brings the proposed system in linear zone, meaning that u(def) (Eq. III.7), v(def) (Eq. III.8) will be 0. Based on the observation, the defined linear region $d_1 = 8$ μm, allows the model to make a decision and adapt the according linear relation. Therefore the same model, with same identified parameter is able to validate a high resolution sensing capability as well.

III.6.3 Performance Repeatability

The repeatability test of the proposed force sensor was done (sampling rate of 0.166 samples/sec) shown in Fig. III.16, the sensed deviation error was found well in the proposed 1 % range. The corresponding force sensed by reference sensor and that from the estimation is shown in Fig. III.16a, while the estimation error is shown in Fig. III.16b. The obtained non-linearity is within 0.5 %.

The use of the encoded platform as a force sensor includes two main components in non-linearity (combining all the mechanical phenomena), the first component is from the vision sensing (which sense the planar positions directly). Whereas the second roots are from the modeling itself. The proposed force sensor includes the advantage of working in linear zone, along with added benefits of higher range sensing capability with inclusion of non-linear sensing zone, making its sensing acceptability over long range. The performance obtained with the proposed sensor is highly repeatable with standard deviation less than 1 %.

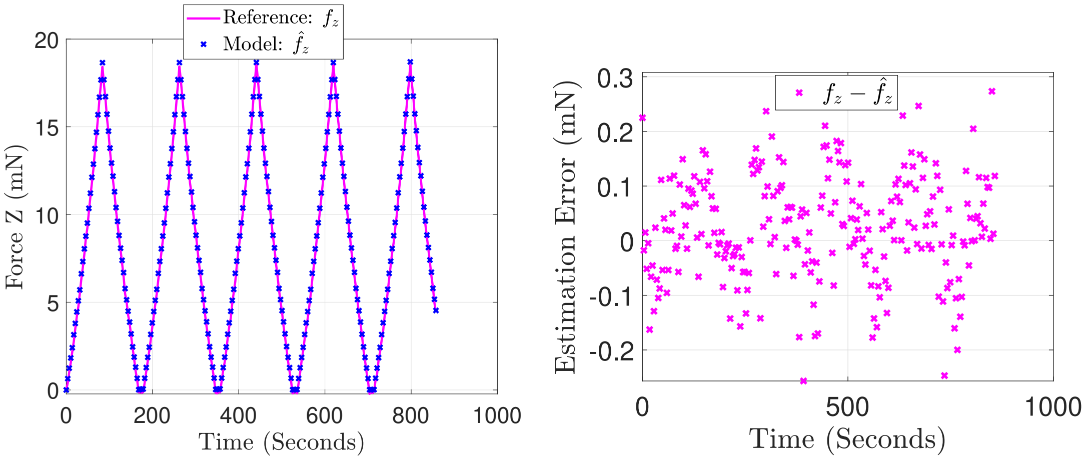

(a) Force along Z, Repeatability Test (b) Estimation Error, Repeatability Test

Figure III.16 – Repeatbility of the proposed sensing platform

III.7 CONCLUSIONS

A compliance structure with high form factor to restrict the motion in focal plane of the camera is designed for the development of the proposed device. A dedicated 2D encoding strategy with a physical period of 6 μm is employed, which enabled a long range planar position sensing. This device is fabricated in clean room to meet the encoding, and mechanical requirements. This work proposes a methodology to generalize the force sensing over a high range keeping advantage of linear and non-linear operational zone together. The proposed device is capable of sensing forces along 2 planar axis and torque along the normal to the sensing plane. Experimental studies demonstrated the resolution of 2 μN over a sensing range of 110 mN. The estimation error and the non-linearity of the proposed sensors is less than 1 %, but with the use of non-linear global model, a disruptive range-to-resolution ratio is successfully demonstrated. This bolsters wide acceptability of the proposed sensors among various tasks at micro-scale.

Chapter IV

A 2-Axis Piezoresistive Force Sensing Tool

IV.1 INTRODUCTION

With a wide requirement of multi-axis local states knowledge in the different micro-scale tasks like rotation, gluing etc. (as discussed in Chapter I and II), there is potential requirement of multi-axis instrumentation. Chapter III, presented a multi-axis sensing platform which demonstrated a high range to resolution sensing capability. In this chapter, the instrumentation of a tool for multi-axis force sensing is targeted. The multi-DoF of force sensing can bring a diverse task handling capability, but in the case where sensor is external to the interacting tool, then the corresponding frames (tool and sensor's frame) must need to be suitably positioned so as to be in convenient sensing range. Also, such sensors require free-space between the sensor and the tool of interest (e.g. laser or vision based sensor etc.). To address this key issue, there is requirement of instrumented tools/grippers capable of multi-DoF force/position sensing. Instrumented tool allows the measurement (within its calibrated range) without its dependency over specific positioning as in the case of external sensors, therefore strengthening an optimized use of work-space for varieties of tasks.

There are different possible approaches to measure the forces (as discussed in Chapter I), and specific state can be used to define the sensing principle based on the requirements. In this work, a 2-axis force sensing tool is presented which works on piezoresistive principle. The key interest to use the piezoresistive sensors is in precise sensing capability that may be used over a long measurement range. Indeed the disadvantage remains in its sensitivity to environmental changes such as from temperature and humidity. But, for the use where the temperature and humidity changes are not significant (as defined with temperature coefficient of the material chosen), then the piezoresistive sensor becomes a preferable candidate. The proposed tool can be integrated with the appropriate actuator to perform variety of tasks at micro-scale (like characterization of tissues and fiber as discussed in Chapter I), but can also be used for the development of microgripper (discussed in Chapter V). The sensing tool development constitutes of assembly of a passive tool and two sensing devices (cavalier). The separate fabrication of the devices (passive tool and sensing device) insures use of dedicated process individually, which minimizes the fabrication complexity for the devices (sensing device in particular). Moreover, the sensing devices can be assembled with varieties of passive tools to perform different tasks, therefore giving its wide acceptability for different requirements. This chapter starts with the discussions on sensing principle, system design and working (section IV.2), thereafter FEM analysis of the device is presented in section IV.3. Based on the proposed design, fabrication process of the devices, their assembly to develop the sensing tool is discussed in section IV.4. The developed sensing tool performance especially when there is no any external forces, and when the force is applied along specific sensing axis is experimentally studied and the corresponding characterization works are presented in section IV.6. Finally, conclusion of the presented works in this chapter is discussed in section IV.7.

IV.2 SENSING PRINCIPLE AND DESIGN

In this section, the sensing principle and the design of the system is discussed. The key phenomenon includes, the physical change detection in terms of the resistance change and mapping of the detected change in terms of force change. This work was done in collaboration with CITHADEL [CITHADEL 19] project which also targeted piezoresistive based force sensor development for mechanical characterization of surfaces at the micro-scale.

IV.2.1 Sensing Principle

Any structure in general, which allows the passage of electric current exhibits some finite resistance, or in other case it would be a pure insulator. The different categories possible in terms of the materials conductivity defines the material as semiconductor, conductor or a super-conductor (where electrical resistance vanishes with the introduction to magnetic behavior).

$$R = \rho \frac{L}{A} \tag{IV.1}$$

Eq. IV.1 defines a general equation of resistance R, dependency over resistivity ρ, length L and cross section area A of any conductive structure as shown in Fig. IV.1. So, the resistance of the structure is dependent on the geometry, and the material property. In order to use any conductive structure as a piezoresistive transducer, the key factors needed are the mechanical reversability (more particularly elasticity), change of electrical resistance and the resistance change detection circuit such as a wheatstone bridge. The resistance change is not solely dependent on the geometry, or the resistivity, but also on the temperature. Based on the choice of material there is a parameter called “temperature coefficient”, which defines the dependency of resistance on the temperature. This dependency could be constant, or linear in certain temperature range or non-linear. So, in order to use any conductive-mechanical structure as a piezoresistive transducer, the device must need to have stable behavior within the operating temperature. This ensures that the significant resistance change comes from the mechanical stress, not from the small fluctuation in the temperature (or humidity which is indirectly linked). Therefore the temperature dependent element is not included in the definition of resistance in Eq. IV.1. The following discussions in this chapter will only consider the pure piezoresistive effect, which constitutes the impact of external force towards change in electrical resistance.

The change of resistance (ΔR) can be written in relation with Poisson’s coefficient ν, strain ε, and resistivity change $\Delta\rho$ as in Eq. IV.2.

$$\frac{\Delta R}{R} = G\varepsilon \quad \text{where} \quad G = 1 + 2\nu + \frac{\Delta\rho}{\varepsilon\rho} \tag{IV.2}$$

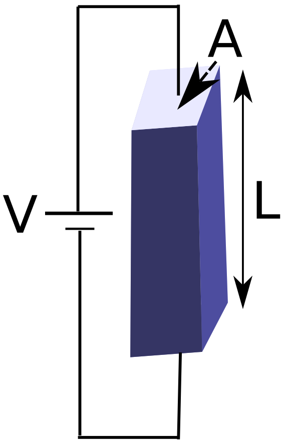

Figure IV.1 – Resistance dependency on Geometry

G written as in Eq. IV.2 defines the resistance change sensitivity and is called Gauge factor. In [Greaves 11], change of Poisson's ratio (ν) under the strain for different types of material is discussed. In context of macroscopic isotropic materials, for extremely compressible material like foam, ν can go negative up to -1, whereas for material like rubber it can reach maximum value of 0.5. Therefore, the dependency over the geometrical parameter to improve the sensitivity is very limited in isotropic materials. For anisotropic materials, although there is no such limits but the possible variation of ν is not very significant [McCarthy 14] and so in defining the Gauge factor (G). Therefore the sensitivity needs to be seen on other dependent factor which is the resistivity of material. Conventional metal strain sensors typically enable a gauge factor of 2-5, but metal grid strain sensors based on all-solution process can exhibit also a high gauge factor (4685.9 in [Oh 18]). A further higher gauge factor can be obtained with the approach of "crack propogation". Cracks can be introduced in the transverse direction of applied stress, especially in the case of plasma treated polymers. The introduced cracks lower the conduction and so resulting into increase of electrical resistance. Such an approach based on crack depth is discussed in [Park 16], where a very high gauge factor of 16000 was demonstrated. The use of Pt and Au films in the "crack propogation" approach lacks stretchability (typically < 2 %). In the context of micromanipulation tasks the factor like stretchability, linearity and repeatability are highly important. A high gauge factor may have a very poor stretchability, and therefore need to be considered before the sensor development. Semiconductor like silicon can provide an interesting trade-off between the gauge factor (up to 200) and stretchability (> 10 % possible) which can be tuned[Yang 13] based on the substrate modulus. For these discussed reasons along with considerations in terms of fabrication complexity and costs, the proposed work used p-type silicon for the piezoresistive sensing tool fabrication.

IV.2.2 System Design

The piezoresistive sensitivity is defined by the resistance change detection capability. The sensitivity of the device is also dependent on other factors, other than the choice of material as discussed in subsection IV.2.1.

$$\frac{\Delta R}{R} = c_k G \varepsilon \tag{IV.3}$$

The sensitivity of a p-type silicon structure can be further increased (Eq. IV.3) by introduction of cavity around the deformation. An introduced cavity in [Komati 14a] made 25 % increase in sensitivity, with $c_k = 1.25$ (scaling factor). Basically, the introduced cavity lowers the mass and so the moment of inertia, resulting into scaling of the stress distribution in the sensitive part. Therefore, the cavity needs to be taken into account for the system design.

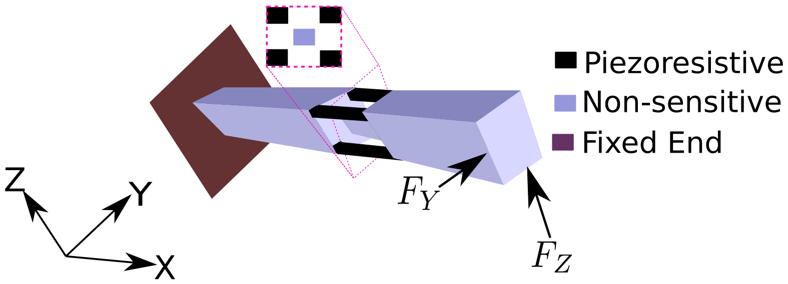

Figure IV.2 – Sensing Principle

In order to sense force along the 2 orthogonal axis, one key important requirement is the distribution of piezoresistive sensing structure uniformly around the neutral axis (leading to have maximization of the stress distribution on the piezoresistive part). Also, to allow scaling of strain distribution, the sensing part need to be suitably distant from the point of load and the neutral axis. Moreover, the tool must need to have one end fixed, which is important to have compression-elongation phenomenon together along the suitable gauges depending on the force applied (discussed in subsection IV.2.3). Work of [Komati 14a], constitutes the design compatible for single axis sensing at a time , extension of which would lead to Fig. IV.2, meeting the mentioned requirements, where the four piezoresistive gauges are distributed uniformly around the cavity and neutral axis of the fixed non-piezoresistive (not containing the sensitive gauges) structure.

IV.2.3 System Working

The micro-scale piezoresistive tool needs a clean room fabrication, which mainly includes planar additive or etching process. Single wafer fabrication of such a device may introduce complexity in the process, with potential fabrication uncertainties. To avoid the device fabrication complexity, and to target a mass production of varieties of sensing tools requirement, the according device fabrication may be

Force	S_1	S_2	S_3	S_4
F_Y	+	-	-	+
F_Z	-	-	+	+

Table IV.1 – Load Impact with direction

divided into 3 parts. In the first part, a mass production of piezoresistive gauge containing cavalier can be targeted, secondly passive tool based on specific task requirements can be fabricated separately. In the third part, the two cavaliers can be used to assemble with the fabricated passive tool in a way so as to be close to the configuration of Fig. IV.2. With this scheme, a 2-axis force sensing piezoresistive tool's design is proposed in Fig. IV.3. The proposed design consists of three parts, passive tool and two cavaliers which includes the piezoresistive strain gauges. The cavalier (Fig. IV.3c) as additional parts termed as "Mechanical Handling Part", which can be useful during the process of assembly with passive tool (detailed in subsection IV.5) and latter removed to have configuration of Fig. IV.3a, where the two cavaliers are sandwiched around the passive tool. Overall, there are 5 beams passing through the cavity, 4 beams are 4 strain gauges, whereas 1 beam is from the passive tool used (Fig. IV.3b). The central beam of passive tool provides link between the two sides of the cavity (along its length), therefore useful to minimize the number of parts and hence the complexity for the sensing tool development.

Definition of the gauges with respect to the defined frame in Fig. IV.2 remains same for the Fig. IV.3, therefore the top gauges are S_1 and S_2, whereas the bottoms are S_3 and S_4. The corresponding resistances are R_1, R_2, R_3 and R_4 respectively.

Under the applied load along +Y (F_Y), the gauges S_1 and S_4 would be elongated, whereas gauges S_2 and S_3 would be compressed. For load applied along +Z (F_Z), the gauges S_1, S_2 would be compressed and the remaining S_3, S_4 would be elongated (opposite effect with reversal of direction). This behavior is listed in Table. IV.1, where "+" and "-" are used to indicate respectively elongation and compression of the gauges. Revisiting the obtained behavior along the two axes, it can be seen that behavior of two gauges remained same against the load along +Y or +Z, these two gauges are S_2 and S_4, where S_2 undergone compression for both the cases and S_4 undergone elongation in the respective two cases. Also, the other point that can be observed from the discussed behavior is, that the diagonally opposite gauges always kept the opposite behavior irrespective of the applied load in the two cases. These observations can be employed to decouple the force sensing along the two axes. The requirement is to transform the resistance change to force change. This transformation can be done with the voltage change detection, which can be done with the help of a "Wheatstone Bridge" circuitry. Using the two diagonally opposite gauges in a wheatstone bridge, two bridges can be defined (as shown in Fig. IV.4). The first bridge W_1 consists of gauges S_1 and S_3, whereas the second bridge W_2 includes gauges S_2 and S_4, each bridge powered with DC supply voltage V_{CC}. Each individual bridge is balanced under no-load

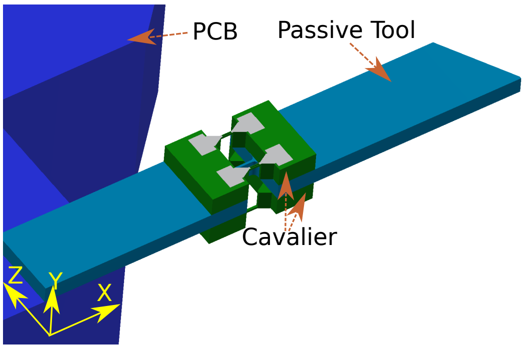

(a) Assembled sensing tool

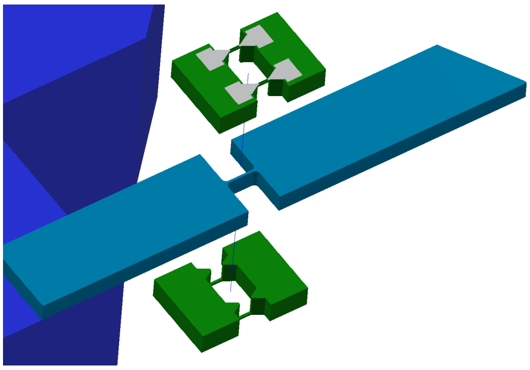

(b) Exploded view of assembly

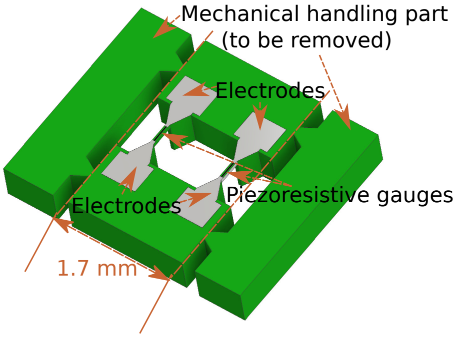

(c) Cavalier with electrodes and additional handling part

Figure IV.3 – Proposed design of the sensing tool

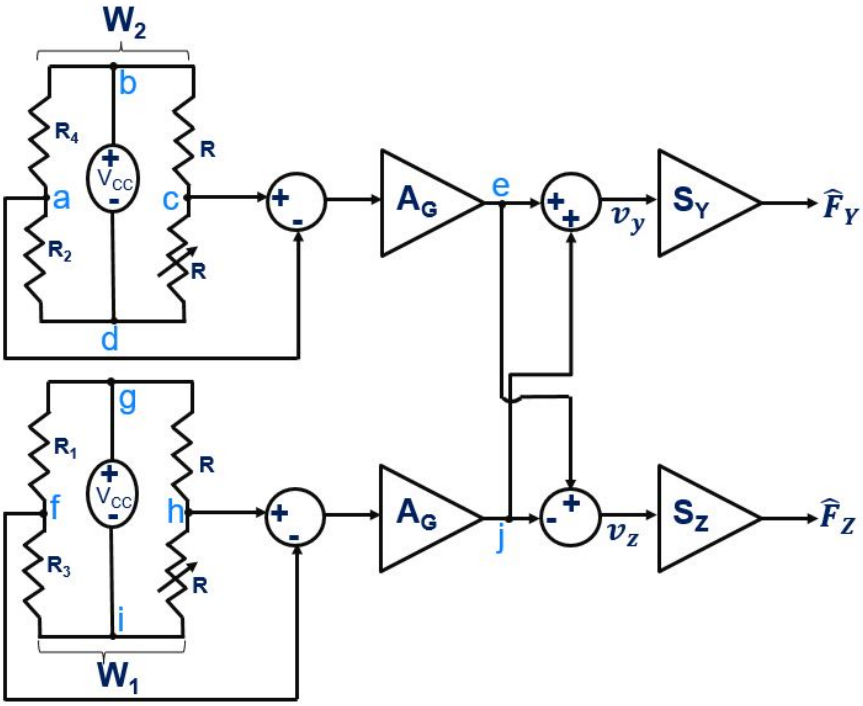

Figure IV.4 – Wheatstone Circuitry

with two reference resistors R, one of them can be a variable resistor (as denoted in Fig. IV.4) to facilitate the balancing of the bridge against any environmental variation (at no-load).

For an input supply voltage V_{CC} in parallel to the bridge W_1 and W_2, the respective mid-point voltages of the two bridges at no-load and in balanced condition are respectively given by v_{W1i} (voltage at point f and h) and v_{W2i} (voltage at point a and c) (Eq. IV.4).

$$v_{W1i} = \frac{R_3}{R_1 + R_3} V_{CC} \quad \text{and} \quad v_{W2i} = \frac{R_2}{R_2 + R_4} V_{CC} \tag{IV.4}$$

Under the balanced condition, both the middle points of each bridge will have the same potential (voltage at point a and c, and respectively at point f and h) therefore, the output of the differential amplifier used (with a gain A_G) for each of the bridge would be zero. As a result, the subsequent addition and subtraction of the two output voltages (from point e and j) from the differential amplifiers would also be zero. The respective additions and subtractions are done to decouple the two axes. Single wheatstone bridge and the two planar gauges are sufficient to detect the force along Y or Z, but not at the same time. The two bridges, and 4 gauges distribution are used to detect force along the two axes simultaneously. The detected processed voltage then need to be multiplied by the sensitivity S_Y, and S_Z respectively to estimate the force along Y and Z ($\hat{F}_Y$ and $\hat{F}_Z$).

When any load is applied at the sensing tool (in all the cases we would be referring to the tool's tip as point of load application), then the wheatstone bridge gets unbalanced which would be reflected in different mid-point voltage (point a, c and f, h) for the respective two arms of each bridge. In reference resistors arm (part of W_1 and W_2 where we have R) the mid point (point c and h) voltages would remain same as that defined for no load case, but the arm containing the piezoresistors would have a different mid-point (a and f) voltage following the changes in their respective resistances. Assuming an infinite impedance of the differential amplifiers used, the current passing through them can be neglected compared to the current passing in the branch, therefore if ΔR_1, ΔR_2, ΔR_3 and ΔR_4, are the change in resistance in R_1, R_2, R_3 and R_4 respectively, then the new mid-point voltages v_{W1}, v_{W2} (respectively in bridge W_1 and W_2) can be defined as given in Eq. IV.5.

$$\begin{cases} v_{W1} = \frac{R_3+\Delta R_3}{R_1+R_3+\Delta R_1+\Delta R_3} V_{CC} \\ v_{W2} = \frac{R_2+\Delta R_2}{R_2+R_4+\Delta R_2+\Delta R_4} V_{CC} \end{cases} \tag{IV.5}$$

The overall voltage change detected along the Y and Z axis can be given as v_y and v_z respectively (Eq. IV.6), where A_G is the amplification gain from the differential amplifier used in the circuitry.

$$\begin{cases} v_y = A_G[(v_{W1} - v_{W2}) - (v_{W1i} - v_{W2i})] \\ v_z = A_G[(v_{W1} + v_{W2}) - (v_{W1i} + v_{W2i})] \end{cases} \tag{IV.6}$$

Combining the corresponding voltage changes detected, the amplification and the processing, the force estimate along Y and Z can be written as Eq. IV.7.

$$\begin{bmatrix} \hat{F}_Y \\ \hat{F}_Z \\ 1 \end{bmatrix} = \begin{bmatrix} S_Y A_G & 0 & 0 \\ 0 & S_Z A_G & 0 \\ 0 & 0 & 1 \end{bmatrix} \begin{bmatrix} 1 & -1 & -(v_{W1i} - v_{W2i}) \\ 1 & 1 & -(v_{W1i} + v_{W2i}) \\ 0 & 0 & 1 \end{bmatrix} \begin{bmatrix} v_{W1} \\ v_{W2} \\ 1 \end{bmatrix} \tag{IV.7}$$

Ideally, when there is a force along one axis alone then there should not be any non-zero voltage along the other axis (no coupling), meaning that for F_Y alone, F_Z should be 0 and so the vice versa.

IV.3 SYSTEM ANALYSIS IN COMSOL

Before getting into fabrication of device, it becomes significantly important to estimate the behavior of the "to be fabricated device" from the design we have. This could be done using a theoretical/mathematical model or probably little efficiently using numerical simulation. We opted for numerical simulation of the sensing tool presented in the previous section using COMSOL Multiphysics,

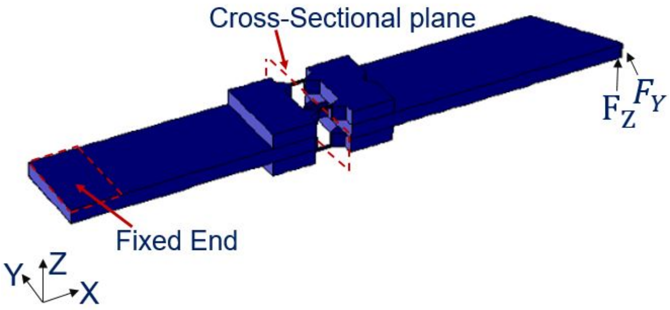

(a) Force application

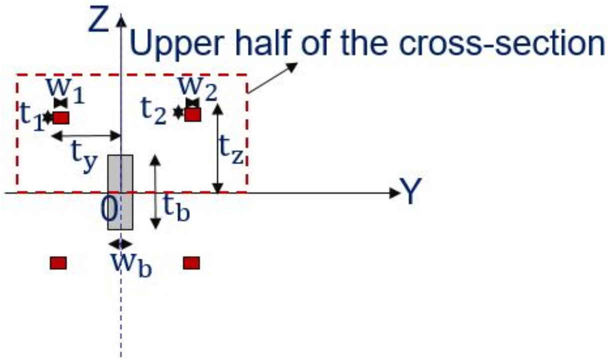

(b) Cross-Section of cavity

Figure IV.5 – Force application in COMSOL, and the cross-section view of cavity

Parameters	Value
t_1, t_2 (μm)	40
w_1, w_2 (μm)	50
w_b (μm)	50
t_b (μm)	350
t_z (μm)	575
t_y (μm)	525
Poisson's Ratio, ν	0.27
Piezoresistive Coefficient, π ($[TPa]^{-1}$)	718
Young Modulus, E (GPa)	170
No load Resistivity, ρ_0 (Ωmm)	0.25

Table IV.2 – Geometrical and mechanical parameters used in the COMSOL simulation

where the geometrical, physical and electrical parameters are defined in accordance with the standard data-sheet of the corresponding device to be fabricated (key properties listed in table IV.2).

In COMSOL Multiphysics, a surface load of 10 mN (across 50 μm × 50 μm tip area) is applied respectively along the Y and Z axis one-by-one. The stress introduced on the tool was calculated in COMSOL. Sensitivity of the device is a key parameter that can be estimated in COMSOL. In order to estimate that, the stress or strain information is needed. Stress or strain can be calculated directly in COMSOL across a defined region but in the experimental scenario it is difficult to have such possibility. In other way, it is possible to develop a model so that stress or strain can be estimated based on the force applied at the tip. We would cover this discussion in the next subsection.

IV.3.1 Modeling of the system for Stress/Strain Estimation

A model used in [Komati 12] can allow to estimate the stress depending on the cavity size. The corresponding estimation was based on the calculation of moment of inertia (I) and bending moment (M).

$$\sigma(z) = \frac{Mz}{I} \quad \text{and} \quad I = I_1 + I_2 + I_b \tag{IV.8}$$

As the piezoresistive gauges are around the cavity (Fig. IV.5a) and the longitudinal strain is developed along X axis, therefore the cross section information of the cavity is needed. A cross-sectional view of the cavity is shown in Fig. IV.5b, this cross-section is in accordance with the cross-sectional plane marked in Fig. IV.5a. Using the corresponding dimensions listed in Table IV.2, moment of inertia along the desired axis can be calculated. Stress is linearly dependent on z which is

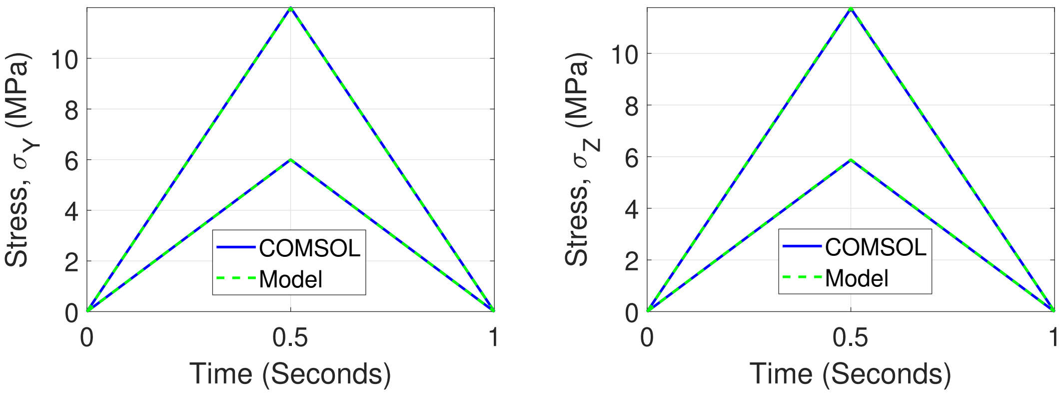

(a) For load along Y

(b) For load along Z

Figure IV.6 – Comparison of analytical model and COMSOL measurement

distance (where stress is intended to be calculated) from the neutral axis along the direction of applied load. To simplify the calculation, and using the symmetry of the proposed structure (around the cavity as shown in Fig IV.3a), only upper half of the system is sufficient to calculate the stress $\sigma(z)$. The respective moment of inertia of gauge S_1, and S_2 are marked as I_1, and I_2, and that from of the central beam (from passive tool shown in Fig IV.3a) as I_b in Eq. IV.8.

$$I_1 = \int_{t-t_1}^{t} w_1 z^2 dz \quad \text{and} \quad I_b = \int_{0}^{\frac{t_b}{2}} w_b z^2 dz \tag{IV.9}$$

Moment of inertia about S_1, and S_2, may be assumed equal (symmetric from neutral axis), whereas that along the central beam would be different. The corresponding calculation is shown in Eq. IV.9. The bending moment calculation includes calculation of reaction force (f_R) about the fixed end. Because of the stepped configuration (cavalier-passive tool transition) of the proposed sensing tool, the force applied F at the tip of the tool may be approximated to a different scaled value for a uniform configuration as proposed in [Al-Shareef 95]. But in the present case, because of the complexity from the cavity in the theoretical formulation, a proportional parameter a_L to the applied force can be used to define the bending moment at the step near to the fixed end. Indeed, its possible to directly identify a parameter proportional to F to estimate M but keeping equation of the form Eq. IV.10 allows to have an understanding of the reaction force knowledge which could be useful if the sensing tool is integrated with actuator or some other passive part.

$$f_R = F \frac{x_L + a_L}{x_a} \tag{IV.10}$$

As a result of stepped configuration and the cavity, the reaction force can be defined as in Eq. IV.10. Where x_L is the total length of the sensing tool, x_a is the distance of the cavalier (nearest edge) from the fixed end, parameter a_L can be identified from least square fit. Therefore the overall bending moment at the cavity center can be given by Eq. IV.11, where x_B is the distance of the cavity center from the fixed end.

$$M = x_L f_R - x_B F \tag{IV.11}$$

For external load F = 10 mN and 5 mN (under static condition), average stress is calculated for $z = t_z$ ($z = t_y$ for load along Y). Using the defined model, the corresponding estimate of stress (respectively termed as σ_Z and σ_Y for load along Z and Y) is compared with direct measurement from COMSOL, and is shown in Fig. IV.6. For calculation corresponding to load along Y (Fig. IV.7a) was made by exchange among t_1 and w_1, and replacing t_z by t_y in the defined equations for Z. The identified parameter a_L for the load along Z and Y was respectively found to be 3.38×10^{-3} and 4.79×10^{-3}. The identified parameter a_L is a proportional parameter and is dependent solely on the geometry of the sensing tool, therefore for a fixed geometry it works for any load value within the elastic limit of the structure. One key important side of the stress estimation discussed is in its dependency over geometry, and the load whereas the physical material parameters were not needed. This brings the interest of using the discussed model for experimental case, provided the geometrical parameters are same or in closed proximity of that used.

IV.3.2 Electrical Connectivity and Gauge Factor Calculation

Now the interest in this subsection is to combine the electro-mechanical behavior by analysing the strain change against the resistance change, with which the sensitivity and its according improvement from the cavity can be analyzed.

$$[\rho] = \rho_0(1 + [\pi][\sigma]) \tag{IV.12}$$

A 5 V DC voltage was applied across the length of the gauge. As there is change of resistivity ρ under the applied stress (Eq. IV.12), therefore there is change of resistance. With the measurement of the resistance change, the gauge factor G can be estimated using Eq. IV.2. Assuming isotropic distribution of stress, the strain along X and current density was computed from COMSOL. The according resistance can be calculated by knowing the cross section area of the gauge, current density and the applied voltage. The relative change in resistance against the strain (ε_Y, ε_Z respectively for load along Y and Z) computed from COMSOL is shown in Fig. IV.7. As the gauge factor is a constant parameter, and therefore irrespective of the load (in the elastic range), the slope of relative change in resistance against the strain should be constant. In Fig. IV.7 slope of the plot for 2 different loads (5 mN and 10 mN) is constant which is in accordance with our assumption (no temperature effect included). The slope of the relation was found 128.15 and 137.35, respectively for the load along Y and Z axis. The c_k value obtained (using

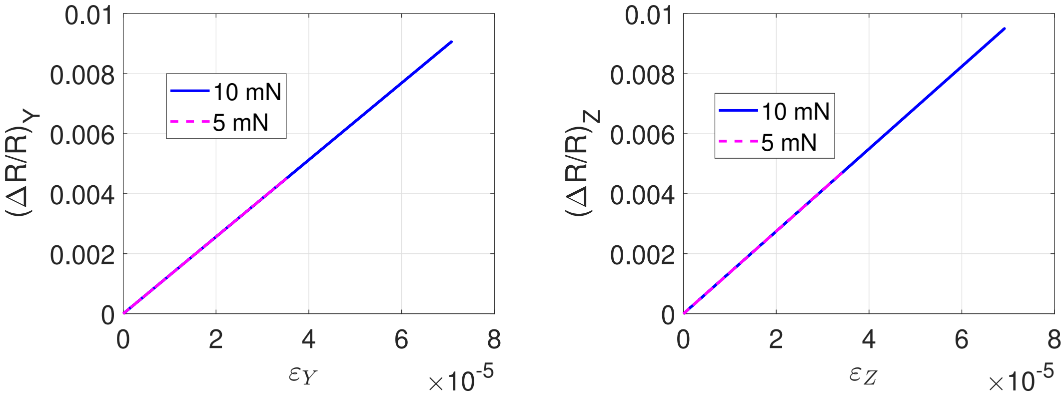

(a) For load along Y

(b) For load along Z

Figure IV.7 – Resistance change against the strain

Eq. IV.3) is respectively 1.05 and 1.125, along Y and Z axis, meaning 5 % and 12.5 % of sensitivity improvement in device along the corresponding axes, under the impact of introduced cavity.

IV.4 DEVICE FABRICATION AND ASSEMBLY PROCESS

In this section, fabrication and assembly process of different components of the sensing tool are discussed. The proposed sensing tool, consists of two types of component, one is the passive tool while second is the cavalier with piezoresistive gauges. These two type of components are fabricated separately with two different processes. Their respective fabrication process and assembly is discussed in the following subsections.

IV.4.1 Fabrication of the Passive Tool

In this section, the fabrication process of the passive tool is presented. The fabrication starts with a silicon wafer of 350 μm thickness. The top and bottom sides of the wafer went through the lithography followed by the electrode deposition (which may be used for wiring if needed). The DRIE etching technique was used for the etching process. Finally, the samples were cleaned and were ready to be used for the assembly process. A summarized flow of the fabrication process is shown in Fig. IV.8.

IV.4.2 Fabrication of the Cavalier

In our presented sensing configuration of Fig. IV.5a, the strain development and the electric current passage for piezoresistive sensing are in the same direction. Therefore the piezoresistive effect targeted is longitudinal effect. As the intention for the sensing is to use the strain along the gauge length, which means tensile strain in (100) silicon wafer should increase the mobility of electron in the <100> direction, while a compressive strain should increase the holes mobility in <110> direction (the miller indices representation is shown in Fig. IV.9).

Wafer orientation, type of doping, and the strain direction, can strongly influence the system behavior as discussed in [Billot 15]. We chose (100) wafer and to have <110> mobility direction, and therefore mask and wafer flat side were accordingly chosen for the fabrication process. The targeted strain development for piezoresistive effect is longitudinal, and the piezoresitive coefficient for the holes is 718 $[TPa]^{-1}$ which is higher than that of electrons -316 $[TPa]^{-1}$, which makes sense to go ahead for p-doped piezoresistive effect. The n-type wafer can be used to create p-n junction in reverse bias, so that there is no current leaking to the substrate. This approach of single crystal diffusion is a widely used method for doping.

In our case we used a commercially available 5 layered wafer (5" with 350 μm thickness) constituted of 1 layer of p doped Si (100), 2 layers of SiO_2, 1 layer of Si <111> and 1 layer of Si <100> (as shown in Fig. IV.10). The fabrication Process (Fig. IV.10) started from the top surface by performing the first lithography followed by DRIE etching. Thereafter thermal oxidation of 300 nm was made on

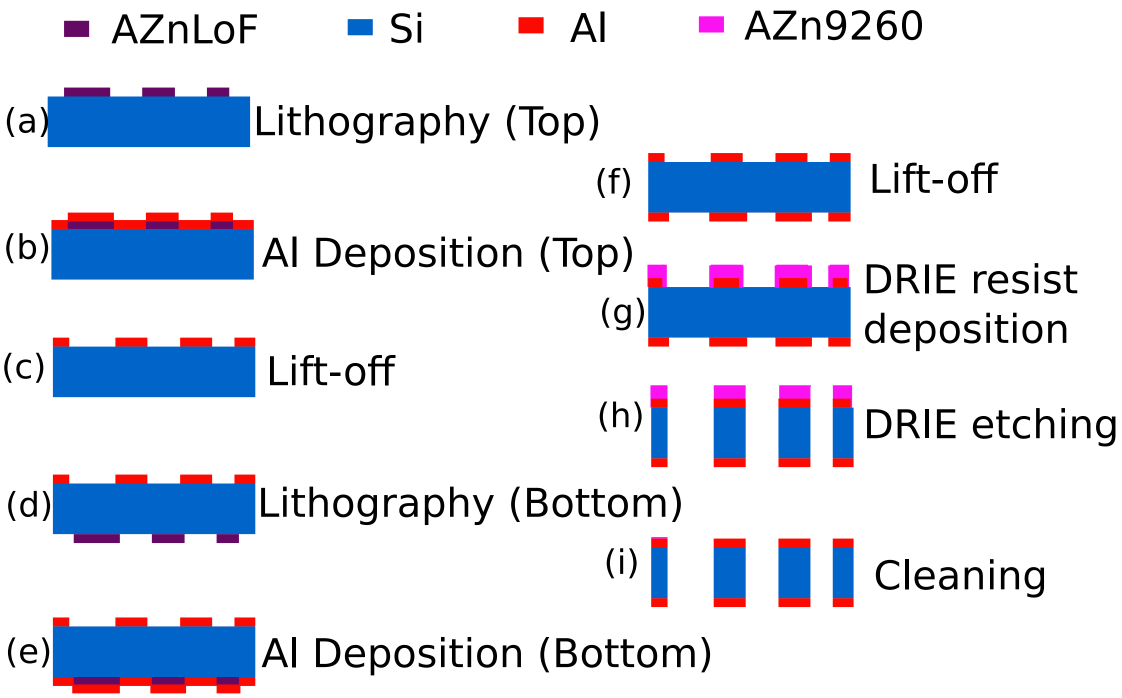

Figure IV.8 – (a)-(i) Fabrication steps for the Passive Tool

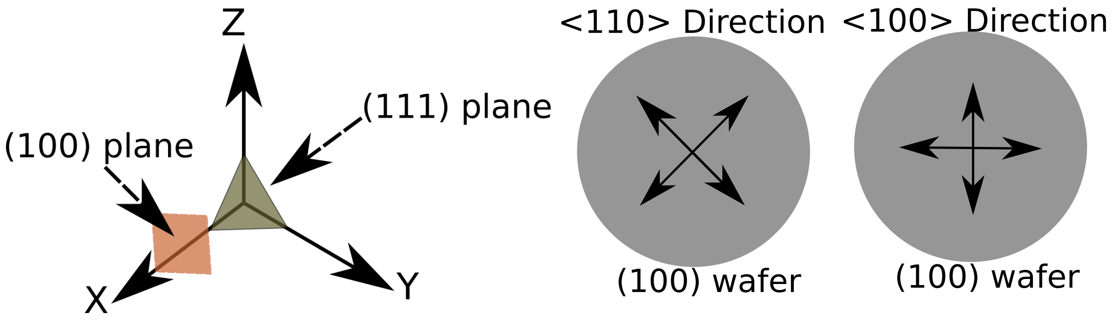

(a) Planes representation using Miler indices

(b) Wafer and carriers mobility direction

Figure IV.9 – Plane and direction representation for wafer and carriers

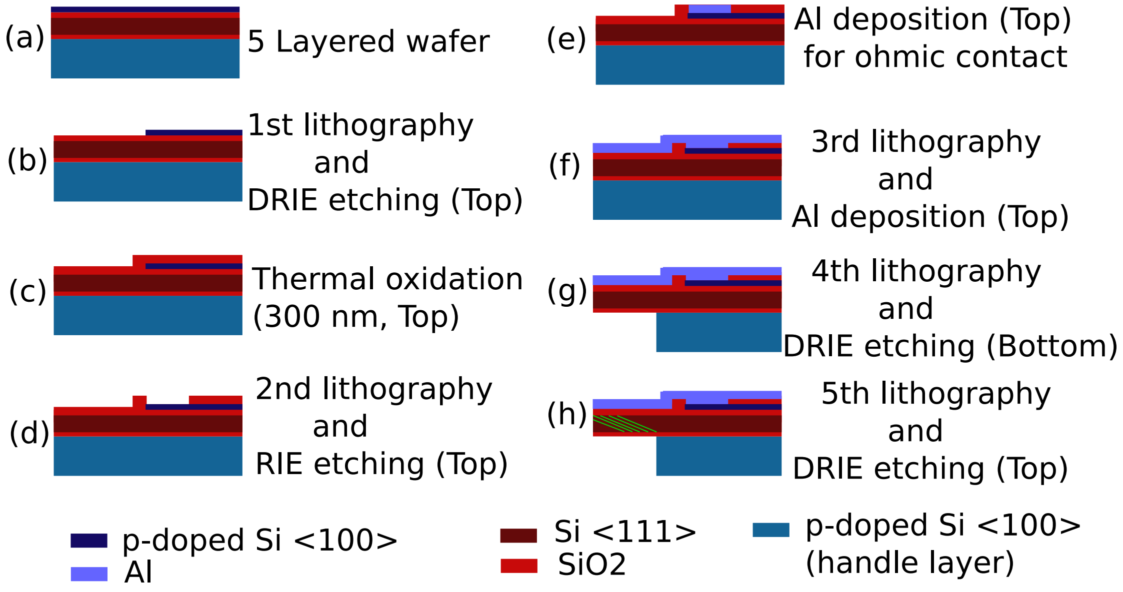

Figure IV.10 – Fabrication process of the cavalier

the top layer. The oxidized layered was then partly etched following a second round of lithography on the top surface and the RIE etching. This process was used to create an ohmic contact, which was made after deposition of Al on the etched zone. A third round of lithography was used on the top side for the deposition of Al to make the conduction around the ohmic contact previously made. The fourth lithography was then used on the bottom side followed by DRIE etching for the bottom side. Finally the last round of lithography was made for the mechanical handling part.

IV.5 ASSEMBLY PROCESS

In this section assembly strategy employed in order to develop a sensing tool from the fabricated components is discussed. The fabricated passive tool and cavalier are shown in Fig. IV.11. The entire process of assembly is divided into 6 steps (Fig. IV.12). In the Step 1, the one side of the mechanical handling part is removed. Thereafter, in the Step 2 the two cavaliers are glued in a sandwich configuration against the passive tool in a way that one side contains only one mechanical handling part. This step required extra attention, because the assembly of the cavalier has a direct impact on the behavior of the sensing tool. Therefore the cavaliers are properly positioned against the passive tool and finally fixed using an epoxy glue. The remaining mechanical handling parts then can be removed manually.

In the step 3, each electrodes around the gauges are electrically wired. The wiring on the electrodes are done using a conductive glue, the conductive glue need to properly cured under the defined standard condition from the manufacturer. It

(a) Fabricated passive tool (b) Fabricated cavalier

Figure IV.11 – Fabricated devices

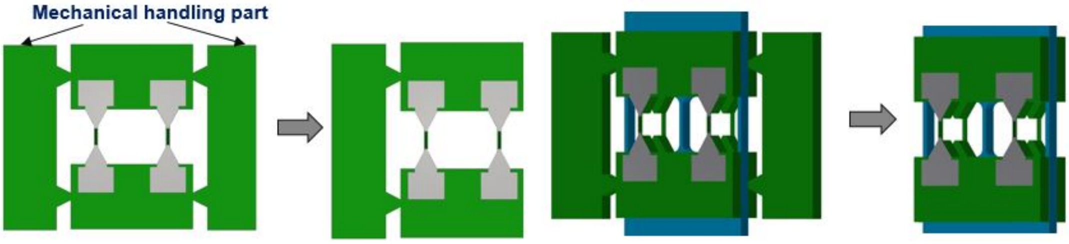

(a) Step 1, Removal of one side mechanical handling part (b) Step 2, Cavalier assembly on the passive beam followed by removal of remaining mechanical handling part

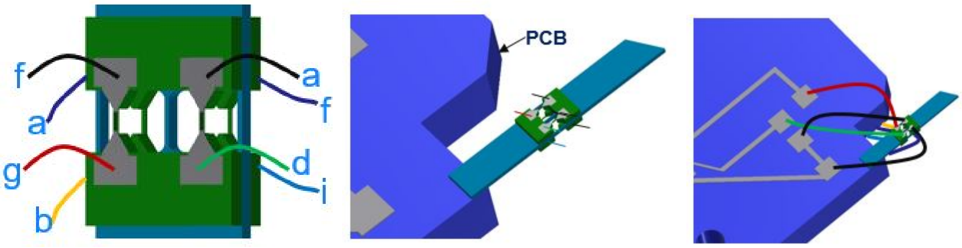

(c) Step 3, Wiring on the electrodes (d) Step 4, Assembly of the assembled tool on the PCB (e) Step 5, Wiring from the electrodes to the PCB

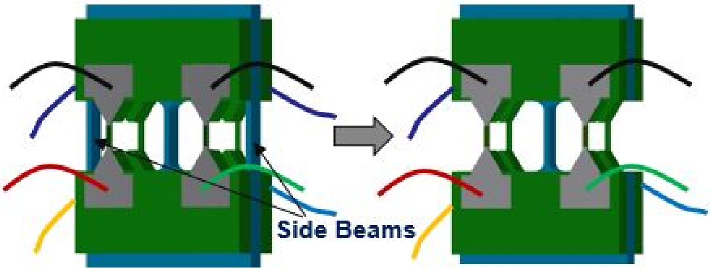

(f) Step 6, Removal of the side beams from the assembled tool

Figure IV.12 – Steps involved in the process of assembly and wiring is noticed that if the conductive glue is not cured well (timing and/or temperature of curing not respected) then the corresponding gauges may have unwanted resistance. Therefore, the wiring on the electrodes required a careful attention. The corresponding wiring is made in accordance with the discussed wheatstone bridge in Fig. IV.4, where the common point of R_2 and R_4 is marked as “a”, and that of R_1 and R_3 as “f”. The supply voltage V_{CC} would be provided across point “b”,“d” and “g”, “i” respectively for the bridge W_2, and W_1. This assembled tool is then glued on a PCB using an epoxy glue in step 4. After this, the wiring from the electrodes are transferred to the PCB in step 5, which then can be electrically connected to wheatstone circuitry as discussed in Fig. IV.4. The two extra side beams of the passive tool in the cavity part, then removed using a laser cutting process (step 6). The assembly of the cavalier with the passive tool, and the wiring involved on the electrodes of cavalier are done at the “Percipio Robotics”, who is an industrial partner in the COLAMIR project [COLAMIR 20].

IV.6 EXPERIMENTAL STUDIES

This section introduces the experimental setup, its working and discusses the realized tasks in terms of system performances. The constituent elements of the experimental setup is defined in the subsection IV.6.1. System behavior under no load (subsection IV.6.2), and the characterization for the load along Y (subsection IV.6.3) and Z axis (subsection IV.6.4), with a global discussion on the sensitivity and gauge factor is discussed (subsection IV.6.5).

IV.6.1 Experimental Setup

The experimental setup of the system is shown in Fig. IV.13. The experimental setup consists of a MCL Nano 3D-200, which is capable of positioning along 3 axes with nanometric resolution. The developed sensing tool is fixed on the positoning stage and is positioned to move against a reference force sensor. The reference force sensor employed for the tasks are Femtotools FT-S1000 and FT-S10000 respectively for resolution and long range validation (as in our knowledge there was no any commercially available force sensor which can meet both these requirements). Reference force sensor is fixed on a rotational axis, which is PI M116.DGH rotational axis from Physik Instrumente.

The experimental system configuration for the characterization along the two axes are shown in Fig. IV.13 as Configuration 1 and Configuration 2, respectively for Y and Z axis. Throughout the characterization process the performance was characterized for the applied load within 50 μm from the tip end along the length of Piezoresistive Tool (PRT).

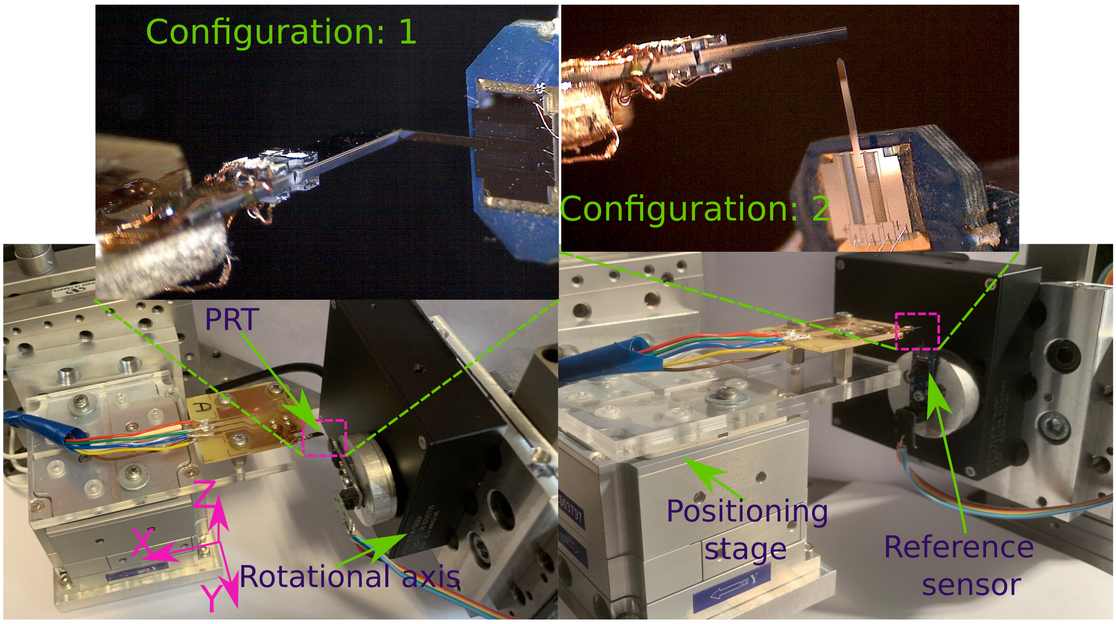

Figure IV.13 – Experimental setup

Resistors	Values (kΩ)
R_1	2.98
R_2	3.01
R_3	3.22
R_4	2.88

Table IV.3 – Measured resistance of gauges under no load

IV.6.2 Behavior under no load

The resistance property is sensitive to the environmental variations like temperature and humidity. In the presented case experiments were conducted in a closed room assuming very less influence on the resistance. To validate this argument output voltages of the wheatstone bridge circuitry were monitored under no load and it was observed that temperature and humidity are very stable related to the SNR of the signal acquired from the wheatstone circuitry.

With the measured voltage along the two axis as v_y and v_z (as defined in section IV.2.3), under no load the obtained system behavior is shown in Fig. IV.14.

Depending on the type of doping (p or n) and the doping concentration, the temperature coefficient (a parameter for resistance dependency on the temperature) can change as discussed in [norton 78]. The obtained performance Fig. IV.14, demonstrate a reasonably stable behavior within the sensed temperature noise level. The different resistances across the gauges under no load was measured

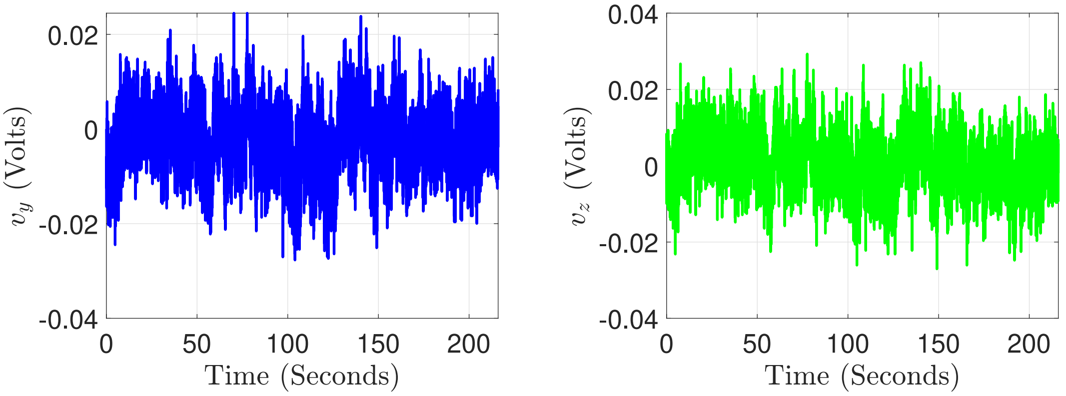

(a) Voltage signal, v_y (b) Voltage signal, v_z

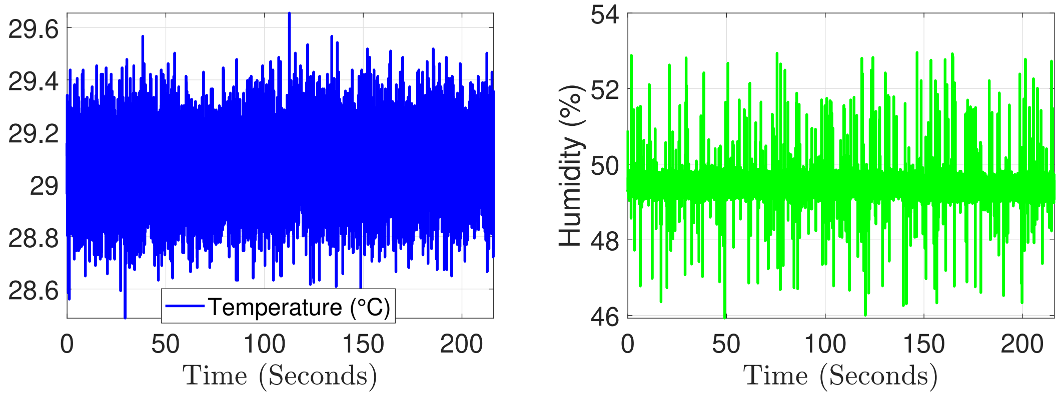

(c) Temperature in working environment (d) Humidity in working environment

Figure IV.14 – Signal acquisition under no load and the environmental conditions

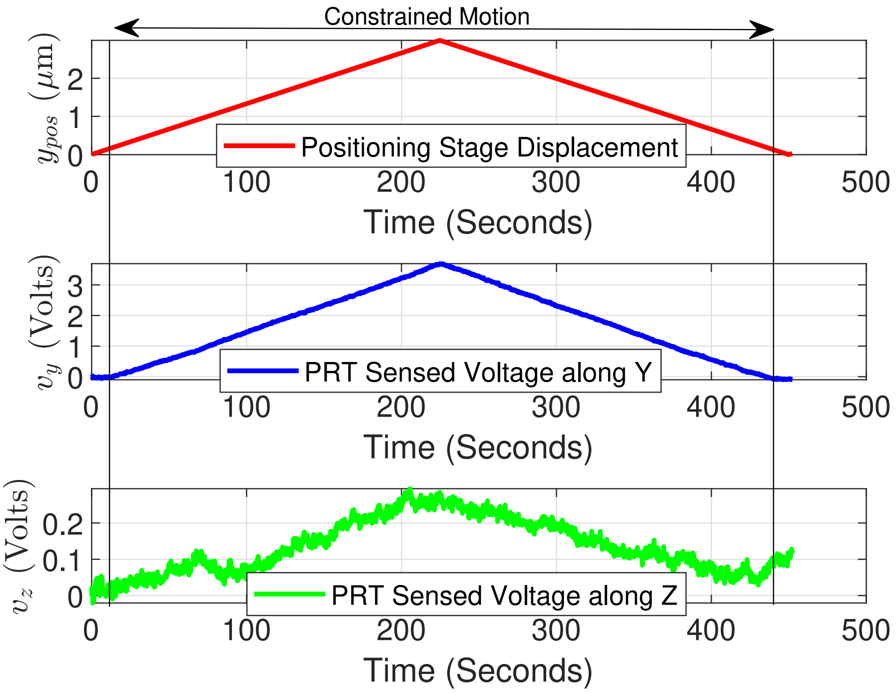

Figure IV.15 – Input displacement and sensed voltages from PRT against load along Y

(after the wiring and assembly) and listed in Table IV.3. This corresponding resistance change would lead to voltage changes in the circuitry, under the external load.

IV.6.3 Characterization for load along Y axis

In this section the different characterization works along the Y axis are discussed. In order to characterize the PRT along this axis, positioning stage was moved along the Y axis allowing a constrained motion of the PRT against the reference force sensor. The input displacement to the positioning stage along Y axis (y_{pos}) and the respective sensed voltages v_y, v_z along the two axes are shown in Fig. IV.15. The entire motion, consisted of constrained motion (as marked in Fig. IV.15), while remaining as free motion (unconstrained).

The applied constrained motion resulted into a voltage measurement of approximately 4 V along the intended characterization axis, whereas a voltage of approximately 0.3 V along the out of motion direction. The alignment of the reference force sensor (sensing axis) and the motion direction (of the positioning stage) was along Y axis and therefore the chances of the force component along Z is very less. To further minimize the obtained coupling behavior, a scaling factor is identified which is multiplied with the output of one of the wheatstone bridge

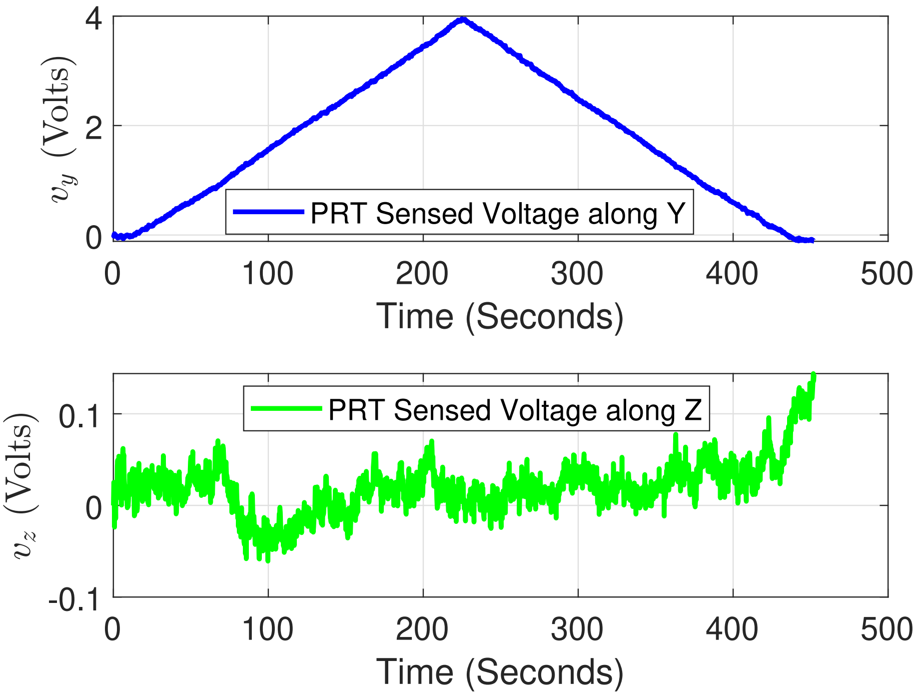

Figure IV.16 – Voltage signal after coupling correction (resulting from Fig. IV.15)

(lower in magnitude in out of motion direction), so that the two wheatstone bridges gives closest possible value ($v_{W1} \simeq v_{W2}$). In the present case a parameter k_v equals to 1.15 is identified to meet the mentioned requirements.

The obtained output for voltage proportional to strain along Y and Z are shown in Fig. IV.16, where it can be seen that the coupling extent is minimized typically to the noise level in the signal processed. From here onward the respective voltage change detection and the according calculations along the two axis would be after the correction of coupling.

IV.6.3.a Sensitivity and Stiffness Identification

The employed wheatstone bridge circuitry allows the measurement in terms of voltage under the application of any load, therefore there is need to find a factor which can map the voltage measured in terms of force measurement. This factor is the defined sensitivity for the studied sensor. Corresponding to the experimentation shown in Fig. IV.16, the force measurement from the reference force sensor (f_{ref}) against the sensed voltage (v_y) along the Y axis is shown in Fig. IV.17. An estimate of force is calculated using identified sensitivity of 2280 μN/V. The force measurement of 9 mN is presented in Fig. IV.17.

The force sensing PRT can also be used to estimate the displacement of the tip, to have this capability we need to identify the stiffness of the PRT. Such knowledge of stiffness allows to find the stiffness of the structure in contact and can also be used for various task handling capacity, for instance in manipulation against an

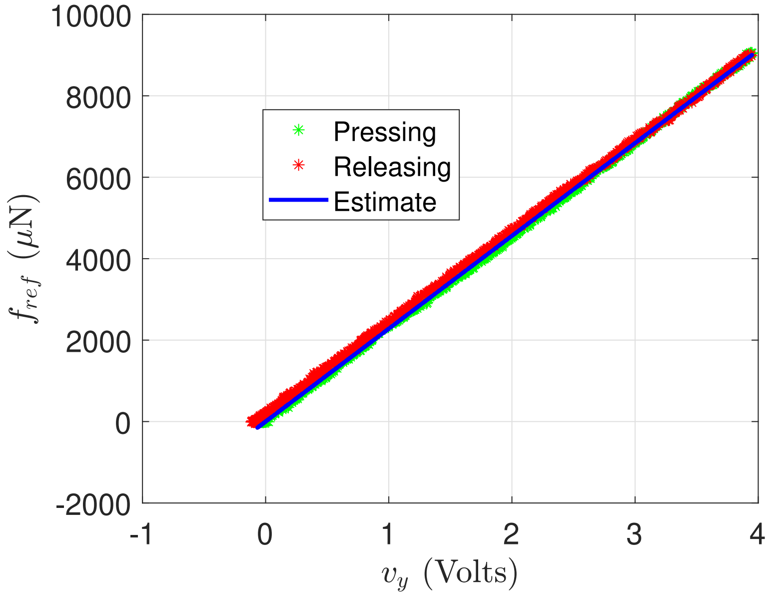

Figure IV.17 – Sensitivity identification of PRT along Y axis

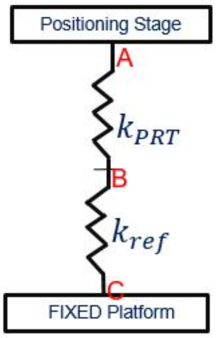

Figure IV.18 – Spring equivalence

unknown environment with a dedicated force/position control such as impedance control. For the stiffness identification, the employed experimental setup can be modeled into spring equivalence system assuming the static behavior of the system. The according spring equivalence system is shown in Fig. IV.18. The stiffness of the PRT in general is termed as k_{PRT}, whereas the reference force sensor's stiffness as k_{ref}.

For a reference force f_{ref}, reference force sensor stiffness k_{ref}, and positioning stage displacement along the characterization axis d_{pos}, the corresponding stiffness of Piezoresistive tool k_{PRT} can be given as in Eq. IV.13. Using Eq. IV.13, for the stiffness along y axis k_{YPRT} of the PRT, the corresponding positioning stage displacement is y_{pos} is replaced by d_{pos} , and k_{ref} by 8300 N/m (for the FT-S10000). This resulted into stiffness k_{YPRT} identified along the Y axis as 5130.3 N/m.

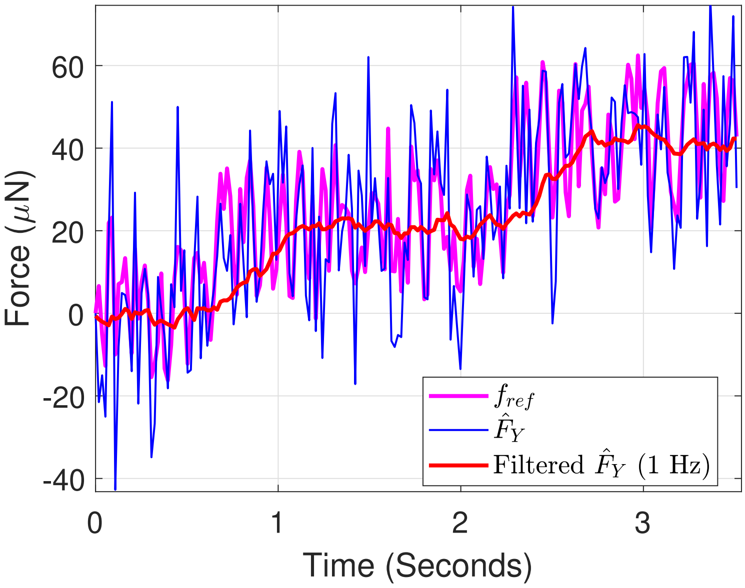

Figure IV.19 – Resolution study along the Y axis

$$k_{PRT} = \frac{f_{ref}}{d_{pos} - \frac{f_{ref}}{k_{ref}}} \tag{IV.13}$$

IV.6.3.b Resolution validation

The sensing resolution of the force sensor can be defined in terms of the percentage of the noise level obtained from the acquisition of the signal, but its good to demonstrate the system capability to detect the minimum change, the reference sensor used was FT-S1000. A staircase motion of 30 nm step was made from the positioning stage along the Y axis. Under the constrained motion, the respective sensed force from the reference force sensor and the sensed force from the PRT is shown in Fig. IV.19. The proposed PRT is able to detect the force change of 20 μN corresponding to the detection from the referenced force sensor.

IV.6.4 Characterization for load along Z axis

The characterization along the Z axis of the sensing tool was performed using the configuration 2 of Fig. IV.13. Same process was followed as done along the Y axis. The corresponding reference force, voltages, positioner displacement are used from the Fig IV.20. Validated force range along Z axis is 9.2 mN as shown in Fig. IV.20b. Table IV.4 summarizes the different potential parameters identified for the sensing along Y and Z axis.

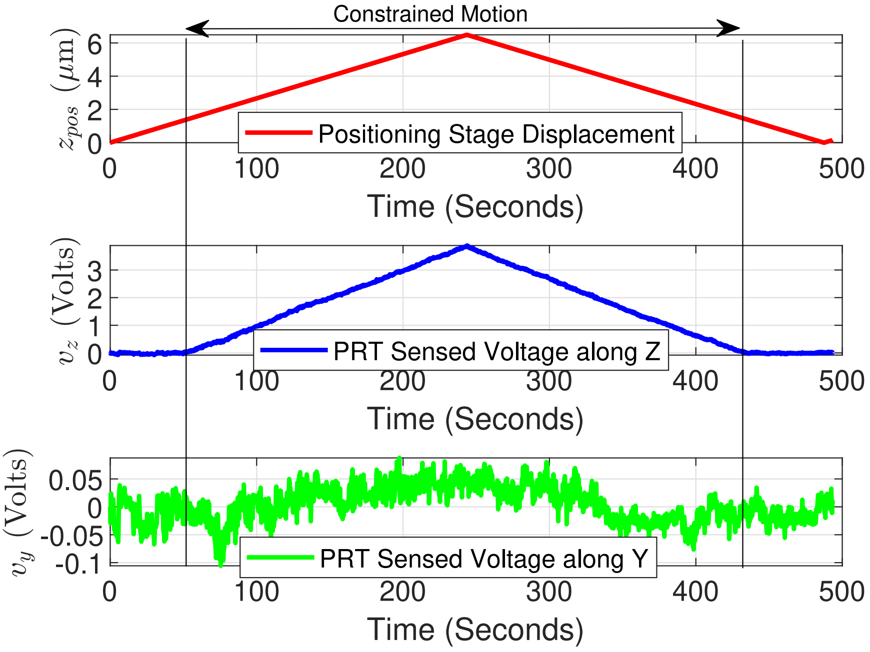

(a) Sensed voltages with constrained motion from positioner

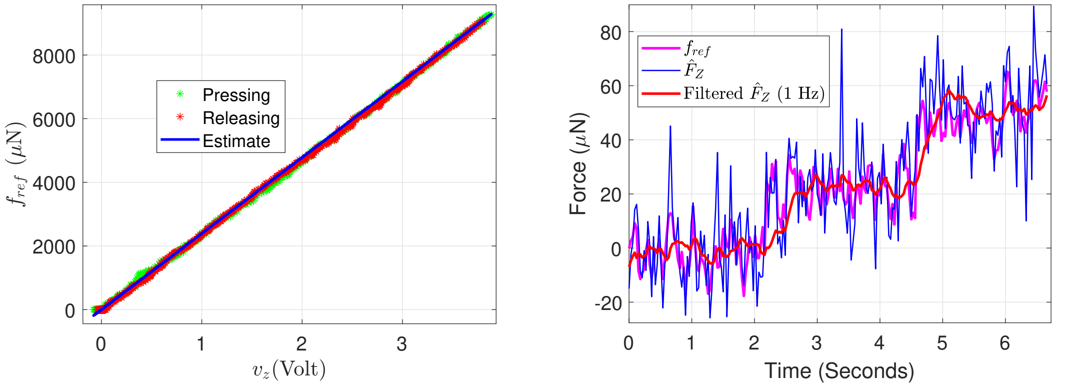

(b) Sensitivity Identification along Z axis (c) Resolution validation along Z axis

Figure IV.20 – Characterization along the Z axis

Parameters	Y	Z
Stiffness (N/m)	5130.3	2342.4
Sensitivity (μN/V)	2280	2390
Resolution (μN)	20	20
Standard Deviation (μN)	28	22

Table IV.4 – Identified parameters for characterization along Y and Z

IV.6.5 Gauge Factor and Sensitivity analysis

From Eq. IV.5, under unbalanced conditions, the respective diagonally opposite resistors undergo resistance change and this change can be approximated to be equal in magnitude (opposite in sign as defined in Fig. IV.1). This assumption conduct to simplify the Eq. IV.5 into Eq. IV.14.

$$v_{W1} = \frac{R_3 + \Delta R_3}{R_1 + R_3} V_{CC} A_G \quad \text{and} \quad v_{W2} = \frac{R_2 + \Delta R_2}{R_2 + R_4} V_{CC} A_G \tag{IV.14}$$

v_{W1}, and v_{W2} is measured from the wheatstone bridges, the input supply voltage V_{CC} is 5 V DC, amplifier gain A_G is 103, therefore the change in resistance in R_3 and R_2 can be calculated using Eq. IV.14. The calculated relative change in resistance is shown in Fig. IV.21, where r_3 is the actual piezoresistive resistance across the gauge R_3. The resistance change happens mainly in the piezoresistive gauges, whereas the total resistance measured contain also some component of non-piezoresistive resistance which might comes from the wiring around and/or the conductive glue used in the wiring. From various trials it was observed the resistance measured on a free cavalier without any wiring and the one measured at the end of final wiring, has an increment from 0.1 to 0.7 kΩ. Moreover this non-piezoresistive resistance can be considered approximately same for all the resistors measured (assuming similar wiring about the different gauges). For a non-piezoresistive resistance of 0.5 kΩ, the sensitivity improvement factor c_k obtained is 11 % and 7.3 % respectively along Y and Z axis (corresponding to the marked curve “Estimate” in Fig. IV.21a and Fig. IV.21b respectively). The calculated c_k comprised of hypothesis including an estimate of non-piezoresistive resistance, and its equal presence along all the gauges, which introduced certain degree of uncertainity in the calculation involved.

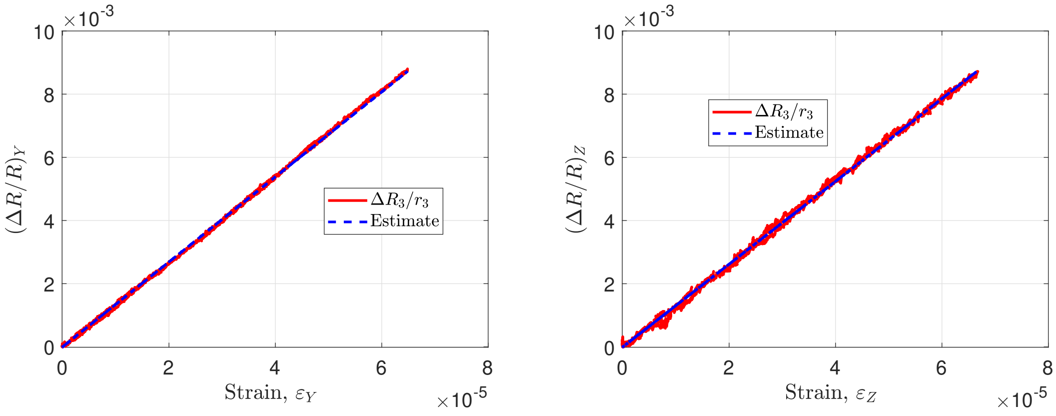

(a) For load along Y (corresponding to Fig. IV.16)

(b) For load along Z (corresponding to Fig. IV.20a)

Figure IV.21 – Relative resistance change against the strain

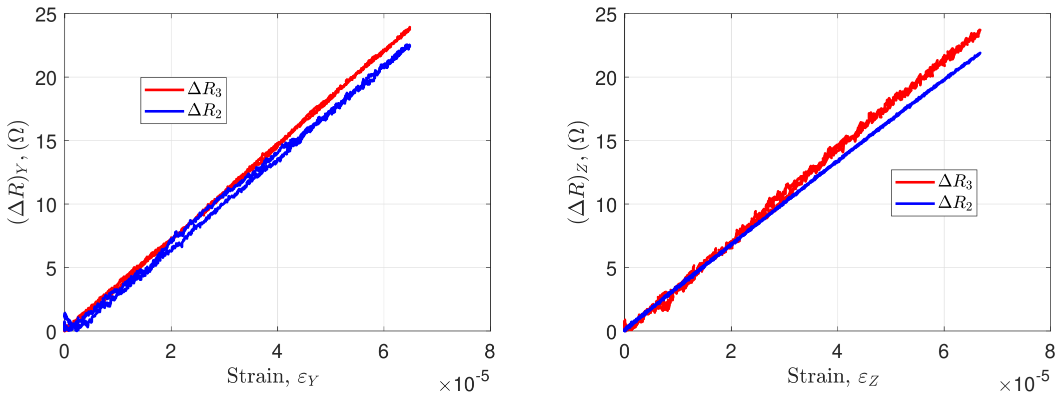

(a) R_3 and R_2 against load along Y (corresponding to Fig. IV.16)

(b) R_3 and R_2 against load along Z(corresponding to Fig. IV.20a)

Figure IV.22 – Absolute resistance change in the two wheatstone bridge against the load along Y and Z

The stress distribution in the proposed scheme may have several losses from the gluing of cavalier, and wiring around the gauges, which is not very obvious to include in the model. Moreover the expected ideal condition of decoupled sensing capability is not very realistic from the experimental side. The compression and elongation stress along a cross-section of cantilever should follow the same absolute change which may not be the situation experimentally (Fig. IV.22). R_2 and R_3 follows decrements for the load along Y, whereas in case of load along Z, R_2 follows the decrements, while R_3 has increments (as discussed in Table IV.1. In Fig. IV.22, the absolute changes are shown for R_2 and R_3, which are different in their amplitude.

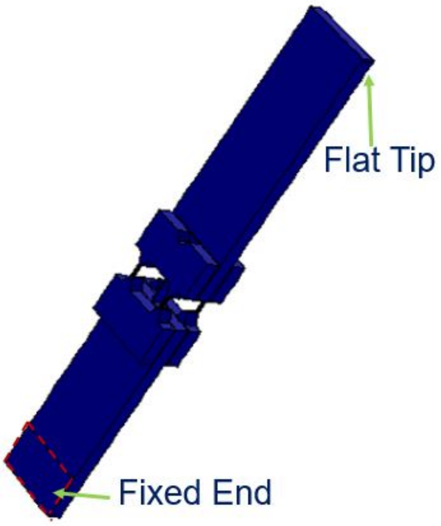

Figure IV.23 – A completely flat tip used for the analysis in COMSOL

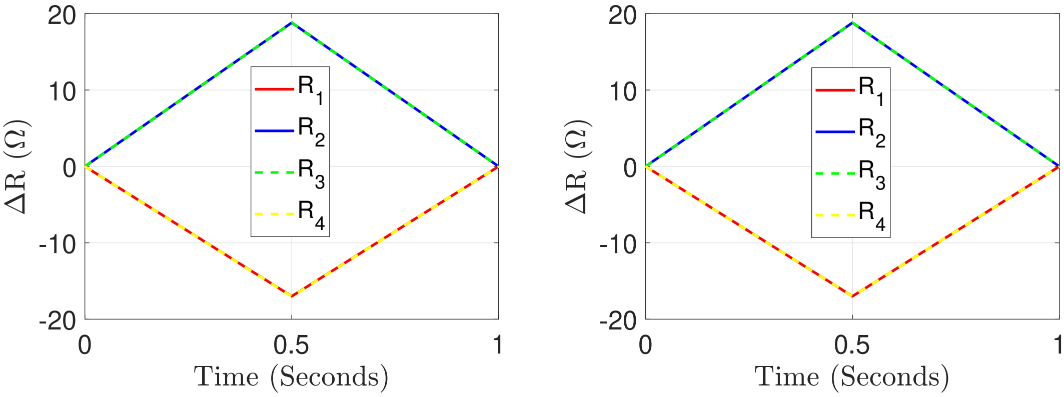

(a) Resistance changes for flat tip (b) Resistance changes for actual tip

Figure IV.24 – Resistance changes with load along Y axis

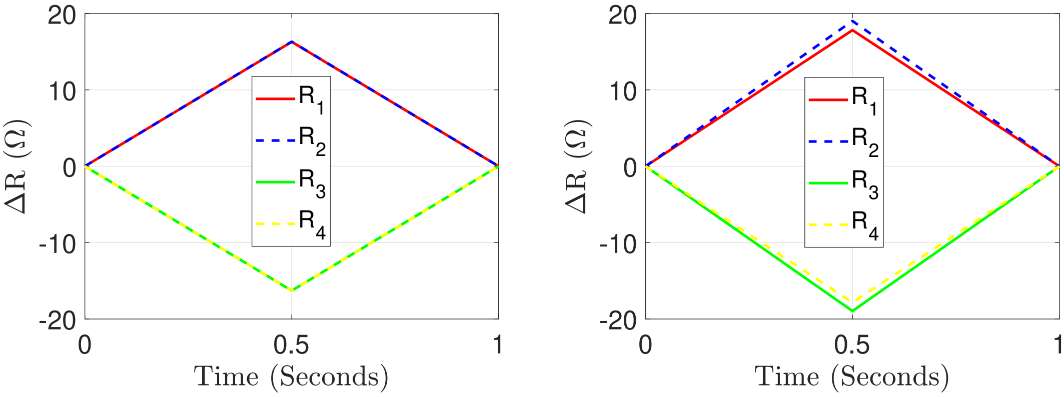

(a) Resistance changes for flat tip (b) Resistance changes for actual tip

Figure IV.25 – Resistance changes with load along Z axis

To further investigate the major reason for this different changes, one argument is the difference in compressive and tensile stress, while the second possible reason could be from the non-symmetric tool tip around the neutral axis. Both these possibilities are checked in a COMSOL simulation, the simulation result obtained for the actual tip has different change in absolute resistances under the influence of external load. In order to be sure that this change is coming from the difference in compressive-tensile stress, the same load was applied on a flat tip (Fig .IV.23). It was noted as shown in Fig. IV.24, for load along Y axis the corresponding change for flat (Fig. IV.24a) and actual tip (Fig. IV.24b) is same for corresponding resistors. Whereas when the load is applied along the Z axis (shown in Fig. IV.25), the corresponding change in resistance obtained for flat tip (Fig. IV.25a) and the actual tip (Fig. IV.25b) was found different. This means the geometrical non-symmetry of tip is making considerable influence for load along Z axis along with the influence compressive-tensile stress influence, which is not the case for load along Y alone. This makes sense as the stiffness along Y axis is much higher than that along Z, making the geometrical influence less pronounced along this axis. Overall in the context of the sensitivity of the proposed sensor, 3 main components are discussed. First component is the choice of material, which is discussed in section IV.2 with a study of different works done from the state of the art. The second component is the geometrical, which was discussed in terms of introduced cavity, dependency on moment of inertia, bending moment etc. The third component is the signal processing, for instance the choice of the differential amplifier which need to be chosen to scale the signal change to the detectable limit from the acquisition system while noise amplification must not affect the signal change detection. All, these three components were taken into consideration for the choice and requirements from the sensing.

IV.7 CONCLUSIONS

The proposed work introduced a novel multi-axis force sensing tool, which works on piezoresistive principle. The device development constitutes of a novel approach, with separate fabrication of cavalier and passive tool. Fabrication was made considering the versatile adaptability of the sensing device (cavalier of typical size 2.5 mm × 1.7 mm × 0.35 mm) with different passive structures, which can be designed based on the specific task requirements. A force sensing resolution of 20 μN over a range of 9 mN was experimentally demonstrated. The different electro-mechanical studies were made with the help of COMSOL multiphysics simulation. The sensitivity influence from design, choice of the material and the signal processing is also discussed. The two-axis sensing capability of the proposed sensing tool can be used in the development of an instrumented gripper, and according micro-scale task handling can also be demonstrated (which is discussed in the Chapter V).

Chapter V

Development of an Instrumented microgripper and micro-scale task handling

V.1 Introduction

The development of instrumentation at micro-scale and its according use for the study and micro-assembly, is the key objective of this thesis. Two instrumented micro-systems proposed and discussed so far, which includes a multi-axis force/torque sensing platform (Chapter III) and a 2 axis force sensing tool (Chapter IV). This chapter constitutes the use of the developed instrumented systems for some key micro-scale tasks handling like gripping and gluing. To fulfill the requirements of grasping and manipulation, an instrumented microgripper development is targeted in this chapter. This microgripper s developed using the multi-axis force sensing tool discussed in chapter IV as a sensing finger. There are potential requirements of gripper's tip position information, especially in the case of micro-assembly where positioning accuracy is of great importance. It is also seen in the chapter II, where for gluing extent estimation, the position of the gluing end was useful. Indeed, it was positional information which was used for the necessary force generation at the gluing end. The force information from the instrumentation can therefore be used to retrieve the position of the tip. If the knowledge of the dependent state (s), like driving input, external forces; allow the estimation of the tip position, then the external position sensors may not be required. In other word to avoid the use of the external position sensors, the gripper should comprise of the instrumentation which allows the knowledge of the necessary state(s) for the position estimation. Force sensing tool developed in chapter IV, allows the force information along the 2-axis, and therefore provided the driving input dependency over the actuation is convenient then the tip position of the gripper can be modeled. The instrumented microgripper development, modeling of the actuation and gripping tasks are discussed in section V.2. In chapter II, gluing study was done, which provided the gluing behavior analysis and a precise glued product using an active control. The studies made covered 1 axis, which was the axis densely influenced from the gluing process but indeed there is requirement to study the behavior along multi-axis. To address this issue, sensing platform developed in chapter III was used along with the use of the gripper developed in this chapter. Gluing with the developed instrumented systems is discussed in section V.3, where the corresponding force from gluing was measured along multi-axis.

V.2 Development of an instrumented microgripper

Towards development of an instrumented multi-axis microgripper from the developed sensing tool of Chapter IV, the primary requirement is to integrate the sensing tool with the precise multi-axis actuators (for multi DoF tasks). The actuation of any microgripper can be chosen from the different existing principles such as electrostatic [Alneamy 20], electromagnetic [Xie 19, Tisnes 20], electrothermal

[V.-Chable 19], vacuum [Ruggeri 18], pneumatic [Gursky 19], shape memory alloy [L.-Evans 20] or piezoelectric [Das 21]. One important point in the choice of the actuator is that the actuator should not interfere with the performance of sensing device integrated, therefore in the context of piezoresistive tool for sensing (PRT of Chapter IV); it is important to avoid external stimuli such as heating or optical based actuation. The requirement is also to avoid the need of any high input voltage (or additional amplifier) for actuation, by keeping a precise and long range positioning capability. The opening of gripper, sometime requires to generate additional force to get rid of contact forces, and therefore the actuation need to be compatible along both sides (±) of the respective axes. Piezoelectric actuators are known for their precise positioning, have the advantage of no electromagnetic radiation, good response with simple structure and are widely used in precise positioning applications [Deng 19, Chen 16, Deng 20]. In this work, piezoelectric multilayer actuators, are used for the development of gripper. These piezoelectric multilayer actuators can actuate with nanometric resolution up to ± 100 μm (range) along the two axis, corresponding to maximum input voltage of ± 20 Volts. Indeed a bimorph actuator, able to introduce a higher blocking force capability as compared to a multilayer stack piezoelectric actuator. But in our case, the sensing range of the integrated PRT (Chapter I), the according task handling force requirements are well within the blocking force of the employed piezoelectric actuator (> 10 mN). Choice of the piezoelectric multilayer actuator meets the compatibility with the developed sensing PRT and also with the requirement of micro-assembly. The piezoresistive tool (PRT) demonstrated in the previous chapter is integrated with 2 axis piezoelectric actuators, the assembled version is shown in Fig. V.1. The electronics including the circuitry for actuation and PRT which consists of wheatstone bridges (included in "Main PCB"), are developed on board with the gripper, where the "Intermediate PCB" is used mainly to allow a smooth transfer (closest to PRT, low noise) of electrical signals to the "Main PCB". The work including the PCB development, the compatible components packaging, and the main wiring with the PRT, is done at the Percipio Robotics (industrial partner in this COLAMIR [COLAMIR 20] project).

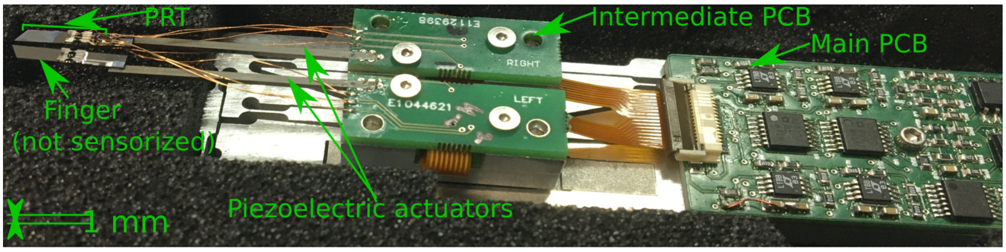

Figure V.1 – The instrumented microgripper after integration of the developed piezoresistive tool (PRT) from Chapter IV with actuators

The proposed gripper consists of a single finger instrumented (marked as PRT in Fig. V.1) for the sensing while the other finger is not wired for piezoresistive sensing and therefore used only for the actuation/gripping purpose. The piezoelectric actuators are fixed on an intermediate PCB and the electrical signals are then processed to the main PCB before the exchange of the signals with the host PC. In the following subsections the gripper actuation behavior is discussed.

V.2.1 Modeling of the gripper's actuation

The piezoelectric material exhibits the actuation based on the supplied input voltage, along with the non-linear properties from hysteresis and creep. There is requirement of gripper's tip position information in varieties of micro-manipulation tasks like making a force/position controlled grasping, release etc. In the absence of an external position sensor, modeling the actuation enables to provide an estimate of the gripper's tip position, in order to perform different tasks using gripper. A generalized schematic of the PRT containing finger of the gripper can be represented as Fig. V.2, where U is an input voltage for the actuation, f_{ext} is the external force applied on the gripper's tip. The according displacement δ of the actuator can be used to estimate the gripper's tip displacement δ_S with the use of the sensed force F_S, from the PRT. Also, an important consideration in this model is in the sensed force information which included the hypothesis that force would be only sensed if its on PRT tip, but indeed there would be influence of this force on δ and so on δ_S. Moreover, throughout different experimentation and analysis in this chapter, the forces are applied and considered only on the tip of the gripper (on end effector).

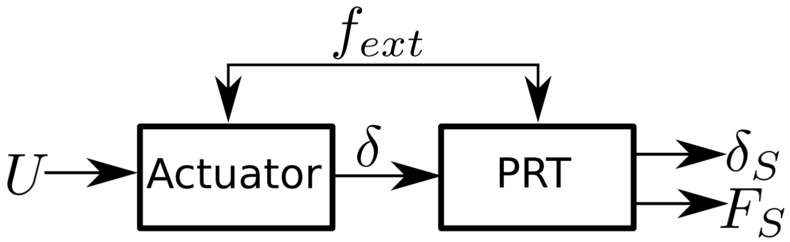

Figure V.2 – Block model of instrumented finger of the Gripper

In order to make a precise estimation of the actuator's displacement δ, it becomes important to include the non-linearity induced in terms of hysteresis and creep (can introduced > 20 % deviation from linear behavior). There are several studies done [Sabarianand 20] to compensate (allow < 10 % estimation error) the accordingly introduced positioning error from these non-linearity components. The hysteresis component can be modeled using Bouc-Wen (BW) modeling, because of the simplicity and the accuracy of estimation [Gan 19]. The other benefit of the BW modeling is possibility to cascade the external force/stress influence on the actuation without additional complexity. This modeling can be written as described in Eq V.2, where α, β, γ and ζ are the proportional parameters to the respective defined variables and can be identified using non-linear least square fitting of the model on the obtained behavior. Under static conditions, piezoelectric actuation contains three components, first a proportional to the input voltage component,

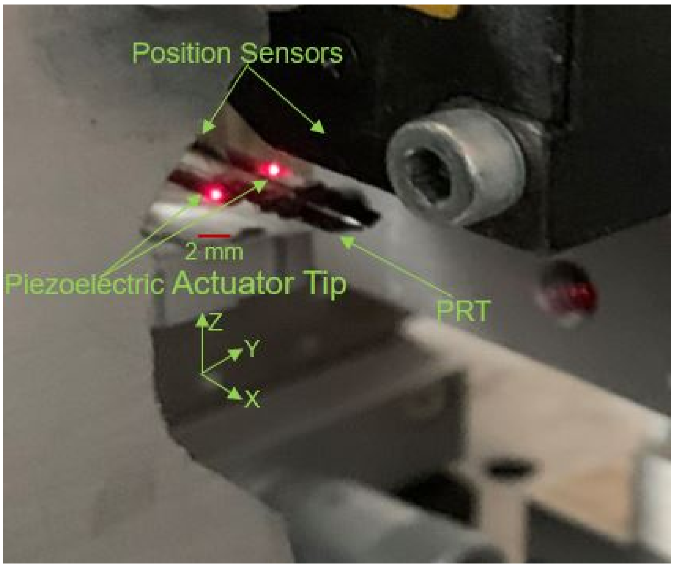

Figure V.3 – Experimental setup to study the characteristics of the gripper

second the hysteresis component, the third which is the external force component as written in Eq V.1 where for displacement δ, d_p is the proportionality constant to the input voltage U, H_s is the hysteresis component, and s_p is the proportionality constant to the external force sensed F_S.

$$\delta = d_p U - H_s - s_p F_S \tag{V.1}$$

$$\dot{H}_s = \alpha \dot{U} - \beta \mid \dot{U} \mid H_s - \gamma \dot{U} \mid H_s \mid + \zeta U sign(\dot{U}) \tag{V.2}$$

To facilitate an effective identification of the different parameters, the model identification is divided into two steps, first when there is actuation in free space (no influence of parameter s_p), while second when the actuation combines free space and constrained part together.

V.2.1.a Free space actuation

An experimental setup using position sensors (Keyence LC-2420) focused at the tip of the piezoelectric actuator is shown in Fig. V.3. With the applied input voltage the displacement of the actuators can be measured using the employed position sensors, and the PRT finger allows the measurement of the external force on the sensing finger of the gripper. The system behavior when there is no external load applied, allows the identification of the different parameters except s_p. The actuation δ along Y and Z is defined as δ_Y and δ_Z, whereas the corresponding input voltage U as u_Y and u_Z respectively. Coupling extent was found negligible between the two axis, and therefore to model the actuator's tip displacement δ_Y and δ_Z, separate studies are conducted with the u_Y and u_Z input across the corresponding electrodes (one axis actuation at a time).

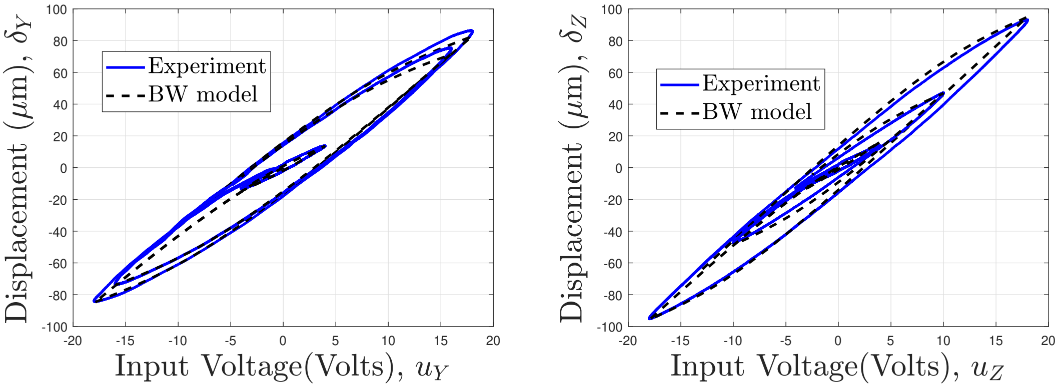

(a) Along Y, free space actuation (b) Along Z, free space actuation

Figure V.4 – Estimation and experimental results for actuation in free space

Actuator displacement along Y is shown in Fig. V.4a, which consists of 3 loops. These loops correspond to respectively sinusoidal input voltage of 18 V, 16 V and 4 V (frequency 100 Hz). Similarly for the actuation along the Z axis which is out of the gripping plane actuation, is shown in Fig. V.4b. The estimation error (in position) is within 10 % for all the cases. The identified parameters for the actuation along Y and Z axis are listed in Table V.1.

Parameters	Y axis	Z axis
α	2.56	2.5
β	0.085	0.12
γ	0.02	0.03
ζ	-1×10^{-5}	-1×10^{-5}
d_p (μm/V)	5.9	6
s_p (m/N)	-0.025	-0.032

Table V.1 – Identified parameters for the actuator

V.2.1.b Behavior in the presence of external load

A passive beam is placed close to the tip of the PRT, and a sinusoidal input voltage is applied to the actuator so that the corresponding motion includes both the free motion and the constrained motion. Under the constrained motion, the force introduced on the gripper is measured from the PRT and using Eq V.1, the parameter s_p is identified to fit the experimental and the estimation result from the model (respective force sensed along Y and Z are defined as F_{SY} and F_{SZ}). An experimental result corresponding to the actuation under free and constrained motion is shown in Fig. V.5, where a sinusoidal input voltage of 19 V is applied, as a result the gripper tool undergoes a constrained motion (marked as constrained motion). Fig. V.5a shows the hysteresis presence along Y, in the actuation along

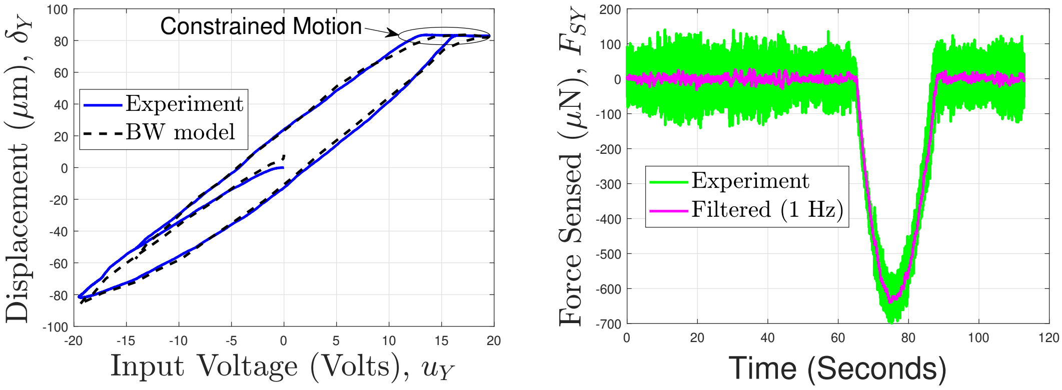

(a) Along Y, Actuation with Hysteresis (b) Along Y, force sensed from PRT

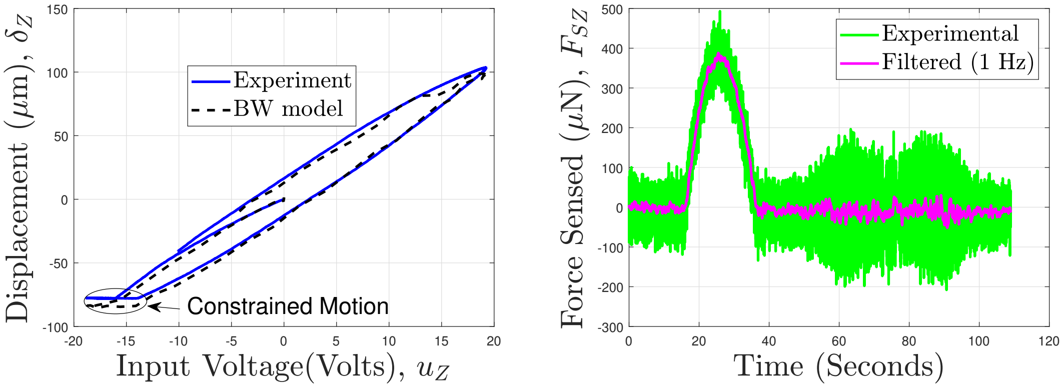

(c) Along Z, Actuation with Hysteresis (d) Along Z, force sensed from PRT

Figure V.5 – Estimation and experimental results combining the constraint motion with a constrained motion, the corresponding force sensed by PRT is shown in Fig. V.5b. Similarly, modeling and actuation obtained in free and constrained motion along Z axis is shown in Fig. V.5c. A table including all the parameters identified for the actuation estimation along Y and Z axis is listed in Table V.1. The defined actuation is the displacement of the piezoelectric actuator in the gripping plane, in order to estimate gripper tip position δ_S, the Eq. V.3, where L_s is the length of the free PRT (= 10 mm), θ is the bending angle of the piezoelectric actuator, k_{gs} is the stiffness of the sensing tool in the gripping plane.

$$\delta_S = \delta + L_s\theta - \frac{F_S}{k_{gs}} \tag{V.3}$$

The bending angle θ of the actuator can be approximated to be two times of the ratio of the deflection δ and the length L_A (= 25 mm) of the actuator (assuming circular curvature of the bend structure). Therefore, the gripper tip displacement can be estimated by knowing the δ, L_s, k_{gs} and the applied force F. Clearly the additional length of the PRT has scaled δ of the actuator's tip to δ_S as gripper's tip displacement. The spacing between the two fingers is about 780 μm, and this can be configured at the time of PRT assembly on the actuators based on the object size to manipulate.

V.2.2 Task Handling with the proposed Gripper

The proposed gripper with both fingers capable to perform 2 DoF actuation, and one finger instrumented with capability to sense force along the two axis, a wide variety of manipulation tasks can be done. Experimental setup with gripper integrated with additional linear positioning stages (2 Physik Instrumente PI M-122.2DD respectively along X and Z), with cameras (top view and side view) to perform grasping and release task of micro-object placed on a manipulation platform is shown in Fig. V.6a.

V.2.3 Grasping of micro-object without control

The grasping and the releasing of a micro-object (size 500 × 500 × 350 μm) is studied in this section. With the help of the positioning stages, the gripper is placed well around the micro-object which is placed on the platform (as shown in Fig. V.6b. Once from the camera (top view and side view camera as shown in Fig. V.6a), it is ensured that gripper is well positioned relative to the micro-object to grasp. Following which, a step-wise input voltage is supplied to the actuators (symmetrically) to follow a gripping motion (along Y axis) while monitoring the relative distance between the gripper and the object using the camera. Indeed the weight of the micro-object is negligible, but considering the surface forces little extra force of approximately 200 μN is applied in order to be sure about the safe grasping. The grasp of the micro-object is verified by making a motion of gripper in Z direction (using the positioner). Finally the gripper is allowed to go closer, to the manipulation platform and the actuator of the gripper is allowed to move step-wise

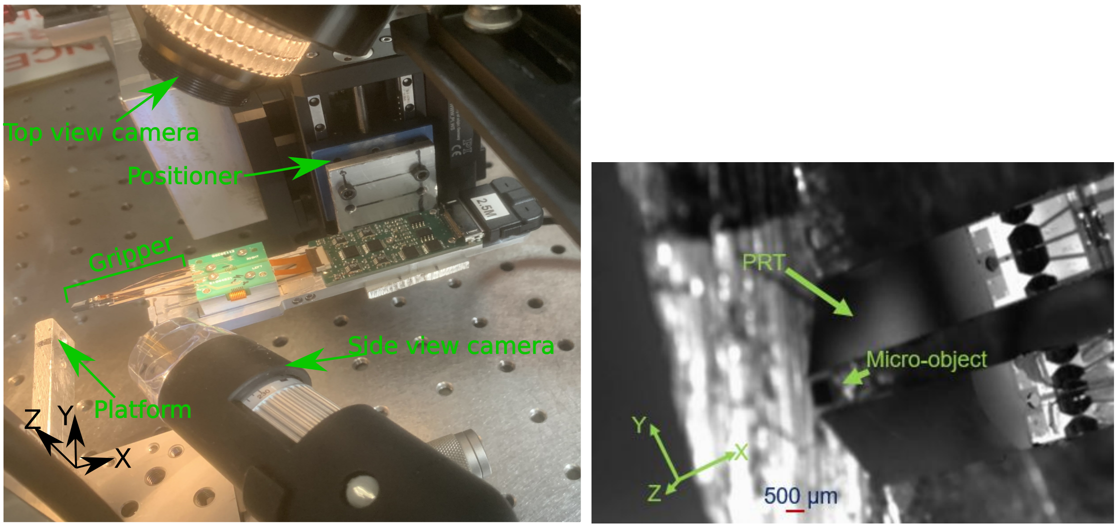

(a) Experimental Setup

(b) Gripper and micro-object

Figure V.6 – Experimental setup and the Gripper-object view

to release the micro-object on the platform. The duration for which the micro-object is grasped, marked as “Grasped” and that during the process of release as “Release” in Fig. V.7. Even following an open loop operation, with precise and high resolution actuation (from piezoelectric actuator) and the online knowledge of the tool interaction with object (Force sensing from PRT), it becomes possible for a safe grasp and release of fragile components. As, the system (instrumented microgripper) is capable to track online state of its end-effector (tip position and introduced force), therefore its possible to automate the grasp and release with a feedback control. To go ahead, a force controlled grasping and release is discussed in the next subsection.

V.2.4 Force controlled Grasping of a micro-object

With a defined reference force in the safe range, grasping and release of the micro-object can be done with inclusion of device safety. To demonstrate the grasping and release of the micro-object in a force controlled closed loop, a direct force controlled scheme is shown in Fig. V.8a. In this scheme finger of the gripper containing PRT is shown, where the actuation voltage u_Y is controlled based on the force sensed F_{SY} by PRT. The according actuation voltage control, allows the control of the actuator displacement δ_Y, and so the grippers tip displacement δ_{SY}. With the proposed control scheme, the stability of the grasped object is tested with inclusion of different instant, as defined in Table V.2. Controller with propotional gain $k_U = 5$, is turned ON and OFF at several stages during the process, to verify the grasped object hold and stability. The reference force f_{Yref} is defined as f_{YG} and f_{YR}, respectively for grasping and release. The microgripper system as a whole is integrated with a high range positioner from Physik Instrument (M-122.2DD), and this positioner position P_{GT}, is defined as P_W and P_G, respectively for "waiting

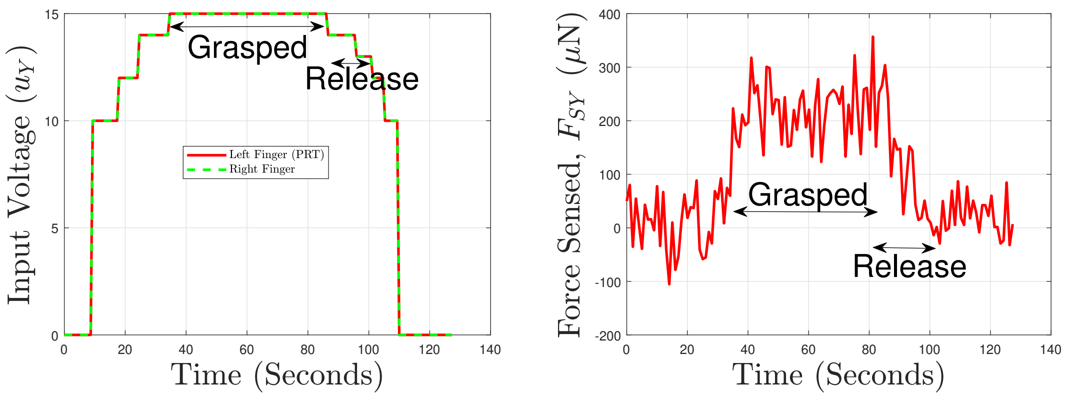

(a) Actuation input voltage to piezoelectric actuators

(b) Force sensed by PRT

Figure V.7 – Gripping of the micro-object without any feedback control

position" and "grasping position". In the current experiment, the positioner is used for actuation only along Z axis, in order to be sure about the grasped and release of the micro-object. The obtained behavior as result of actuation in free space and the sensed force is shown in Fig. V.8. The position of the positioner shown in Fig. V.8e, while the force tracking error is shown in Fig. V.8d, the tracking error is high in the beginning because of the two reasons, one the controller is OFF in the beginning, secondly after turning ON the controller gripper followed Free motion before coming into contact with the micro-object, as soon it comes in contact force tracking error starts decreasing to 0.

Instant	Controller	f_{Yref}	P_{GT}
A	OFF	f_{YG}	P_W
B	ON	f_{YG}	P_G
C	ON	f_{YG}	P_W
D	OFF	f_{YG}	P_W
E	OFF	f_{YG}	P_G
F	ON	f_{YG}	P_G
G	ON	f_{YR}	P_G
H	ON	f_{YR}	P_W
I	ON	f_{YR}	P_W

Table V.2 – Different steps during the gripping and release of micro-object

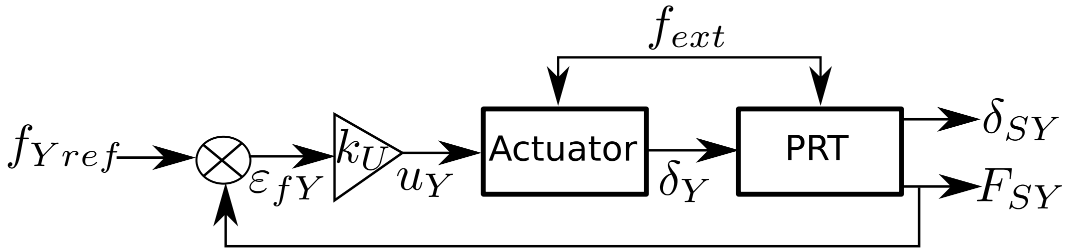

(a) Force controlled gripping and release scheme

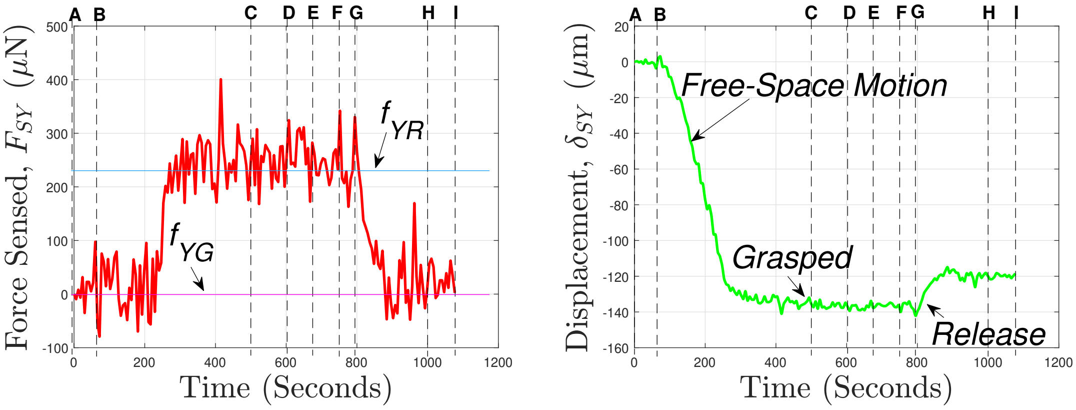

(b) Force sensed by PRT

(c) Displacement of PRT tip

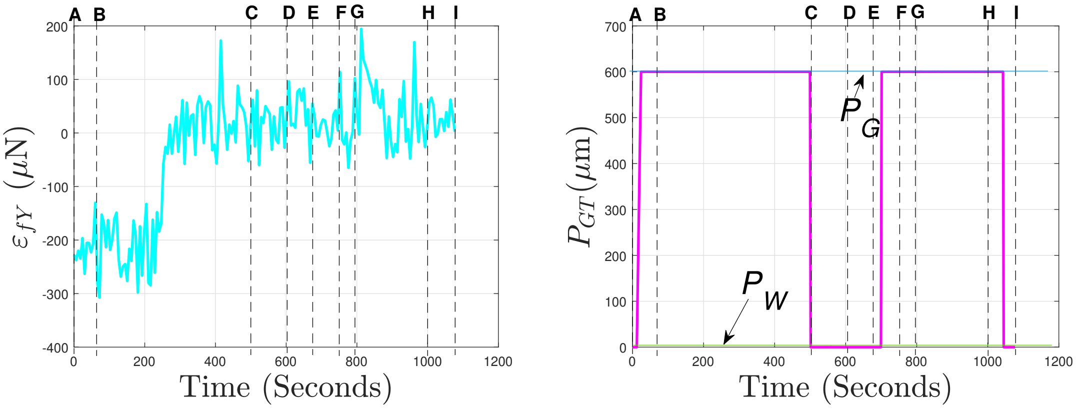

(d) Error in force tracking

(e) Position of the Positioner

Figure V.8 – Force controlled grasping and Release of the micro-object

V.3 ASSEMBLY USING THE DEVELOPED INSTRUMENTED MICRO-SYSTEMS

Combining the instrumented systems developed, a micro-manipulation system setup can be developed to carry-out varieties of tasks. A CAD view of such setup is shown in Fig. V.9a. The sensing platform discussed in chapter III is attached with a slab using thermal glue so as to replace the slab if needed by keeping sensing platform undisturbed. This slab can be used as a platform for the different task's study. For the purpose of micro-object manipulation, the instrumented microgripper is used. The system configuration shown in Fig. V.9a, can sense the 2 x 2D force and 1D Torque. This multi-state information provides a strong capability to the system to make decisions during different micro-scale tasks. For a long-range and multi-axis actuation requirement the instrumented gripper can be connected with 3D micro-positioning stages. The experimental setup corresponding to the discussed CAD design is shown in Fig. V.9b. The sensing platform employed with a glued slab is shown in Fig. V.9c, where the slab is glued with the face which is not encoded (while encoded side facing pattern monitoring camera). The face of the slab used for gluing in this chapter is marked in Fig. V.9c.

The setup described in Fig. V.9a and Fig. V.9b, is used to perform gluing task. As part of gluing process a 500 μm $\times$ 500 μm $\times$ 350 μm micro-object is used. It is glued on the slab (attached to the sensing platform). Micro-object is initially grasped from a platform closed to the presented setup, the grasping is made with a given reference force. Once the grasping is done, then the grasped micro-object is allowed to go in contact with UV-curable glue (VITRALIT 6128). The interaction between the micro-object base and the glue is made to form the glue meniscus, and this meniscus is then detached from the platform (where glue is placed), resulting into glue on the micro-object base. This glue deposited micro-object, is then allowed to go in contact with the slab which is attached to the sensing platform. Once, the glue-slab contact is established, then the UV light is turned "ON", in order to start the curing of the glue. The different steps employed throughout the process of gluing is shown in Fig. V.10. The starting phase of interaction between the glue-slab contact is marked as "P" (at 150 seconds), while that when the UV exposure is turned "ON" is marked as Q (at 220 seconds) in the measured forces (Fig. V.9d and Fig. V.9e, and Fig. V.9f).

Through the phase of glue contact with the slab, the presence of capillary force can be seen (between the point P and Q). This force has major influence along Z direction, which makes sense as the vertical motion is least blocked for motion as compared to planar direction (as more area of contact along planar face). When the UV exposure was turned ON, the curing resulted into stress development on the sensing platform and the object, the corresponding evolution of force on the platform is seen to follow a rapid increase in the beginning followed by some increase and decrease. This process is mainly because of the fact that the major glue shape change (from curing) happens in the very beginning (the polymerization of the boundary glue) followed by the strengthening of the glue link. During the

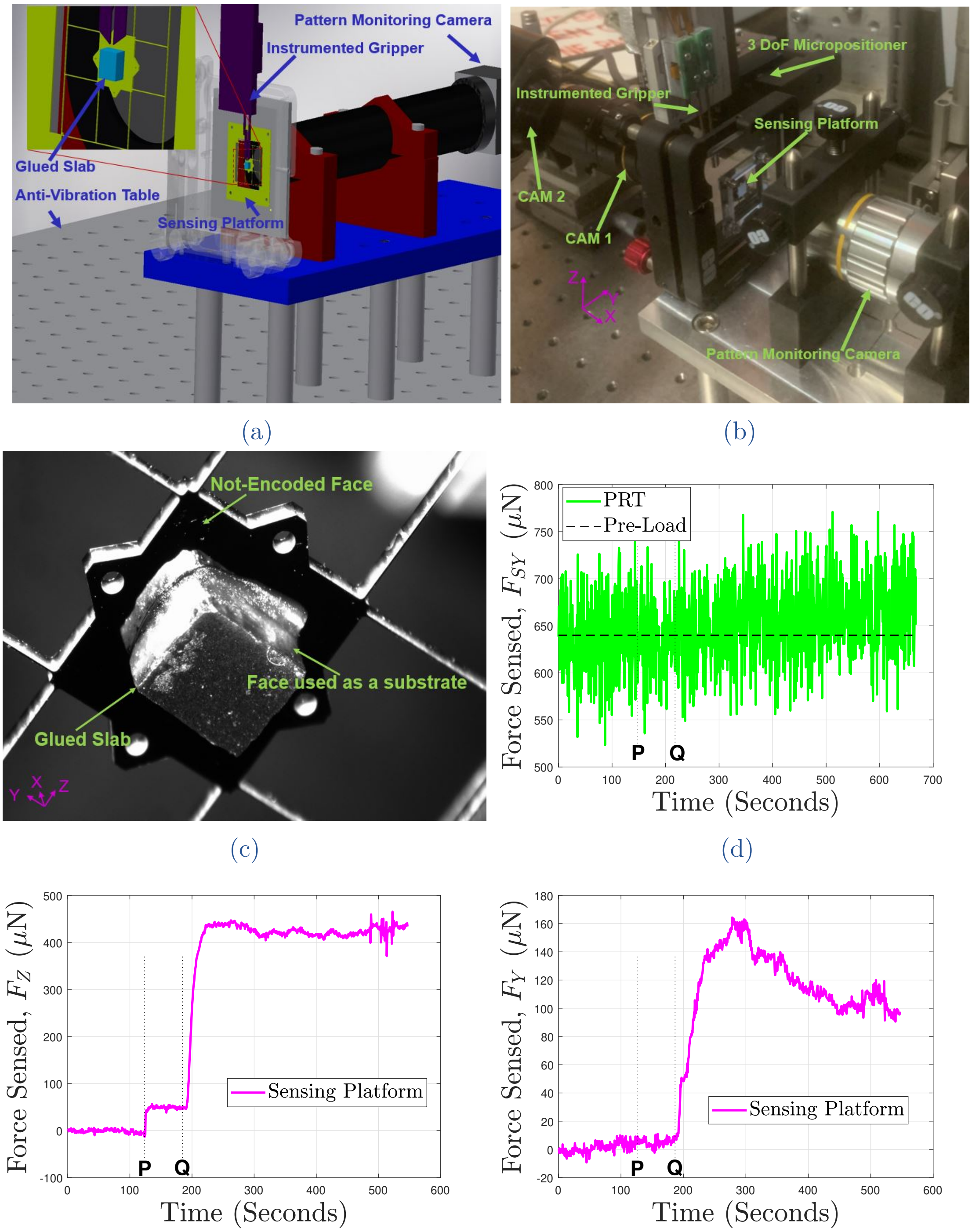

(a) (b) (c) (d) (e) (f)

Figure V.9 – Gluing with developed micro-systems; (a) CAD version of the gluing system; (b) Experimental Setup; (c) Sensing platform with Slab; (d) Force sensed by PRT along Y (P: glue-slab contact, Q: UV ON); (e) Force sensed by sensing platform along Z; (f) Force sensed by sensing platform along Y

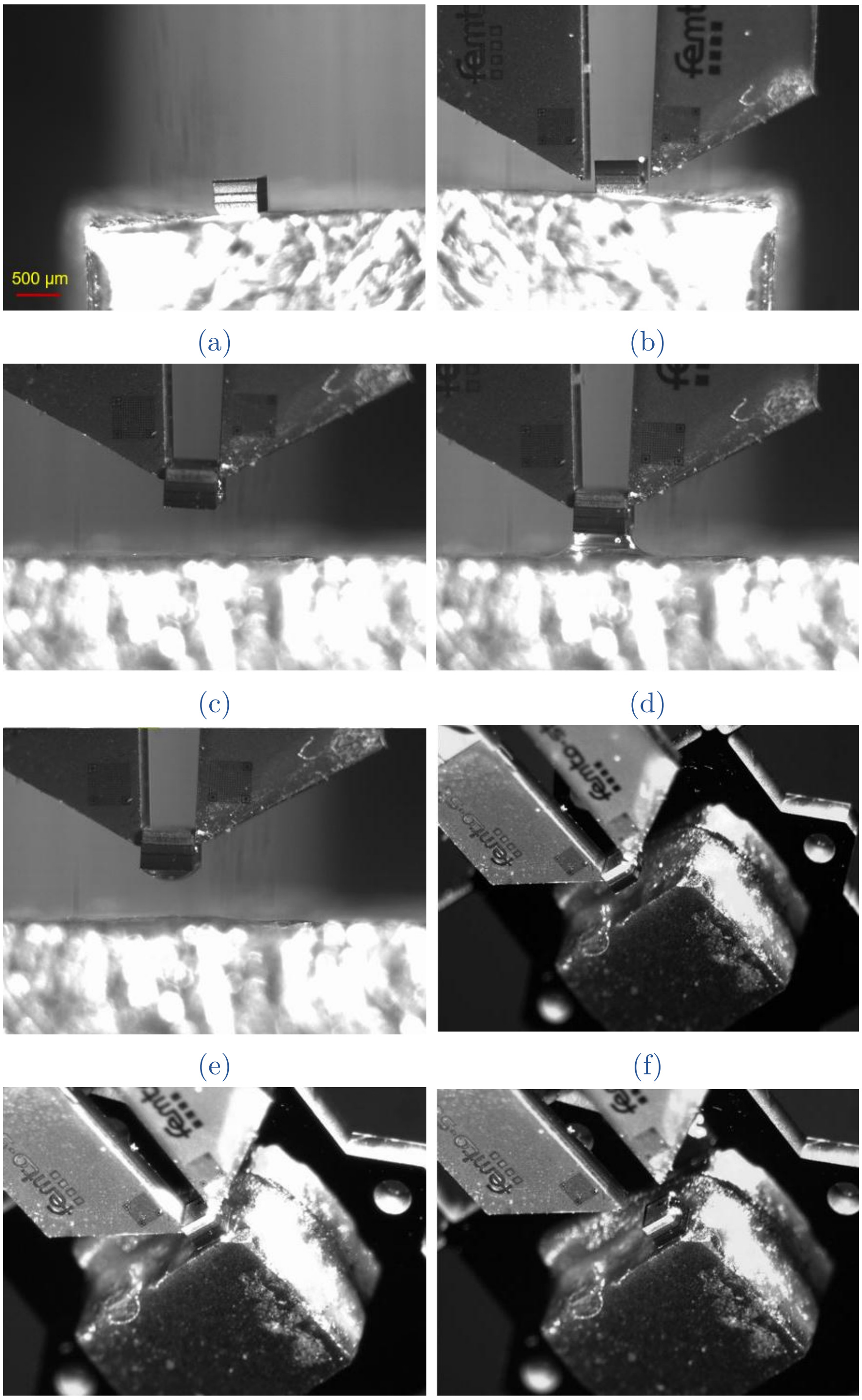

(a) (b) (c) (d) (e) (f) (g) (h)

Figure V.10 – Gluing process in different steps: (a) A 500 μm × 500 μm object on the support platform; (b) Gripper towards the object for grasping; (c) Grasped object; (d) Glue-Object contact for glue-deposition; (e) Deposited Glue at the base of the object; (f) Glue-deposited object towards the slab attached to sensing platform; (g) Object positioned on the slab, UV turned ON; (h) UV turned OFF, and object released (glued object on the slab) phase of the curing link building, it may follow some release of the residue stress coming from the initial shape change and the stress build around the structure. This is similar to what seen in the chapter II, where studies were made along the single axis. While during the phase of curing the micro-object is intended to remain least influenced by the curing effect, therefore the micro-object is grasped with much higher force than what actually needed (640 μN). A small change of 50 μN is seen in the sensed force along the gripping axis (Y axis) by the PRT (Fig. V.9d), while along the same axis the sensed force by the sensing platform is much higher (varied from 160 to 100 μN before stabilization). The signal noise level of PRT used in the current version of the gripper is much higher (100 μN) as compared to that measured from the sensing platform, and therefore the corresponding measurement by PRT is not as precise as that from the sensing platform. Also, there could be possibility of axial misalignment between the PRT sensing axis and the corresponding axis of sensing platform. Therefore, the difference in the measurement from the two systems is possible. In this version of PRT which is used in gripper has single wheatstone bridge for force sensing because of some problems in one of the gauges at very final stage of device installation, whereas in chapter IV, there were 2 bridges used and therefore we have double noise level in the gripper than the PRT along previously discussed. Therefore a further precise sensing is possible with a good version of the same gripping device discussed, secondly the difference in force sensing from the two instrumented systems can be minimized, by a careful alignment of their corresponding axes on the experimental platform.

V.4 CONCLUSIONS

A novel instrumented gripper development and its actuation modeling is studied. The obtained actuation estimation is within 10 %, in the case of static as well as dynamic. The developed microgripper is demonstrated with its use in micrograsping in open-loop and also in closed loop with a force controlled grasping and release. The obtained performances are closed to the acquisition noise of the system. Moreover, the developed gripper is used with the sensing platform developed in chapter III to investigate a gluing task. The sensing resolution of 2 μN of the sensing platform allows the glue-object contact detection and the corresponding introduced capillary forces along multi-axis (up to about 50 μ N in the presented study). The force sensed as result of curing is measured about 400 μN and 100 μN). A long range sensing capability of the sensing platform (up to 110 mN) can be used to sense the curing force for wide range of glue quantity and gluing area. The gluing task performed is in open loop but it brings the interest of developed system's use to perform a precise gluing task along multi-axis. The obtained behavior from the sensed forces followed the typical S-shaped trajectory which is in accordance with the studies in chapter II, and therefore the precise gluing with an active control can be extended along multi-axis. As a future work, the proposed instrumented gripper can be used to perform varieties of complex tasks in partially and/or fully automated mode.

Conclusions and perspectives

This thesis presented a study of different micro-systems, their instrumentation and the potential applications. As part of the COLAMIR project, this thesis targeted the study and instrumented systems development for micro-assembly (in industrial context). The robotization of assembly process is an important need in the industry as it enables a cost effective mass production with repeatable performance. Gluing of the surfaces, is a very common approach of the assembly in the industry. But, being a widespread requirement, gluing is mostly done manually. At the micro-scale the gluing behavior is affected by several parameters, during the phase from liquid glue capillary influence to stress developed during curing. This brings high uncertainty in the final positioning of the glued product. Therefore, in this thesis work gluing for micro-assembly is studied, the according challenges and approach towards precise gluing is discussed in Chapter II. It was found that curing alone can generate force of 200 μN across a gluing area of 500 μm × 500 μm, but still this amplitude can't be quantified because of its dependency over different parameters such as glue quantity, choice of the glue and several others. A study of external load based dependency over the positioning enabled the use of an active control for a precise gluing. With this use, positioning accuracy of ~ 0.2 μm is demonstrated for the glued product. The studies in this chapter also suggested the requirement of multi-axis instrumentation to extend the approach adapted for a precise gluing along multi-axis. To follow up the assembly requirements, there are several key challenges possible (in addition to the observation from gluing) such as; interaction with an unknown/variable environment, structural studies etc. Modeling of the system alone is not sufficient to address these issues, and there are potential requirements of multi-axis instrumentation with which local state(s) information can be retrieved. To address these requirements, this thesis targeted the multi-axis instrumentation development and proposed 2 sensors and one instrumented microgripper. First sensor (sensing platform discussed in chapter III) is based on vision principle while the other using piezoresistive (piezoresistive tool discussed in chapter IV). The proposed vision sensor of chapter III can sense the forces along the two planar axis and torque about the normal axis to the force-sensing plane. This sensor employed a dedicated encoding strategy which enabled planar position sensing over a long range. The vision sensor was demonstrated with a multi-axis force sensing with high range to resolution ratio of 55000. This sensor demonstrated to sense the force from 2 μN to 110 mN along the two axis. The corresponding work included a novel methodology of modeling for force–torque estimation along with non-linear force-displacement evolution. Task like gluing, where the extent of forces exerted (on the surfaces) is dependent on the several parameters (like glue quantity, size, shape with the gluing surfaces); in such cases this sensor with high range to resolution enables the sensing from capillary interaction to the cured phase for a versatile choice over the gluing parameters. Moreover, this sensor is equally useful for multi-axis mechanical characterization of a wide varieties of structures such as natural/artificial fibers, MEMS devices, etc. Also, the interest of this multi-axis instrumented system extends to the development of other instrumentation (calibration process). Therefore the developed instrumentation is significantly useful for various applications. The second instrumentation, which is piezoresistive sensing tool (chapter IV) demonstrated with a sensing capability from 20 μN to 9 mN, along the two axis. This sensor can be easily integrated with actuators to perform different studies, and are very useful when the sensing frame need to move in a very confined workspace. The demonstrated sensing tool was mainly designed for its use to develop an instrumented gripper, but one key advantage of this device development constitutes separate fabrication of the sensing part, and passive part. Therefore, different sizes and shapes of passive tool can be separately fabricated based on specific task requirements and can be assembled with the proposed sensing part. This would lead to wide range of sensing possibilities, as the performance in terms of the range, resolution are dependent on the geometrical and mechanical parameters of the passive tool. This work therefore, opens up the possibilities to tune up different parameters for any specific application.

The demonstrated piezoresistive sensing tool was further integrated with a 2-axis piezoelectric actuators to develop an instrumented microgripper (chapter V). Modeling of the actuation of the instrumented gripper with inclusion of the hysteresis and external force is discussed with an estimation error less than 10 %. The developed gripper is demonstrated with grasping and release of a micro-object, making an open loop and a feedback controlled task. The obtained performances were within the signal noise level. The developed microgripper was also used for the multi-axis gluing study with its combined use with the sensing platform. The corresponding study from multi-axis gluing brings the interest of using an active control for a precise gluing along multi-axis. Moreover, the developed instrumented devices can be used to perform varieties of complex tasks, including 6-DoF precise gluing, insertion, rotation etc. Especially, for gluing and insertion (varying environment), use of impedance control can provide interesting results and therefore need to be demonstrated in the near future.

In terms of the device improvement for the microgripper developed, an adaptation of the variable stiffness mechanism in the sensing tool can bring interesting flexibility. Indeed there are several works which demonstrated the possibility of the use of the variable stiffness gripper such as using jamming technique [Yokouchif 20], [Jiang 19]. The gripper can also be tuned magnetically for variable stiffness such as in [Memar 19] (Fig V.11) which enhanced manipulation safety and robustness during collisions. A variable stiffness capability of the gripper allows to play with different sensing range and resolution without changing the tool. The MEMS devices such as [Cailliez 18], demonstrated variable stiffness sensing for a nN resolution over a measurement range of ± 2.45 µN. The interest of such sensing is in the characterization of mechanical structures, where for the distance (<20 nm) between the sensor and the structure, intramolecular force follows variable gradi-

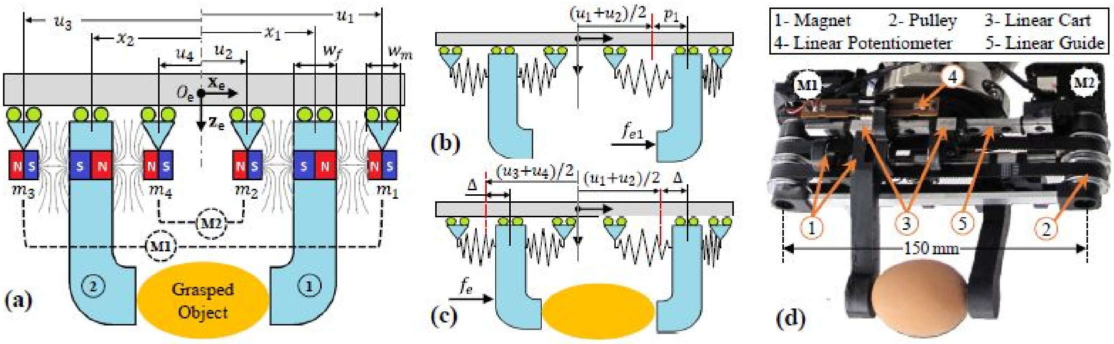

Figure V.11 – A variable stiffness used in [Memar 19] (a) gripper schematic (b) Fingers passive motion before grasp denoted by p_1 (c) Fingers passive motion after grasp denoted by Δ. Equilibrium points in the absence of external forces are denoted by dotted lines in red (d) Different components of the gripper and mechanical design

ant which leads to instability regions. With the use of variable stiffness sensing, the dynamic requirement can be fulfilled and irregularities from instability regions can be avoided. Moreover, microgripper can be also be improved in terms of its communication to the host PC, mainly a wireless communication mechanism can be introduced to minimize the number of wiring around the device. This work can be seen also as a development of a microgripper towards a non-fixed end actuation like using spider micro-systems [Yanagida 17] or micro-aerial systems [Estrada 18]. With such a mechanism, a wide variety of work-space requirements may be achieved. Even it brings several challenges but it would allow the extension of the micro-manipulation in a very broader context. A wireless communication can enhance the system capability to minimize the requirement of large numbers of actuators around, and can enhance the acceptability of the system to perform micro-manipulation and assembly in large range of applications. There is potential scope of such systems not only in assembly but in medical and defense operations.

Bibliography

[Adam 19] G. Adam & D. J. Cappelleri. *Design of a 3d vision-based micro-force sensing probe.* IEEE MARSS' 19 proceeding, 2019.

[Al-Shareef 95] K. J. H. Al-Shareef, J. A. Brandon & A. J. Griffiths. *A simplified technique for the analysis of multi-stepped beams.* Proceedings of the Institution of Mechanical Engineers, Part C: Journal of Mechanical Engineering Science, 1995.

[Alapan 19] Y. Alapan, O. Yasa, B. Yigit, I. C. Yasa, P. Erkoc & M. Sitti. *Microrobotics and Microorganisms: Biohybrid Autonomous Cellular Robots.* Annual Review of Control, Robotics, and Autonomous Systems, vol. 2, pages 205–230, 2019.

[Alneamy 20] A. M. Alneamy, M. E. Khater, A. K. A.-Aziz, G. R. Heppler & E. M. A.-Rahman. *Electrostatic arch micro-tweezers.* Elsevier, International Journal of Non-Linear Mechanics, vol. 118, 2020.

[André 20a] A. N. André, P. Sandoz, B. Mauzé, M. Jacquot & G. J. Laurent. *Robust phase-based decoding of absolute (X, Y, θ) positioning by vision.* IEEE Transactions on Instrumentation and Measurement, 2020.

[André 20b] A. N. André, P. Sandoz, B. Mauzé, M. Jacquot & G. J. Laurent. *Sensing One Nanometer over Ten Centimeters: A Micro-Encoded Target for Visual In-Plane Position Measurement.* IEEE/ASME Transactions on Mechatronics, vol. 25, no. 3, pages 1193–1201, 2020.

[Bettahar 17] H. Bettahar, A. Caspar, C. Clévy, N. Courjal & P. Lutz. *Photo-Robotic Positioning for Integrated Optics.* IEEE Robotics and Automation Letters, vol. 2, no. 1, page 217–222, 2017.

[Beyeler 09] F. Beyeler, S. Muntwyler & B. J. Nelson. *A Six-Axis MEMS Force–Torque Sensor With Micro-Newton and Nano-Newtonmeter Resolution.* Journal of Microelectromechanical Systems, vol. 18, no. 2, 2009.

[Billot 15] M. Billot, X. Xu, J. Agnus, E. Piat & P. Stempflé. *Multi-axis MEMS force sensor for measuring friction components involved in dexterous micromanipulation: Design and optimization.* Inderscience, International Journal of Nanomanufacturing, vol. 11, pages 161–184, 2015.

[Budday 17] S. Budday, G. Sommer, C. Birkl, C. Langkammer, J. Haybaeck, J. Kohnert, M. Bauer, F. Paulsen, P. Steinmann, E. Kuhl & G. A. Holzapfel. *Mechanical characterization of human brain tissue.* Elsevier, Acta Biomaterialia, vol. 48, pages 319–340, 2017.

[Cailliez 18] J. Cailliez, M. Boudaoud, A. M. Ousaid, A. W.-Duflos, S. Haliyo & S. Régnier. *Modeling and Experimental Characterization of an Active MEMS Based Force Sensor.* International Conference on Manipulation, Automation and Robotics at Small Scales, Japan, 2018.

[Chang 10] R. J. Chang & C. C. Chen. *Using Microgripper in Development of Automatic Adhesive Glue Transferring and Binding Microassembly System.* Engineering, vol. 2, no. 1, pages 1–11, 2010.

[Chang 16] R.-J. Chang & J.-C. Jau. *Augmented Reality in Peg-in-Hole Microassembly Operations.* International Journal of Automation Technology, 2016.

[Chang 17] B. Chang, M. Koverola, Z. Ge & Q. Zhou. *Hybrid Microassembly combining Laser Die Transfer and Capillary Self-alignment.* International Conference on Manipulation, Automation and Robotics at Small Scales, 2017.

[Chen 16] X. Chen, C.-Y. Su, Z. Li & F. Yang. *Design of Implementable Adaptive Control for Micro/Nano Positioning System Driven by Piezoelectric Actuator.* IEEE Transactions on Industrial Electronics, vol. 63, no. 10, pages 6471–6481, 2016.

[Chen 19] P. C. Chen, K. Gadepalli, R. MacDonald, S. K. Y. Liu, K. Nagpal, T. Kohlberger, J. Dean, G. S. Corrado, J. D. Hipp, C. H. Mermel & M. C. Stumpe. *An augmented reality microscope with real-time artificial intelligence integration for cancer diagnosis.* Nature Medicine, vol. 25, no. 3, 2019.

[CITHADEL 19] CITHADEL. *CITHADEL project.* `https://www.ens2m.fr/fr/projet-cithadel`, 2019.

[Clévy 19] C. Clévy, B. Sauvet, J.-Y. Rauch, O. Lehmann, F. Marionnet, P. Lutz, L. Beccacece, S. Xavier, R. Aubry, A. Ziaei, C. Prévot & G. J. Laurent. *In-situ Versatile Characterization of Carbon NanoTubes using Nanorobotics.* IEEE, International Conference on Manipulation, Automation and Robotics at Small Scales, 2019.

[Cognard. 10] J. Y. Cognard., R. Creac'hcadec, L. Sohier & D. Leguillon. *Influence of adhesive thickness on the behaviour of bonded assemblies under shear loadings using a modified TAST fixture.* Springer, vol. 30, pages 257–266, 2010.

[COLAMIR 20] COLAMIR. *COLAMIR ANR Project.* https://projects.femto-st.fr/colamir/en/sample-page, 2020.

[Cui 18] S. Cui, X. N. Guan, E. Ghantous, J. J. Vajo, M. Lucas, M. S. Hsiao, L. F. Drummy, J. Collins, A. Juhl, C. S. Roper, & A. F. Gross. *Aqueous Assembly of Oxide and Fluoride Nanoparticles into 3D Microassemblies.* Langmuir, vol. 34, no. 27, pages 8075–8080, 2018.

[da Silva 11] L. F. M. da Silva, A. Ochsner & R. D. Adams. Fiber to chip fusion splicing for robust, low loass photonic packaging. Handbook of Adhesion Technology, Springer-Verlag Berlin Heidelberg, 2011.

[Dai 19] J. Dai, S. Xi & D. Li. *Numerical Analysis of Curing Residual Stress and Deformation in Thermosetting Composite Laminates with Comparison between Different Constitutive Models.* Materials, 2019.

[Das 20] T. K. Das, B. Shirinzadeh, M. Ghafarian & A. Al-Jodah. *Design, analysis, and experimental investigation of a single-stage and low parasitic motion piezoelectric actuated microgripper.* IOP, Smart Materials and Structures, 2020.

[Das 21] T. K. Das, B. Shirirnzadeh, A. A.-Jodah, M. Ghafarian & J. Pinskier. *A novel compliant piezoelectric actuated symmetric microgripper for the parasitic motion compensation.* Elsevier, Mechanism and Machine Theory, vol. 155, no. 1, 2021.

[Dash 19] J. N. Dash, Z. Liu, D. S. Gunawardena & H.-Y. Tam. *Fabry–Perot cavity-based contact force sensor with high precision and a broad operational range.* OSA, Optics Letters, vol. 44, no. 14, page 3546, 2019.

[Deng 19] J. Deng, W. Chen & H. Yu. *A XY Transporting and Nanopositioning Piezoelectric Robot Operated by Leg Rowing Mechanism.* IEEE/ASME Transactions of Mechatronics, vol. 24, no. 1, pages 207–217, 2019.

[Deng 20] J. Deng, Y. Liu, S. Zhang & J. Li. *Development of a Nano-Positioning Platform with Large Travel Range Based on Bionic Quadruped Piezoelectric Actuator.* IEEE/ASME Transactions of Mechatronics, 2020.

[Desroches 18] J. Desroches, M. Jermyn, M. Pinto, F. Picot, M.-A. Tremblay, S. Obaid, E. Marple, K. Urmey, D. Trudel, G. Soulez, M.-C. Guiot, B. C. Wilson, K. Petrecca & F. Leblond. *A new method using Raman spectroscopy for in vivo targeted brain cancer tissue biopsy.* Nature, Scientific Reports, 2018.

[Dosta 17] M. Dosta, C. Costa & H. A. Al-Qureshi. *Numerical investigation of compaction of deformable particles with bonded-particle model.* EPJ Web of Conferences 140, 15021, Powders & Grains, 2017.

[Estrada 18] M. A. Estrada, S. Mintchev, D. L. Christensen, M. R. Cutkosky & D. Floreano. *Forceful manipulation with micro air vehicles.* Science Robotics, 2018.

[Fornes-Leal 16] A. Fornes-Leal, C. Garcia-Pardo, M. Frasson, V. P. Beltran & N. Cardona. *Dielectric characterization of healthy and malignant colon tissues in the 0.5–18 GHz frequency band.* IOP, Physics in Medicine & Biology, vol. 61, no. 20, 2016.

[Gakkestad 10] J. Gakkestad, P. Dalsjo, H. Kristiansen, R. Johannessen & M. M. V. Taklo. *Use of conductive adhesive for MEMS interconnection in ammunition fuze applications.* Journal of Micro/Nanolithography, MEMS, and MOEMS, vol. 9, 2010.

[Galeano 20] J. Galeano, A. Zarzycki, J. G. Reyes & M. E. Moncada. *Optical characterization of collagen scaffolds using multispectralimages and a light-scaffold interaction model.* Elsevier, Biomedical Signal Processing and Control, 2020.

[Gan 19] J. Gan & X. Zhang. *Nonlinear Hysteresis Modeling of Piezoelectric Actuators Using a Generalized Bouc–Wen Model.* MDPI, Micromachines, vol. 10, 2019.

[Gao 20] J. Gao, J. Zhan & Z. Yang. *Enzyme-Instructed Self-Assembly (EISA) and Hydrogelation of Peptides.* Advanced Materials, 2020.

[Greaves 11] G. N. Greaves, A. L. Greer, R. S. Lakes & T. Rouxel. *Poisson's ratio and modern materials.* Nature Materials, 2011.

[Guggenheim 17] J. W. Guggenheim, L. P. Jentoft, Y. Tenzer, & R. D. Howe. *Robust and Inexpensive 6-Axis Force-Torque Sensors using MEMS Barometers.* IEEE/ASME Transactions on Mechatronics, vol. 22, no. 2, pages 838–844, 2017.

[Gursky 19] B. Gursky, S. Bütefisch, M. L.-Schädel, K. Li, B. Matheis & A. Dietzel. *A Disposable Pneumatic Microgripper for Cell Manipulation with Image-Based Force Sensing.* MDPI, Micromachines, vol. 10, no. 10, 2019.

[He 14] X. He, J. Handa, P. Gehlbach, R. Taylor & I. Iordachita. *A Submillimetric 3-DOF Force Sensing Instrument With Integrated Fiber Bragg Grating for Retinal Microsurgery.* IEEE Transactions on Biomedical Engineering, vol. 61, no. 2, pages 522–534, 2014.

[Hossain 09] M. Hossain, G. Possart & P. Steinmann. *A small-strain model to simulate the curing of thermosets.* Computational Mechanics, vol. 43, pages 769–779, 2009.

[Jiang 19] P. Jiang, Y. Yang, M. Z. Q. Chen & Y. Chen. *A variable stiffness gripper based on differential drive particle jamming.* IOP, Bioinspiration & Biomimetics, vol. 14, no. 3, 2019.

[Komati 12] B. Komati, J. Agnus, C. Clévy & P. Lutz. *Suspended submicron silicon-beam for high sensitivity piezoresistive force sensing cantilevers.* Sensors and Actuators, 2012.

[Komati 14a] B. Komati, J. Agnus, C. Clévy & P. Lutz. *Prototyping of a highly performant and integrated piezoresistive force sensor for microscale applications, Sensors.* Journal of Micromechanics and Microengineering, 2014.

[Komati 14b] B. Komati, C. Clévy & P. Lutz. *Force tracking impedance control with unknown environment at the microscale.* Proc. - IEEE Int. Conf. Robot. Autom., page 5203–5208, 2014.

[Komati 16a] B. Komati, C. Clévy & P. Lutz. *High Bandwidth Microgripper With Integrated Force Sensors and Position Estimation for the Grasp of Multistiffness Microcomponents.* IEEE/ASME Transactions on Mechatronics, 2016.

[Komati 16b] B. Komati, A. Kudryavtsev, C. Clévy, G. Laurent, B. Tamadazte, J. Agnus & P. Lutz. *Automated robotic microassembly of flexible optical components.* IEEE International Symposium on Assembly and Manufacturing, 2016.

[L.-Evans 20] H. L.-Evans, C. A. Griffiths & A. A. Fahmy. *An experimental study into displacement of a shape memory alloy actuated robotic microgripper.* IOP, Engineering Research Express, vol. 2, no. 1, 2020.

[Lee 18] T. Y. Lee, K. Han, D. O. Barrett, S. Park, S. A. Soper & M. C. Murphy. *Accurate, predictable, repeatable micro-assembly technology for polymer, microfluidic modules.* Sensors Actuators, B Chem., vol. 254, pages 1249–1258, 2018.

[Lee 20] Y. R. Lee, J. Neubauer, K. J. Kim & Y. Cha. *Multidirectional Cylindrical Piezoelectric Force Sensor: Design and Experimental Validation.* MDPI, Sensors, vol. 20, no. 17, page 4840, 2020.

[Li 19] T. Li, N. K. K. King & H. Ren. *Disposable FBG-Based Tridirectional Force/Torque Sensor for Aspiration Instruments in Neurosurgery.* IEEE, Transactions on Industrial Electronics, vol. 67, no. 4, pages 3236–3247, 2019.

[Li 20a] T. Li, A.Pan & H. Ren. *A High-Resolution Triaxial Catheter Tip Force Sensor With Miniature Flexure and Suspended Optical Fibers.* IEEE, Transactions on Industrial Electronics, vol. 67, no. 6, pages 5101–5111, 2020.

[Li 20b] T. Li, N. K. K. King & H. Ren. *Disposable FBG-Based Tridirectional Force/Torque Sensor for Aspiration Instruments in Neurosurgery.* IEEE Transactions on Industrial Electronics, vol. 67, no. 4, pages 3236–3247, 2020.

[Li 20c] T. Li, A. Pan & H. Ren. *A High-Resolution Triaxial Catheter Tip Force Sensor With Miniature Flexure and Suspended Optical Fibers.* IEEE Transactions on Industrial Electronics, vol. 67, no. 6, pages 5101–5111, 2020.

[Liseli 17] J. B. Liseli, J. Agnus, P. Lutz & M. Rakotondrabe. *Self-Sensing method considering the dynamic impedance of piezoelectric based actuators for ultra-low frequency.* IEEE Robotics and Automation Letters, vol. 3, no. 2, pages 1049–1055, 2017.

[Liu 13] H. Liu, S. Yang, Y. Zhao, Z. Jiang, Y. Liu, & B. Tian. *A Micro-Force Sensor with Slotted-Quad-Beam Structure for Measuring the Friction in MEMS Bearings.* MDPI Sensors, vol. 13, pages 13178–13191, 2013.

[Liu 17] Y. Liu, Y. Zhang & Q. Xu. *Design and Control of a Novel Compliant Constant-Force Gripper Based on Buckled Fixed-Guided Beams.* IEEE/ASME Transactions on Mechatronics, 2017.

[Liu 19] Y. Liu, L. Wang, H. Feng, X. Ren, J. Ji, F. Bai & H. Fan. *Microemulsion-Assisted Self-Assembly and Synthesis of Size-Controlled Porphyrin Nanocrystals with Enhanced Photocatalytic Hydrogen Evolution.* ACS, Nano Letters, 2019.

[Liu 20] S. Liu, Y.-F. Li & X.-W. Wang. *A Novel Dual-Probe-Based Micrograsping System Allowing Dexterous 3-D Orientation Adjustment.* IEEE Transactions on Automation Science and Engineering, 2020.

[Lu 18] Z. Lu, P. Huang, Z. Liu & H. Chen. *Fuzzy Observer-based Hybrid Force/Position Control Design for a Multiple-sampling-rate Bimanual Teleoperation System.* IEEE Trans. Fuzzy Syst., 2018.

[Ma 19] Y. Ma, K. Du, D. Zhou, J. Zhang, X. Liu & D. Xu. *Automatic precision robot assembly system with microscopic vision and force sensor.* International Journal of Advanced Robotic Systems, 2019.

[Ma 20] Y. Ma, D. Xu & F. Qin. *Efficient Insertion Control for Precision Assembly Based on Demonstration Learning and Reinforcement Learning.* IEEE Transactions on Industrial Informatics, 2020.

[McCarthy 14] E. K. McCarthy, A. T. Bellew, J. E. Sader & J. J. Boland. *Poisson's ratio of individual metal nanowires.* Nature Communications, 2014.

[Memar 19] A. H. Memar & E. T. Esfahani. *A Robot Gripper with Variable Stiffness Actuation for Enhancing Collision Safety.* IEEE Transactions on Industrial Electronics, 2019.

[Morales 18] A. R. R. Morales & M. E. Zaghloul. *Highly Sensitive Wearable Piezoelectric Force Sensor With Quasi-Static Load Testing.* IEEE, Sensors Journal, vol. 18, no. 24, pages 9910–9918, 2018.

[Mosca 20] S. Mosca, P. Lanka, N. Stone, S. K. V. Sekar, P. Matousek, G. Valentini & A. Pifferi. *Optical characterization of porcine tissues from various organs in the 650–1100 nm range using time-domain diffuse spectroscopy.* Biomedical Optics Express, vol. 11, no. 3, 2020.

[Muntwyler 10] S. Muntwyler, F. Beyeler & B. J. Nelson. *Three-axis micro-force sensor with sub-micro-Newton measurement uncertainty and tunable force range.* Journal of Micromechanics and Microengineering, 2010.

[Müller 15] T. Müller, V. K. Venu, S. Haag, D. Zontar, S. Sauer, C. Wenzel & C. Brecher. *UV Curable Formulations for UV-C LEDs.* Strategies for precision adhesive bonding of micro-optical systems, vol. 9346, 2015.

[Na 19] C.-H. Na & K.-S. Yun. *Capacitive Force Sensor with Wide Dynamic Range Using Wrinkled Micro Structures as Dielectric Layer.* ASP, Journal of Nanoscience and Nanotechnology, vol. 19, pages 6663–6667, 2019.

[Nauriyal 18] J. Nauriyal, M. Song, R. Yu & J. Cardenas. *Fiber to Chip Fusion Splicing for Robust, Low Loass Photonic Packaging.* arXiv:1810.09531 [physics.app-ph], 2018.

[Neugebauer 11] R. Neugebauer, H.-J. Koriath, A. F. V. der Merwe, M. Müller & S. Matope. *Study on applicability of adhesive forces for micro-material handling in production technology.* ISEM Proceedings, 2011.

[Noh 16] Y. Noh, S. Sareh, H. Würdemann, H. Liu, J. Back, J. Housden, K. Rhode & K. Althoefer. *Three-Axis Fiber-Optic Body Force Sensor for Flexible Manipulators.* IEEE, Sensors Journal, vol. 16, no. 6, 2016.

[Norland 00] E. A. Norland & F. S. Martin. *Mechanisms Relating to Reducing Stress in Curing Thick Sections of UV Adhesives.* Norland Products Inc., 2000.

[norton 78] P. norton & J. Brandt. *Temperature coefficient of Resistance for p- and n-type Silicon.* Solid State Electronics, vol. 21, pages 969–974, 1978.

[Oh 18] S. Oh, J. Kim & S. T. Chang. *Highly sensitive metal-grid strain sensors via water based solution processing.* RSC Advances, 2018.

[Okamura 16] H. Okamura, S. Niizeki, T. Ochi & A. Matsumoto. *UV Curable Formulations for UV-C LEDs.* Journal of Photopolymer Science and Technology, vol. 29, pages 99–104, 2016.

[Park 16] B. Park, J. Kim, D. Kang, C. Jeong, K. S. Kim, J. U. Kim, P. J. Yoo & T. Kim. *Dramatically Enhanced Mechanosensitivity and Signal-to-Noise Ratio of Nanoscale Crack-Based Sensors.* Advanced Materials, 2016.

[Park 18] S. Park, C. Lui, W.-H. Jung, D. Maity, C. S. Ong, J. Bush, V. Maruthamuthu, N. Hibino & Y. Chen. *Mechanical Characterization of hiPSC-Derived Cardiac Tissues for Quality Control.* Advanced Biosystems, vol. 2, no. 12, 2018.

[Percástegui 19] E. G. Percástegui, J. Mosquera, T. K. Ronson, A. J. Plajer, M. Kieffer & J. R. Nitschke. *Waterproof architectures through subcomponent self-assembly.* Royal Society of Chemistry, Chemistry Science, 2019.

[Perkel 19] J. M. Perkel. *Go big or go home.* Nature, vol. 575, no. 3, 2019.

[Puangmali 12] P. Puangmali, H. Liu, L. D. Seneviratne, P. Dasgupta & K. Althoefer. *Miniature 3-Axis Distal Force Sensor for Minimally Invasive Surgical Palpation.* IEEE/ASME Transactions on Mechatronics, vol. 17, no. 4, pages 646–656, 2012.

[R.D. 84] A. R.D. & W. W.C. *Factors Influencing the Choice of Adhesive. In: Structural Adhesive Joints in Engineering.* Springer, 1984.

[Roca 12] S. F. Roca & R. *UV Adhesive viscocity adjustment apparatus and method.* United States Patent, no. US 8.256.272 B1, 2012.

[Ruggeri 18] S. Ruggeri, G. Fontana, A. Ghidoni, A. Morelli, G. Legnani, A. M. Lezzi & I. Fassi. *A Preliminary Fluid Dynamic Model of a Vacuum Micro-Gripper With Integrated Release System.* ASME, International Design Engineering Technical Conferences and Computers and Information In Engineering Conference, 2018.

[Sabarianand 20] D. V. Sabarianand, P. Karthikeyan & T. Muthuramalingam. *A review on control strategies for compensation of hysteresis and creep on piezoelectric actuators based micro systems.* Elsevier, Mechanical Systems and Signal Processing, vol. 140, 2020.

[Senarathna 19] J. Senarathna, H. Yu, C. Deng, A. L. Zou, J. B. Issa, D. H. Hadjiabadi, S. Gil, Q. Wang, B. M. Tyler, N. V. Thakor & A. P. Pathak. *A miniature multi-contrast microscope for functional imaging in freely behaving animals.* Nature Communications, vol. 10, no. 3, 2019.

[Shang 20] W. Shang, H. Ren, M. Zhu, T. Xu & X. Wu. *Dual Rotating Microsphere Using Robotic Feedforward Compenstion Control of Cooperative Flexible Micropipettes.* IEEE Transactions on Automation Science and Engineering, 2020.

[Shen 19] F. Shen, Z. Zhang, D. Xu, J. Zhang & W. Wu. *An Automatic Assembly Control Method for Peg and Hole Based on Multidimensional Micro Forces and Torques.* International Journal of Precision Engineering and Manufacturing, 2019.

[Shi 19] C. Shi, M. Li, C. Lv, J. Li & S. Wang. *A High-Sensitivity Fiber Bragg Grating-Based Distal Force Sensor for Laparoscopic Surgery.* IEEE, Sensors Journal, vol. 20, no. 5, pages 2467–2475, 2019.

[Suzuki 19] M. Suzuki, T. Takahashi & S. Aoyagi. *A Distributed 3D Force Sensor for Detecting Insect Motion by Optically Evaluating Deformation of Microscale Grid Pattern Inscribed on A Flexible Hydrogel Sheet.* IEEE, International Conference on Solid-State Sensors, Actuators and Microsystems & Eurosensors, 2019.

[Taghipour 20] A. Taghipour, A. N. Cheema, X. Gu, & F. J. Sharifi. *Temperature Independent Triaxial Force and Torque Sensor for Minimally Invasive Interventions.* IEEE/ASME Transactions on Mechatronics, vol. 25, no. 1, pages 449–459, 2020.

[Takahashi 14] H. Takahashi, N. Thanh-Vinh, U. G. Jung, K. Matsumoto & I. Shimoyama. *MEMS two-axis force plate array used to measure the ground reaction forces during the running motion of an ant.* Journal of Micromechanics and Microengineering, vol. 24, no. 6, 2014.

[Teixeira 18] V. S. Teixeira, W. Krautschneider & J. J. M. Rodriguez. *Bioimpedance Spectroscopy for Characterization of Healthy and Cancerous Tissues.* IEEE, International Conference on Electrical Engineering and Photonics, 2018.

[Tennico 10] Y. H. Tennico, M. T. Kosedjojo, S. Kondo, D. T. Mandrell & V. T. Remcho. *Surface modification-assisted bonding of polymer-based microfluidic devices.* Sensors and Actuators B: Chemical, vol. 143, no. 2, pages 799–804, 2010.

[Tisnes 20] S. D. Tisnes, L. Petit, C. Prelle & F. Lamarque. *Modeling and experimental validation of a planar micro conveyor based on a 2 x 2 array of digital electromagnetic actuators.* IEEE/ASME Transactions on Mechatronics, 2020.

[V.-Chable 19] P. V.-Chable, C. F.-Bello, J. O. S.-Reyes, M. T.-Torres & J. Varona. *A novel electrothermal compliance microgripper.* IEEE, International Conference on Mechatronics, Electronics and Automotive Engineering, Mexico, 2019.

[Vyskocil 20] J. Vyskocil, C. Mayorga-Martinez, E. Jablonska, F. Novotny, T. Ruml & M. Pumera. *Cancer Cells Microsurgery via Asymmetric Bent Surface Au/Ag/Ni Microrobotic Scalpels Through a Transversal Rotating Magnetic Field.* ACS Nano, vol. 14, no. 7, pages 8247–8256, 2020.

[Wang 17] G. Wang & Q. Xu. *Design and Precision Position/Force Control of a Piezo-Driven Microinjection System.* IEEE/ASME Trans. Mechatronics, vol. 22, no. 4, pages 1744–1754, 2017.

[Wang 18] H. Wang, J. Li, J. Cui, Q. Shi, Z. Zheng, T. Sun, Q. Huang & T. Fukuda. *Microrobotic Assembly of Shape-Customized Three-Dimensional Microtissues Based on Surface Tension Driven Self-Alignment.* IEEE Transactions on Nanotechnology, vol. 17, no. 4, pages 684–687, 2018.

[Wang 19a] F. Wang, B. Shi, Z. Huo, Y. Tian, X. Zhao & D. Zhang. *Smooth Displacement/Force Switching Control of a Piezoelectric Actuated Microgripper for Micro Manipulation.* IEEE International Conference on Manipulation, Manufacturing and Measurement on the Nanoscale, 2019.

[Wang 19b] Y. Wang, Y. Hiratsuka, T. Nitta, K. Uesugi & K. Morishima. *Micro-Assembly Using Optically Patterned Molecular-Motor-Powered Artificial Muscles.* International Conference on Micro Electro Mechanical Systems (MEMS), 2019.

[Wang 20a] L. Wang, D. Jones, G. J. Chapman, H. J. Siddle, D. A. Russell, A. Alazmani & P. Culmer. *An Inductive Force Sensor for In-Shoe Plantar Normal and Shear Load Measurement.* IEEE, Sensors Journal, vol. 20, no. 22, pages 13318–13331, 2020.

[Wang 20b] Y. Wang, H. Huang, Y. Zhao, Z. Feng, H. Fan, T. Sun & Y. Xu. *Self-assembly of ultralight and compressible inorganic sponges with hierarchical porosity by electrospinning.* Ceramics International, 2020.

[Wei 15] Y. Wei & Q. Xu. *An Overview of Micro-Force Sensing Techniques.* Elsevier, Sensors and Actuators A, 2015.

[Wei 19] G. Wei, Q. Jiang & T. Zhang. *A flexible force sensor based on spheroidal Fabry-Perot micro-cavity.* Elsevier, Optik, vol. 181, pages 483–492, 2019.

[Wu 19] Z. Wu, L. Li, Y. Yang, P. Hu, Y. Li, S. Yang, L. V. Wang & W. Gao. *A microrobotic system guided by photoacoustic computed tomography for targeted navigation in intestines in vivo.* Science Robotics, vol. 4, no. 32, 2019.

[Xie 16] Y. Xie, Y. Zhou, Y. Lin, L. Wang, & W. Xi. *Development of a Microforce Sensor and Its Array Platform for Robotic Cell Microinjection Force Measurement.* MDPI Sensors, vol. 16, 2016.

[Xie 18] H. Xie, H. Z. nad J. Song, X. Meng, Y. Wen & L. Sun. *High-Precision Automated Micromanipulation and Adhesive Microbonding with Cantilevered Micropipette Probes in Dynamic Probing Mode.* IEEE/ASME Transactions on Mechatronics, 2018, 2018.

[Xie 19] H. Xie, X. Meng, H. Zhang & L. Sun. *Development of a Magnetically Driven Microgripper for PicoNewton Force-Controlled Microscale Manipulation and Characterization.* IEEE Transactions on Industrial Electronics, vol. 67, no. 3, pages 2065–2075, 2019.

[Xing 18] D. Xing, F. Liu, S. Liu & D. Xu. *Efficient Insertion of Partially Flexible Objects in Precision Assembly.* IEEE Transactions on Automation Science and Engineering, 2018.

[Xiong 14] L. Xiong, P. Chen & Q. Zhou. *Adhesion promotion between PDMS and glass by oxygen plasma pre-treatment.* Journal of Adhesion Science and Technology, vol. 28, no. 11, page 1046–1054, 2014.

[Yanagida 17] T. Yanagida, R. E. Mohan, T. Pathmakumar, K. Elangovan & M. Iwase. *Design and Implementation of a Shape Shifting Rolling–Crawling–Wall-Climbing Robot.* MDPI, Applied Science, 2017.

[Yang 13] S. Yang & N. Lu. *Gauge Factor and Stretchability of Silicon-on-Polymer Strain Gauges, Sensors.* MDPI Sensors, 2013.

[Yang 17] S. Yang, Q. Xu & Z. Nan. *Design and Development of a Dual-Axis Force Sensing MEMS Microgripper.* Journal of Mechanism and Robotics, vol. 9, no. 6, 2017.

[Yang 18] Y.-L. Yang, J.-Q. Lou, G.-H. Wu, Y.-D. Wei, & L. Fu. *Design and position/force control of an S-shaped MFC microgripper.* Elsevier, Sensors and Actuators, vol. 282, pages 63–78, 2018.

[Yang 20] L. Yang, Y. Zhang, Q. Wang & L. Zhang. *An Automated Microrobotic Platform for Rapid Detection of C. diff Toxins.* IEEE Transactions on Biomedical Engineering, vol. 67, no. 5, pages 1517–1527, 2020.

[Yao 19] Z.-F. Yao, Y.-Q. Zheng, Q.-Y. Li, T. Lei, S. Zhang, L. Zou, H.-Y. Liu, J.-H. Dou, Y. Lu, J.-Y. Wang, X. Gu & J. Pei. *Wafer-Scale Fabrication of High-Performance n-Type Polymer Monolayer Transistors Using a Multi-Level Self-Assembly Strategy.* Advanced Materials, 2019.

[Yasa 19] I. C. Yasa, A. F. Tabak, O. Yasa, H. Ceylan & M. Sitti. *3D-Printed Microrobotic Transporters with Recapitulated Stem Cell Niche for Programmable and Active Cell Delivery.* Advanced Functional Materials, vol. 29, no. 17, 2019.

[Yeh 19] S.-K. Yeh & W. Fang. *Inductive Micro Tri-Axial Tactile Sensor Using a CMOS Chip With a Coil Array.* IEEE, Electron Device Letters, vol. 40, no. 4, pages 620–623, 2019.

[Yokouchif 20] K. Yokouchif, T. Kamegawa, T. Matsuno, T. Hiraki, T. Yamaguchi & A. Gofuku. *Development of a Gripper with Variable Stiffness for a CT-Guided Needle Insertion Robot.* Journal of Robotics and Mechatronics, 2020.

[Yong 09] Y. K. Yong, S. S. Aphale & S. O. R. Moheimani. *Design, Identification, and Control of a Flexure-Based XY Stage for Fast Nanoscale Positioning.* IEEE Transactions on Nanotechnology, vol. 8, no. 1, 2009.

[Youssefi 19] O. Youssefi & E. Diller. Dry surface micromanipulation using an untethered magnetic microrobot. Springer, Cham, 2019.

[Zhang 19] R. Zhang, A. Sherehiy, Z. Yang, D. Wei, C. K. Harnett & D. O. Popa. *ChevBot – An Untethered Microrobot Powered by Laser for Microfactory Applications.* International Conference on Robotics and Automation, 2019.

[Zyvex 20] Zyvex. *Gear Assembly on 100 μm Tungsten wire.* `https://www.zyvexlabs.com/Technology/MicroAssembly.html`, 2020.

Titre : Instrumentation multi-axes pour micro-assemblage robotisé

Mots clefs: Instrumentation, Micro-assemblage, Control

Résumé : L'instrumentation dans les micro-dispositifs a attiré l'attention de différents domaines et a été récemment démontrée avec un large éventail d'acceptabilité de la médecine à la technologie spatiale. Les industries qui souhaitent effectuer diverses tâches de micro-assemblage et robotiser ce processus nécessitent également une instrumentation dédiée. Cette thèse cible l'étude du micro-assemblage, analysant la complexité et le développement de l'instrumentation. Avec les besoins potentiels de collage pour le micro-assemblage dans les industries, le comportement de collage est analysé. La complexité vers un assemblage précis est abordée avec une approche microrobotique selon 1 axe (potentiellement affectée par le collage). L'approche démontrée avec 0.2 μm de précision de positionnement du produit collé. L'extension de l'approche pour un collage précis multi-axes nécessite une instrumentation multi-axes. Cette thèse a démontré le développement de 3 systèmes instrumentés. Cela constitue une plate-forme de détection de force / couple multi-axes, un outil de détection de force à 2 axes, tandis que le troisième est un microgripper instrumenté développé à partir de l'outil de détection de force développé. La thèse couvre différents travaux, de la conception, la modélisation, la fabrication et la validation expérimentale des différents systèmes développés.

Title : Multi-axis Instrumentation for Robotized Micro-assembly

Keywords : Instrumentation, Micro-assembly, Control

Abstract : Instrumentation in the micro-devices has brought the attention of different fields and are recently demonstrated with a wide range of acceptability from medicine to space technology. Industries aiming to do various micro-assembly tasks and robotize this process, also require dedicated instrumentation. This thesis targets the study of micro-assembly, analyzing the complexity and development of instrumentation. With potential needs of gluing for micro-assembly in the industries, the gluing behavior is analyzed. The complexity towards precise assembly is addressed with a microrobotics approach along 1 axis (potentially affected by gluing). The approach demonstrated with 0.2 μm of positioning accuracy of the glued product. The extension of the approach for a multi-axis precise gluing requires multi-axis instrumentation. This thesis demonstrated the development of 3 instrumented systems. This constitutes a multi-axis force/torque sensing platform, a 2 axis force sensing tool, while the third is an instrumented microgripper developed from the developed force sensing tool. Thesis covers different works, from design, modeling, fabrication and experimental validation of the different systems developed.

Université Bourgogne Franche-Comté
32, avenue de l'Observatoire
25000 Besançon